Local Spectroscopy of Correlated Electron Systems at Metal Surfaces

Lokale Spektroskopie an korrelierten Elektronensystemen auf Metalloberflächen

Dissertation zur Erlangung des akademischen Grades
des Doktors der Naturwissenschaften (Dr. rer. nat.)
an der Universität Konstanz
Fachbereich Physik

vorgelegt von

Peter Wahl

Dissertation der Universität Konstanz
Tag der mündlichen Prüfung: 13. Januar 2005
Referenten: Prof. Dr. Klaus Kern
Prof. Dr. Günter Schatz

Zusammenfassung

In dieser Arbeit werden elektronische Vielteilcheneffekte an Metalloberflächen mit einem Tieftemperatur-Rastertunnelmikroskop (STM) und insbesondere auch mit Rastertunnelspektroskopie (STS) untersucht. Das STM wird sowohl zur Charakterisierung der Probe eingesetzt als auch zur Präparation durch gezielte Manipulation von einzelnen Molekülen. Die Kombination von Charakterisierung und Präparation auf atomarer Skala macht das STM zu einem einzigartigen Werkzeug in der Oberflächenphysik. Der Hauptteil der vorliegenden Arbeit beschäftigt sich mit der Untersuchung des Kondoeffektes von einzelnen magnetischen Adatomen über Moleküle und Cluster bis hin zu einem Kondogitter, es werden aber auch die Eigenschaften eines zweidimensionalen Elektronengases an der Oberfläche studiert.
Dabei werden die Eigenschaften von Elektronen, die von der STM-Spitze in die Bildpotenzialzustände der Substratoberfläche injiziert werden, studiert. Die Bildpotenzialzustände bilden Quanteninterferenzmuster nahe Defekten, wie sie früher schon an den Oberflächenzustände der Edelmetall-(111)-Oberflächen beobachtet wurden. Da die Bildpotenzialzustände sich relativ weit ins Vakuum erstrecken, wird der Einfluß der Spitze des Mikroskopes diskutiert. Vielteilcheneffekte äussern sich lediglich in der effektiven Masse der Quasiteilchen sowie in deren begrenzter Lebensdauer.
Der Kondoeffekt beschreibt Phänomene an magnetischen Streuern in einer nichtmagnetischen, metallischen Umgebung. Dabei bildet sich um ein magnetisches Atom bei Temperaturen unterhalb der charakteristischen Kondotemperatur eine Wolke von Leitungsbandelektronen, die mit ihrem Spin den Spin des magnetischen Atoms abschirmen. Es bildet sich ein nichtmagnetischer Vielteilchenzustand aus. Die Auswirkungen dieses Zustandes auf makroskopische Transporteigenschaften wurde bereits vor 70 Jahren entdeckt, während sie erst vor 40 Jahren durch J. Kondo theoretisch erklärt wurden. Kürzlich hat der Kondoeffekt neues Interesse durch zwei Experimente, die das Studium des Kondoeffektes von einzelnen magnetischen Einheiten erlauben, geweckt: einerseits in Transportmessungen an Quantenpunkten, bei denen die lokale Besetzung auf eine ungerade Anzahl von Elektronen eingestellt wurde, so daß der Quantenpunkt einen Spin trägt, andererseits mit STS an einzelnen magnetischen Adatomen auf einer Edelmetalloberfläche. Die Signatur des Kondoeffektes ist eine scharfe Resonanz in der lokalen Zustandsdichte, deren Breite proportional zur Kondotemperatur ist. Aus der Kondotemperatur können Rückschlüsse auf die Kopplung zwischen dem Spin des magnetischen

Atoms und den Leitungsbandelektronen gezogen werden. In dieser Arbeit wird zunächst eine systematische Untersuchung des Kondoeffektes von einzelnen Kobaltadatomen auf den Edelmetall (111)- und (100)-Oberflächen durchgeführt. Die beobachteten Trends werden durch ein einfaches Modell erklärt. Desweiteren wird gezeigt, wie die Kopplung zwischen dem Spin des magnetischen Adatoms und dem Substrat durch die Adsorption von Liganden beeinflußt werden kann. Dabei werden auf der Oberfläche durch Adsorption von Kohlenmonoxid Kobaltkarbonylkomplexe gebildet. Die Adsorption der Liganden führt zu einer Delokalisierung der Elektronen im d-Orbital des Kobaltatoms, und dadurch zu einer Erhöhung der Kondotemperatur. Diese Erhöhung ist Ausdruck einer stärkeren Kopplung zwischen den Substratelektronen und dem d-Orbital des Kobaltadatoms.
Über die spektroskopische Charakterisierung des Kondoeffektes der Komplexe hinaus kann mit Hilfe des STMs die Kondoresonanz auch räumlich auf dem Komplex zugeordnet werden. Dadurch wird es möglich, den Spin des Kobaltatoms im Komplex mit sehr hoher Auflösung zu lokalisieren.
Mit Hilfe des Kondoeffektes kann auch die magnetische Wechselwirkung zwischen benachbarten Adatomen studiert werden. Es zeigt sich, das die magnetische Kopplung für Abstände größer als $\sim$ 6Å vernachlässigbar wird. Eine Kette von drei wechselwirkenden Atomen zeigt in Übereinstimmung mit theoretischen Vorhersagen die Ausbildung einer Lücke an der Fermienergie.
Schließlich wird ein dreidimensionales Kondosystem mit Rastertunnelmikroskopie untersucht. Als Substrat wurde $YbAl_3$ ausgewählt, das bereits mit verschiedenen Methoden studiert wurde. Wir haben unsere Proben zunächst anhand von SQUID Messungen charakterisiert um sicherzustellen, daß sie die erwarteten Eigenschaften aufweisen. Die Ergebnisse sind in hervorragender Übereinstimmung mit der Literatur. Die Untersuchung der Oberfläche mit STM zeigt die Kondoresonanz, die bereits früher mit Photoemissionsspektroskopie gesehen wurde. Die Resonanz zeigt eine Substruktur, die auf die Bildung eines Kondogitters, also eines kohärenten Zustandes der Kondowolken hindeutet.

Contents

Chapter 1

Introduction

Miniaturization is a key issue of modern technology and research, whether the silicon industry, magnetic recording or biotechnology is concerned. Nowadays, typical lateral structures on a computer chip are already smaller than 100nm [1]. As the length scales are further reduced, the limit where quantum effects start to play a role comes closer. Thus it is of fundamental interest to investigate and understand quantum effects in nanostructures. This work is concerned with the investigation of magnetic effects occuring in the limit of single spins or a few coupled spins. As for electronic effects in confined structures, new phenomena occur near single spins and in small magnetic structures due to electronic correlation effects. The study of these effects in nanostructures became only possible by the advent of scanning probe techniques [2] which enable the study of electronic structure locally. Recently by low temperature scanning tunneling microscopy (STM), the study of many body effects at surfaces became possible [3, 4] allowing to select well-defined sample areas with atomic precision. Thus, low-dimensional systems can be investigated, the spatial depence of correlation effects becomes accessible and the STM can even be used to assemble and study novel nanostructures by manipulation which would be impossible to prepare by self-assembly.
The body of this work is concerned with the Kondo effect, a typical low dimensional many body problem. The Kondo Effect of dilute magnetic alloys is already known from experiments dating back to the 1930s, when the low temperature behavior of the resistivity of noble metal samples with minute amounts of iron impurities showed a minimum at a finite temperature [5]. This resistivity minimum could only be explained about 30 years later by J. Kondo [6] by magnetic spin-flip scattering. The spins of the conduction

band electrons interact with that of the magnetic impurity and eventually undergo spin-flip scattering. The interaction strength between the spins becomes more and more important as the temperature is lowered. The interest in the Kondo effect has revived recently – another 30 year later – through two independent experimental developments. On one hand, in quantum dots it became possible to study artificial atoms consisting of electrons confined to the quantum dot and interacting with the electrons in the leads. The occupation of the quantum dot can be tuned by a gate voltage, and for odd occupation, the quantum dot carries a spin which forms a Kondo many body state with the electrons in the leads [7, 8]. On the other hand, by low temperature scanning tunneling microscopy (STM) and spectroscopy (STS) the Kondo Effect of single magnetic adatoms became accessible [3, 9]. In this way, the Kondo Effect can be explored in a very well-defined environment. It is this latter technique, that this work is concerned with.
The thesis is organized as follows: STS as a surface analysis tool being still a rather young technique, I propose and discuss ways to extract the density of states of the sample from tunneling spectra (chapt. 3). The STM is not only used to characterize the sample, but also for the preparation by manipulating single molecules. A whole chapter is devoted to the study of the dissociation process of single molecules with the STM tip (chapt. 4). As a warm-up for the many body effects, the study of a two-dimensional electron gas formed by the image states in front of a metal surface is presented (chapt. 5). Electronic correlation effects enter only through the effective mass of the states and the finite lifetime of the electrons. The investigation of many body effects occuring near impurities at metal surfaces (chapt. 6-9) starts from the Kondo effect of single magnetic adatoms (chapt. 6) and extends these results to small molecules (chapt. 7). While these systems provide insight into the coupling between the spin of the adsorbate and the conduction band of the substrate, the study of the Kondo effect in one-dimensional nanostructures (chapt. 8) offers a unique way to study magnetic interactions between impurities. Having started from 0D (impurity) problems and 1D Kondo chains, the last chapter is concerned with 3D many body effects in a Kondo alloy. The Kondo Effect of a rare-earth bulk system which has been previously investigated by photoemission, is studied (chapt. 9) to establish the connection to earlier results and pave the road towards the study of heavy fermion compounds.

Chapter 2

Scanning Tunneling Microscopy

2.1 Principle

In fig. 2.1, the basic operational principle of an STM is sketched. Between the sample and the tip a bias voltage U is applied. If the tip is sufficiently close to the sample (within ~ 20Å), a tunneling current I between tip and sample on the order of 10^{-9}A can be detected. To maintain a constant tunneling gap, the height of the tip above the sample is continuously adjusted by a feedback loop which drives a z-piezo. Since the tunneling current is a monotoneous function of the tip-sample distance, it has a well defined value for a given reference current I. By moving the tip laterally, a topographic image of the substrate surface can be acquired. For the acquisition of tunneling spectra, the feedback loop is typically deactivated and the tip-sample distance maintained constant while the bias voltage U is sweeped.

The experimental challenge in setting up an STM is twofold: 1. in order to reach the tunneling regime, the tip has to be brought very close to the surface without crashing it into the surface, 2. once the surface is reached, the mechanical stability of the instrument will determine its resolution.

2.2 Experimental

The STM which has been used for the experiments presented in this work is a home-built low-temperature UHV STM [10]. It consists of two chambers which are separated by a gate valve: A preparation chamber offering standard UHV techniques for sample cleaning, characterization and preparation

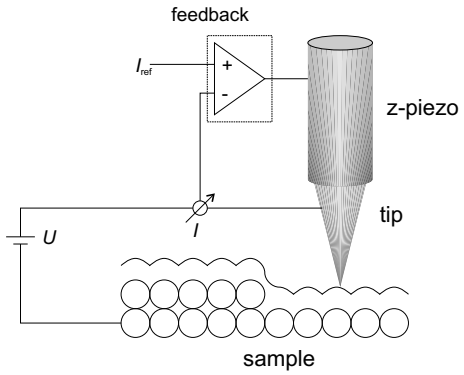

Figure 2.1: Principle of an STM: The bias voltage U is applied between tip and sample and the tunneling current I is measured. To maintain a constant I, a feed back loop controls the extension or contraction of the z-piezo. Lateral movement of the tip and acquisition of the variation of z which is neccessary to keep I constant gives a topographic image of the surface.

by metal deposition and gas dosing and a measurement chamber which contains the liquid helium cryostat with the STM. Fig. 2.2 shows a schematic drawing of the UHV chamber and cryostat.

Since STM is a technique where the tip-sample distance has to be adjusted with an accuracy in the picometer-regime, it is extremely sensitive to mechanical vibrations. Therefore, a considerable effort has been undertaken to decouple the instrument from any source of mechanical or acoustical noise. The vibration isolation consists of three stages. The whole setup is placed on a platform which is actively damped to reduce low frequency noise. Additionally the chamber and the cryostat are passively damped by floating on pressurized air. To make the system insensitive against acoustic noise, the experiment is performed in an isolated hutch. The control electronics needed to operate the STM and run the vacuum chamber are situated outside the hutch so that the cryostat is not exposed to any external noise during the measurement.

The cryostat consists of a liquid helium bath which contains a 5T superconducting split coil magnet. A second outer dewar is cooled by liquid nitrogen to provide an effective radiation shield. The STM is connected to the bottom of the helium bath. Typical sample temperatures during measurements range between $5 - 10$K.

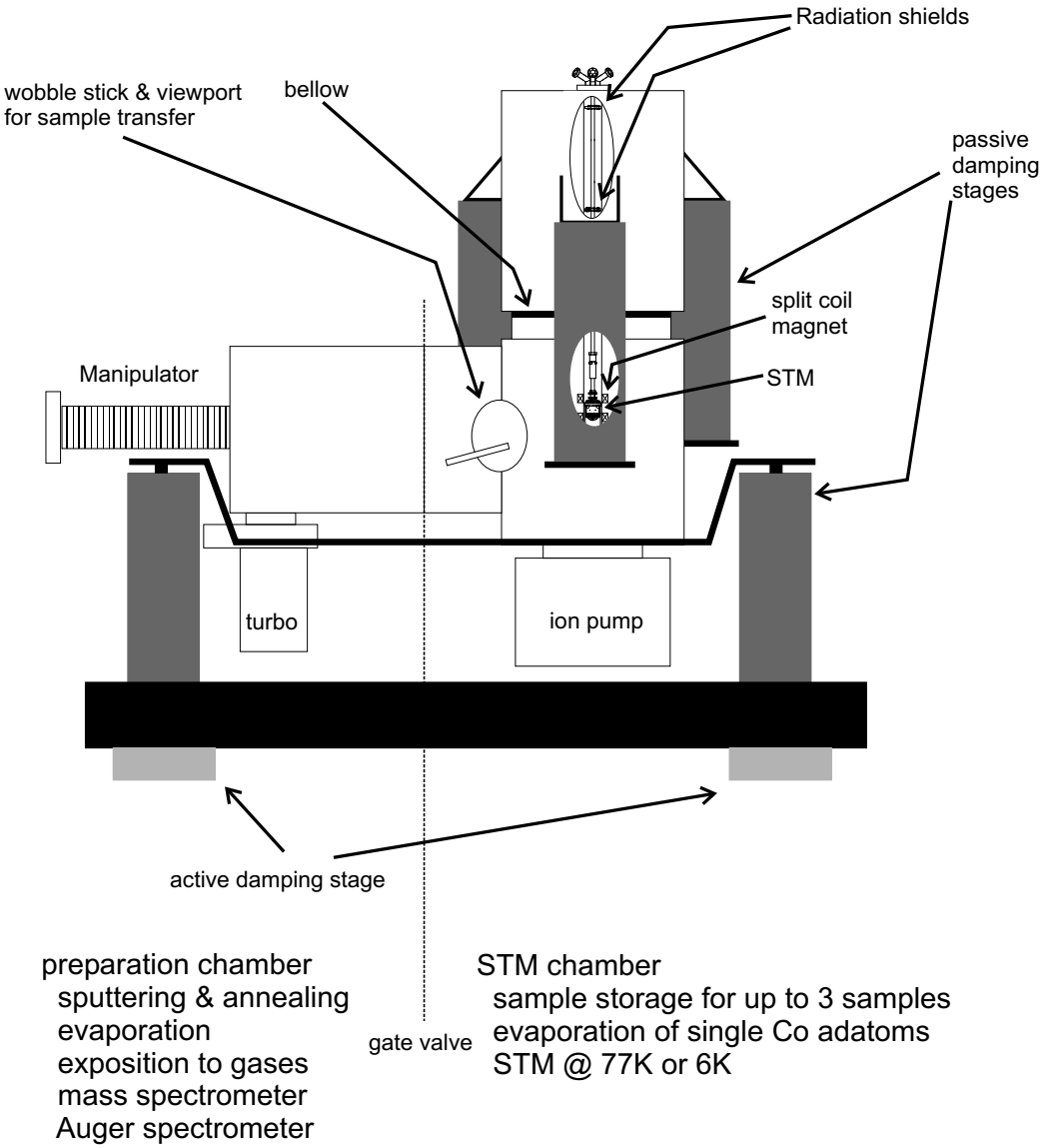

Figure 2.2: Sketch of the UHV chamber housing the low temperature STM.

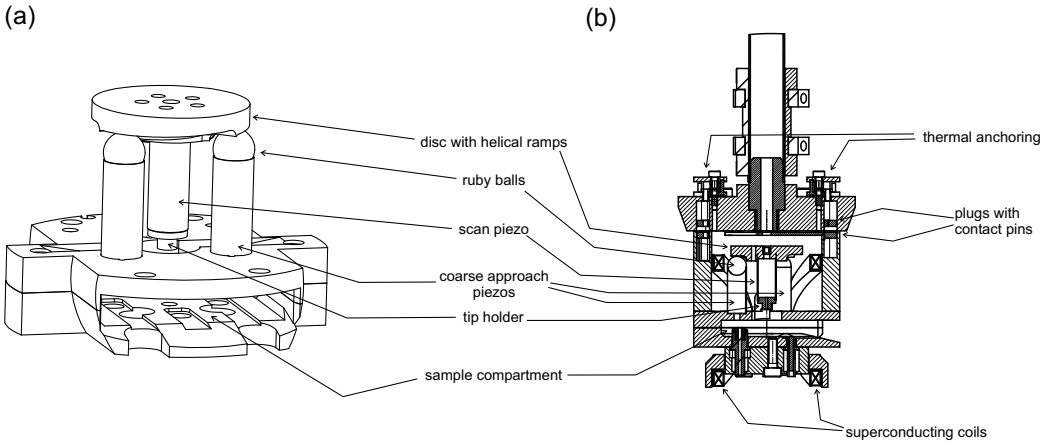

Figure 2.3: (a) Principle of a Besocke STM, (b) cut through the STM head.

The STM head is a Besocke type microscope [11]. The setup of our STM is shown in a pseudo 3D-image in fig. 2.3(a). It consists of three outer coarse approach piezos which are distributed on a circle. On top of the piezos, ruby balls are glued on which a disc with helical ramps rests. By rotation of the disc, it is raised or lowered. In the center of the disc, the scan piezo is mounted pointing downwards with the tip fixed to its end. By moving the tip down, it approaches the sample surface. The maximum vertical travelling length is limited by the range of the ramps. Originally, Besocke designed the STM with a travelling length of 300μm which puts quite severe constraints on the sample positioning inside the STM.
During this work, the original STM head [10] has been replaced by a new version offering additional functionality. A first design goal was to facilitate the exchange of the scan head during maintenance. All cables necessary to control the STM are connected to spring loaded pins. Thus the scan head can be changed easily. To allow for new experiments where the sample is exposed to a lateral electric field or a current is flowing laterally during the measurement, the sampleholders are now connected through three independent leads, which means that not only the bias connection is supplied within the STM, but also the two other contacts which are usually used for thermocouple contact. Thus, combined STM/transport measurements are in principle possible. The vertical traveling distance of the coarse approach has been extended from 300μm to 1mm. This renders the sample mounting a much simpler task than it used to be. Last but not least, the new setup com-

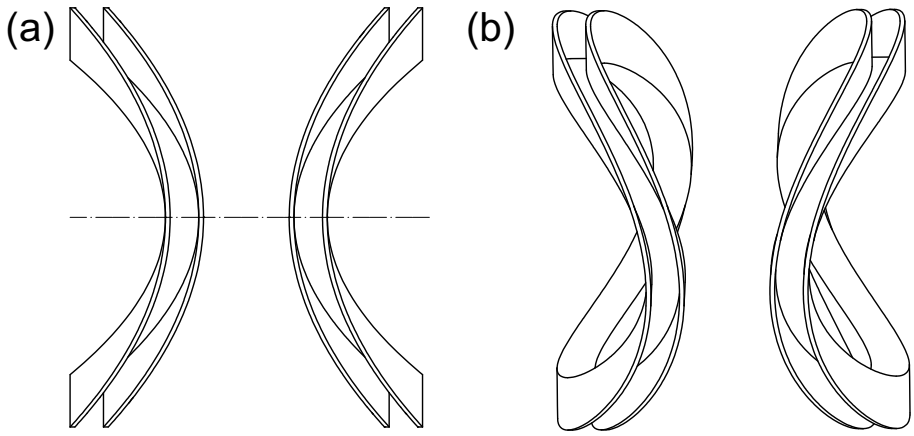

Figure 2.4: Shape of the coils implemented inside the STM.

prises an additional transverse magnetic field with up to 100mT. The coil geometry has been optimized to get the maximum field despite the limited space available. A cut through the new scan head is shown in fig. 2.3(b).
By insertion of a temperature sensor mounted on a sample holder, the sample temperature has been found to be about 6.7K.

2.3 Magnetic field

Apart from the superconducting split coil magnet which is already implemented in the cryostat, a second magnetic field with an orientation parallel to the surface has been implemented. The geometry of the two coils introduced into the STM has been optimized following two constraints: the space available inside the cryostat, limited by the outer diameter of the central bore and the geometry of the STM itself, consisting of the sample compartment and the three coarse approach piezos.
The implementation of a conventional Helmholtz split coil magnet would be the most straightforward way to include a lateral magnetic field. Due to its geometry, the magnetic field in the center of a Helmholtz split coil magnet is very homogeneous. Due to the limited space it was not possible to implement a pair of coils in the Helmholtz geometry with a reasonable number of turns of the wire in the STM body. Therefore, the geometry has been optimized to yield a maximum magnetic field at the position of the sample with an arrangement of coils which is compact enough to fit in the STM body. This

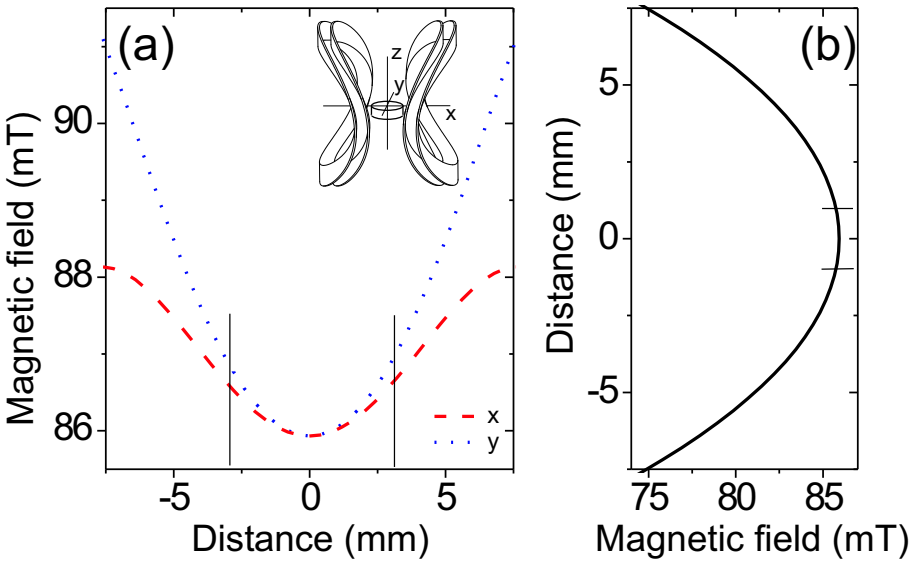

Figure 2.5: Magnetic field produced by the coil geometry shown in fig. 2.4: (a) in the sample plane, vertical lines show the limits of the sample surface, (b) perpendicular to the sample plane, horizontal lines show the maximum variation in the surface height (limited by the coarse approach).

has been achieved by modifying a Helmholtz split coil magnet: The coils have been bent outwards as if they where pressed on a tube. The geometry is shown in fig. 2.4. The magnetic field induced by the pair of coils has been calculated according to the Biot-Savart law

$$\mathrm{d}\vec{B} = \frac{\mu_0 I \mathrm{d}\vec{L} \times \vec{r}}{4\pi r^2}.$$

It relates the magnetic field B to the current I running through a piece of wire $\mathrm{d}\vec{L}$ at position $\vec{r}$ relative to the position where the field is to be calculated. This equation has been integrated numerically along the wire, assuming that the effect of the STM parts (mainly the copper body) on the magnetic field is negligible. The resulting modulus of the magnetic field in dependence of the position is shown in fig. 2.5. The deviations of the magnetic field from the main direction (along the axis of the coils) are smaller than 0.1%. The size of the sample is sketched in fig. 2.5, the homogeneity of the field is found

to be around 1%. It should be noted that area of the sample surface which is accessible by the STM tip is only about 2mm^2, so that the variation of the magnetic field within the area of interest is even smaller.

2.4 Preparation

2.4.1 Samples

The noble metal samples Cu, Ag and Au used in this work are commercially available single crystals with a polished and oriented surface. Typically, the roughness is smaller than 30nm and the miscut angle is smaller than 0.1°. *In situ* preparation of the sample surfaces consists of sputtering and annealing cycles in UHV at a base pressure $1 \cdot 10^{-10}$mbar. Sputtering has been performed with Ar ions with an ion current of $0.02\frac{\text{A}}{\text{m}^2}$. Immediatly afterwards the samples have been annealed to 800K. Samples oriented in the (100)- and (111)- direction have been used in this work.

2.4.2 Evaporants

Evaporation of single cobalt atoms has been preformed from a high-purity cobalt wire wound around a tungsten filament which is mounted close to the STM. This facilitates evaportion of single adatoms onto the sample surface at $\approx$ 20K. On the (100) surfaces, single adatoms could alternatively be prepared from commercial electron-beam heated evaporators. To avoid diffusion, the samples had to be cooled to $\approx$ 150K prior to deposition. The electron-beam heated evaporators have been equipped with high-purity ($> 99.99\%$) cobalt, copper, silver and iron.

2.4.3 Gases

For the gas adsorption experiments, a leak valve is connected to the UHV chamber, which has been used for hydrogen, oxygen and carbon monoxide. All three were supplied with a purity of at least 99.9%.

2.4.4 Tips

The experiments discussed in the following have been performed with two types of tips. Either a tungsten tip, electrochemically etched in KaOH-solution from a tungsten wire and dipped into HF to remove residual oxides has been used or an iridium tip cut from an iridium wire and mechanically ground. *In situ* preparation of the tips is restricted to field emission at 600V between tip and sample (at either polarity) with a current of $\approx 20\mu$A and gentle indentation of the tip into the single crystal surfaces. Both types of tips yielded similar topographic and spectroscopic results hence in the following the type of tip used will only be mentioned occasionally. The fact that both types of tips exhibit only minor differences in their properties is to be expected since they are prepared by indentations into the surface. This will cover the apex of the tip with the material of the substrate.

Chapter 3

Theory of Scanning Tunneling Spectroscopy

3.1 Introduction

The body of this work is concerned with the characterization of the sample surface by scanning tunneling spectroscopy (STS). In this section, I present the basic theory of STS based on the model developped by Tersoff and Hamann [12]. Since in the present context the determination of the electronic structure locally is of central interest, the main part of this chapter is devoted to the $\mathrm{d}I/\mathrm{d}V(V)$-spectroscopy, where the conductivity of the tunneling gap is measured using a lock-in detection as a function of the applied sample bias. This signal is shown to be proportional to the local density of states (LDOS) of the sample. From the theory, model spectra are calculated and discussed. A special emphasis is put on the influence of the tip on the tunneling spectra and possibilities to remove tip effects.

3.2 Tersoff-Hamann Theory

A simple and successful model to calculate the tunneling current between tip and sample is the Tersoff-Hamann picture [12]. It provides a relation between the tunneling current $I(V)$ and the LDOS of the tip $\rho_{\mathrm{t}}(\epsilon)$ and that of the sample $\rho_{\mathrm{s}}(\epsilon)$. The latter depends also on the position of the tip on the surface. Tip and sample are supposed to be in thermal equilibrium at the same temperature T. The tunneling current $I(V)$ between tip and sample at

a bias voltage V can be approximated by

$$I(V) \propto \int_{-\infty}^{\infty} \rho_{\mathrm{s}}(E)\rho_{\mathrm{t}}(E-eV)\mathcal{T}(E,V,z)\left(f(E-eV,T)-f(E,T)\right)\mathrm{d}E. \quad (3.1)$$

In this equation $\mathcal{T}(E,V,z)$ is the transmission matrix of the tunneling gap. It is commonly expressed as

$$\mathcal{T}(E,V,z) = \exp\left(-2z\sqrt{\frac{m_{\mathrm{e}}}{\hbar^2}(\Phi_{\mathrm{s}}+\Phi_{\mathrm{t}}-2E+eV)}\right). \quad (3.2)$$

The tunneling probability depends mainly on the tip-sample distance z. Furthermore it contains the work functions Φ_{s} and Φ_{t} of tip and sample, quite often it is assumed that they are the same since the tip is prepared by dipping it into the surface and thus coating it with the sample material, i.e. $\Phi = \Phi_{\mathrm{t}} = \Phi_{\mathrm{s}}$. The strong dependence of the tunneling gap on the tip-sample distance s requires the tunneling gap to be maintained very stable during the acquisition of tunneling spectra.
The two Fermi functions contained in eq. 3.1 lead to a broadening of features in the LDOS of tip and sample. The temperature of the tip limits the spectral resolution of an STM. The broadening of the Fermi function is on the order of $k_{\mathrm{B}}T$. However, the temperature broadening of the spectra can be neglected if the spectroscopic features under investigation have a width $\Gamma \gg k_{\mathrm{B}}T$. At 6K, this limit is fulfilled for $\Gamma > 1\mathrm{meV}$. Then eq. 3.1 can be simplified to give

$$I(V) \propto \int_{0}^{eV} \rho_{\mathrm{s}}(E)\rho_{\mathrm{t}}(E-eV)\mathcal{T}(E,V,z)\mathrm{d}E. \quad (3.3)$$

Most of the work presented here deals with phenomena occuring close to the Fermi level, i.e. at bias voltages V much smaller than the work funtion Φ_{t} of tip and sample. In this limit, the transmission coefficient eq. 3.2 can be approximated by

$$\mathcal{T}(z) = \exp\left(-2z\sqrt{\frac{m}{\hbar^2}(\Phi_{\mathrm{s}}+\Phi_{\mathrm{t}})}\right). \quad (3.4)$$

Thus, expression 3.3 can be rewritten to yield

$$I(V) \propto \mathcal{T}(z)\int_{0}^{eV} \rho_{\mathrm{s}}(E)\rho_{\mathrm{t}}(E-eV)\mathrm{d}E. \quad (3.5)$$

3.3 Topography

For the acquisition of topographic images, the STM can be operated in two modes: the constant current mode, where the tunneling current I is maintained constant and the variation of the tip-sample distance is recorded and the constant height mode, where the height is kept constant and the tunneling current is measured.
In constant height mode, the resulting (current) image can be simply calculated from eq. 3.1. The work presented here has been done exclusively using the constant current mode, where the image maps the tip-sample distance s. Topographic images can be calculated from eq. 3.1 by setting the current to a constant I_0 and adjusting the tip-sample distance z in the transmission coefficient $\mathcal{T}$ (eq. 3.2) accordingly. In the limit of small bias voltages V, an analytical expression for the tip-sample distance can be derived. Assuming a constant tunneling current I_0 in eq. 3.5, the tip-sample distance z is given by

$$z(V,x,y) = z_0 + \frac{1}{2\sqrt{\frac{m_e}{\hbar^2}(\Phi_s(x,y)+\Phi_t)}} \log \frac{\int_0^{eV} \rho_s(E)\rho_t(E-eV,x,y)\mathrm{d}E}{I_0}. \tag{3.6}$$

While the work function typically depends only weakly on the lateral position of the tip, the LDOS can change considerably at different spot on the surface. An STM image thus contains information on both the topographie and the electronic structure of the surface.

3.4 Spectroscopy

3.4.1 $I(V)$ and $\mathrm{d}I/\mathrm{d}V$

The tunneling current as recorded under open feedback loop conditions can be easily calculated from eq. 3.5. The same is true for the differential conductance $\mathrm{d}I/\mathrm{d}V$. The $\mathrm{d}I/\mathrm{d}V$ signal can be approxmated assuming that ρ_t and the transmission coefficient $\mathcal{T}$ are independent of V by

$$\frac{\mathrm{d}I}{\mathrm{d}V} \propto \rho_s(eV)\rho_t(0). \tag{3.7}$$

This equation states, that the $\mathrm{d}I/\mathrm{d}V$ signal is proportional to the LDOS at the position of the tip for small bias voltages at low temperature and with a

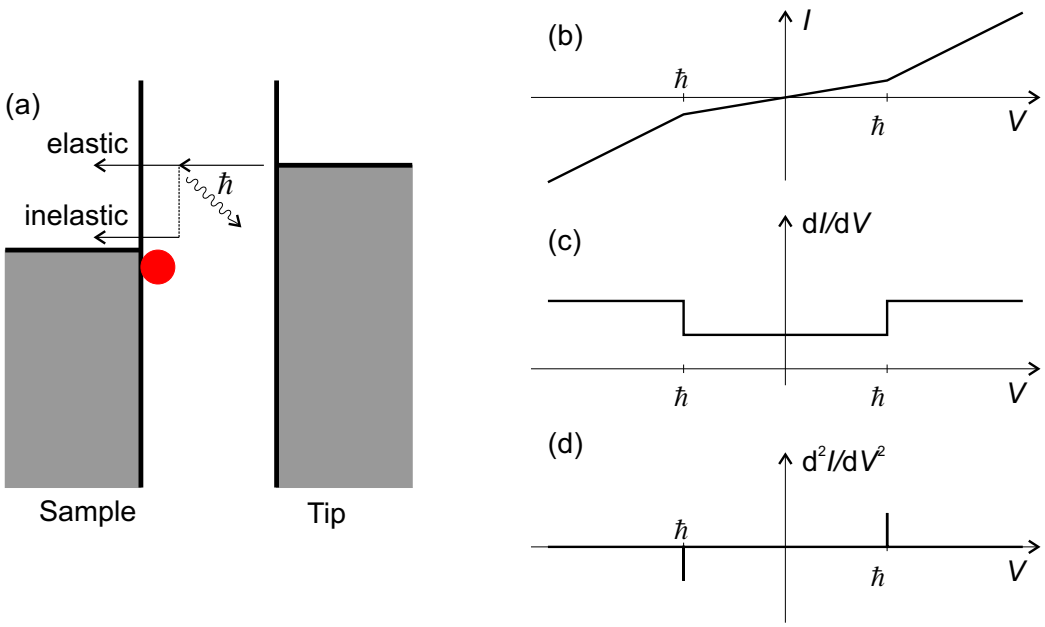

Figure 3.1: (a) Sketch of inelastic and elastic tunneling processes. (b-d) Resulting $I(V)$, $\mathrm{d}I/\mathrm{d}V$ and d^2I/d^2V-signals.

good tip. A good tip means that it has a high spatial resolution (e.g. imaging atoms spherically symmetric) and no strong features in its LDOS ρ_t.

3.4.2 IETS

If the electronic states into which a part of the tunneling current flows are coupled to other excitations e.g. vibrational [13, 14] or excitation of spin-flip processes[15], these excitations lead to an increased conductance if the tunneling electrons carry sufficient energy. Thus inelastic tunneling occurs if in addition to the direct (elastic) tunneling channel an inelastic channel opens as shown in fig. 3.1(a). It leads to steps in the $\mathrm{d}I/\mathrm{d}V$-signal at the energy of the inelastic transition. In order to increase the sensitivity, typically the $\mathrm{d}^2I/\mathrm{d}V^2$-signal is recorded using a lock-in amplifier. In the second derivative, the conductance steps are seen as peaks. In fig. 3.1(b-d) this situation is sketched for an inelastic transition at the energy $\hbar\Omega$ and its influence on the signals. Features in the LDOS can be distinguished from inelastic scattering due to vibrational transitions by their symmetry: since vibrational excitation

is independent of charge, the conductance steps are found to be symmetric with respect to the Fermi level in the $\mathrm{d}I/\mathrm{d}V$ signal and antisymmetric in the $\mathrm{d}^2I/\mathrm{d}V^2$ spectrum.

3.4.3 $z(V)$-Spectroscopy

While $\mathrm{d}I/\mathrm{d}V$ spectroscopy is the method of choice for energies close to the Fermi level, at higher bias voltages the dynamic range needed to acquire $\mathrm{d}I/\mathrm{d}V$-spectra grows due to the exponential dependence of the transmission through the tunneling gap (eq. 3.2) on the bias voltage. This can be circumvented by either keeping the feedback loop closed while acquiring the spectrum, thus the tunneling gap is increased while recording the spectrum to keep the tunneling current constant or by recording directly the tip-sample distance z while ramping the bias voltage (with closed feedback loop). $z(V)$ increases with every new state which becomes available to the tunneling electrons. This method is particularly useful for states at the sample surface which are on a similar energy scale as the work function. For bias voltages comparable to the work function, the conductivity rises strongly with rising bias voltage, so that a high dynamic range is necessary to record a spectrum. This is the case for the image potential states, which are discussed in detail in chapter 5.
For small bias voltage $V \ll \Phi$, the $z(V)$-signal can be calculated from the same expression as used for the topography (eq. 3.6). It shows, that the $z(V)$-spectrum is related to the LDOS by an integration and taking the logarithm. For larger bias voltages comparable to the work functions of tip and sample, the variation in the transmission coefficient can no longer be neglected.

3.4.4 Discussion

Fig. 3.2 shows a comparison of simulated STS spectra recorded in the various ways discussed above (except IETS). The initial LDOS consists of four lorentzian peaks as plotted in fig. 3.2(a). The features in the LDOS can be found as steps in the tunneling current (fig. 3.2(b)), but they are relatively weak due to the exponential rise of the tunneling current with increasing bias voltage. The $\mathrm{d}I/\mathrm{d}V$-signal (fig. 3.2(c)) reproduces the LDOS for small bias voltages around the Fermi level rather well, peaks at high negative or high positive bias voltages are suppressed or enhanced respectively. This enhance-

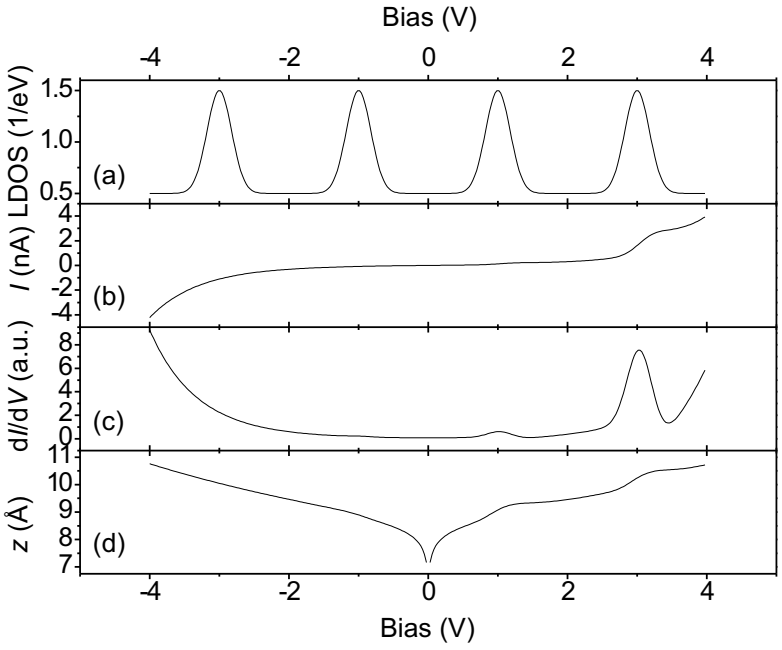

Figure 3.2: Comparison of the various spectroscopies with STM assuming a constant tip LDOS. (a) initial LDOS, (b) $I(V)$ calculated from eq. 3.1 (work function for tip and sample 5eV, tip height 10Å), (c) $\mathrm{d}I/\mathrm{d}V$-signal for a lock-in modulation of 0.1V (with open feedback loop) obtained from (b) by application of eq. 3.8, (d) $z(V)$ with closed feedback loop (numerical solution of eq. 3.3 with $I = 1\mathrm{nA}$).

ment at high bias voltages can be avoided by measuring $z(V)$ (fig. 3.2(d)), where the transmission through the tunneling barrier is adjusted by increasing the tip-sample distance. The height of the steps in $z(V)$ appears similar for comparable peak heights in the LDOS. All STS spectroscopies have in common that the sensitivity is reduced for negative bias voltages and enhanced for positive ones due to the transmission of the tunneling barrier (eq. 3.2). STS is most sensitive for unoccupied states [16].

3.5 Evaluation of tunneling spectra

In this section, the possibilities to quantitatively evaluate STS spectra are discussed. Especially the extraction of the sample LDOS - which is usually the goal of doing spectroscopy - and the influence of the tip is treated but also more technical details such as the broadening due to the detection with a lock-in amplifier.

3.5.1 Lock-in derivative

In order to enhance the dynamic range when recording the spectroscopic signal, typically the $\mathrm{d}I/\mathrm{d}V$-signal is recorded. This is achieved experimentally by employing a lock-in technique. The bias voltage is modulated with an AC signal with an amplitude between $1 - 100\mathrm{mV}$. The exact choice of the amplitude depends on the width of the spectral features to be resolved since the lock-in technique introduces additional broadening which is on the order of the amplitude of the AC signal. Analytically, the lock-in signal can be calculated from the tunneling current I by the lock-in derivative [17]

$$\frac{\mathrm{d}I}{\mathrm{d}V}(V) = \frac{2}{\pi \Delta V_{\mathrm{PP}}} \int_0^{2\pi} \sin t \cdot I\left(V + \frac{\Delta V_{\mathrm{PP}}}{2} \sin t\right) \mathrm{d}t. \tag{3.8}$$

The second derivative regularly encoutered in IETS is given by a similar expression:

$$\frac{\mathrm{d}^2 I}{\mathrm{d}V^2}(V) = -\frac{16}{\pi \Delta V_{\mathrm{PP}}^2} \int_0^{2\pi} \cos(2t) \cdot I\left(V + \frac{\Delta V_{\mathrm{PP}}}{2} \cos t\right) \mathrm{d}t \tag{3.9}$$

Apart from the sign, the main difference between eqs. 3.8 and 3.9 is in the phase of the reference signal from the lock-in amplifier.

3.5.2 Background subtraction

A variety of new and challenging experiments could be performed mainly due to the unique spatial and spectroscopic resolution of STS, which allows it to map spectroscopic features with atomic resolution. The main disadvantage of STS however is that the chemistry and shape of the apex of the tip - the "detector" of the STM - can hardly be controlled. Although a lot of recipes have been proposed for the preparation of the tip (see e.g. [18] and

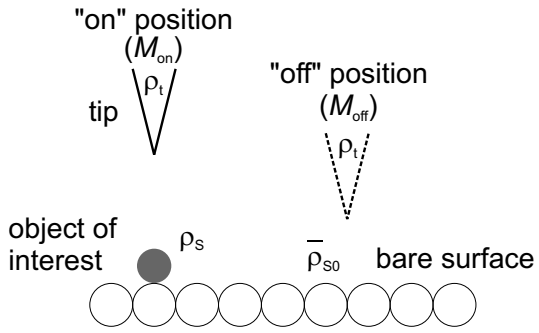

Figure 3.3: Sketch of the measurement setup and assignment of the symbols

references therein), its very end will still vary considerably from tip to tip and it even changes during a measurement. It is therefore of fundamental interest to develop standard methods for the treatment of STS spectra as they exist already for a long time for photoemission spectra [19, 20]. In the past, the possibilities to extract the LDOS of a uniform sample from tunneling spectra has been discussed [21, 16, 22]. Background subtraction for STS spectra which "calibrates" the tip on a spot of the surface with a known LDOS has only been proposed and used in the context of a specific experiment [23, 24].

The basic idea of the background subtraction schemes presented here is to characterize the LDOS of the tip $\rho_{\mathrm{t}}(E)$ on a clean spot of the surface thus allowing to recover the LDOS $\rho_{\mathrm{s}}(E)$ at the point of interest on the sample from a spectrum acquired with the same tip. It is assumed that the LDOS of the clean surface $\rho_{\mathrm{s0}}(E) = \overline{\rho}_{\mathrm{s0}}$ is known and constant. This arrangement is sketched in fig. 3.3. In principle, the same ideas can be applied if the LDOS of the surface were not constant however then the formalism becomes more complicated.

The $\mathrm{d}I/\mathrm{d}V$-signal - neglecting lock-in broadening - follows by calculating the derivative of eq. 3.5.

$$\frac{\mathrm{d}I}{\mathrm{d}V} \propto \left(- \int_0^{eV} \rho_{\mathrm{s}}(E) \frac{\mathrm{d}\rho_{\mathrm{t}}}{\mathrm{d}E}(E - eV)\mathrm{d}E + \rho_{\mathrm{s}}(eV)\rho_{\mathrm{t}}(0) \right) \tag{3.10}$$

We will denote the spectrum acquired on the object under investigation M_{on} and the spectrum on the clean surface M_{off}. Since the LDOS of the clean

sample $\overline{\rho}_{s0}$ is assumed to be constant, the "off"-spectrum is

$$M_{\text{off}}(V) = C_{\text{off}}\overline{\rho}_{s0}\rho_t(-eV), \tag{3.11}$$

were the transmission coefficient and constants are absorbed in C_{off}. The "off"-spectrum gives direct access to the LDOS of the tip ρ_t. Placing the same tip on top of the object of interest gives

$$M_{\text{on}}(V) = C_{\text{on}}\left(\rho_s(eV)\rho_t(0) - \int_0^{eV}\rho_s(E)\rho_t'(E-eV)\mathrm{d}E\right). \tag{3.12}$$

Simple background subtraction

Using a Taylor expansion for $\rho_s(E)$ around $E = 0$,

$$\rho_s(E) = \rho_s(0) + \rho_s'(0)E + \mathcal{O}(2), \tag{3.13}$$

allows us to replace $\rho_s(E)$ in the integral in eq. 3.12. In the zeroth order approximation, the integral can be solved analytically. It is valid under the assumption that ρ_s is sufficiently flat, or - more rigorously - that $E \cdot \rho_s(0)' \ll \rho_s(0)$. In that case, we can perform a background removal by simple subtraction:

$$\rho_s \propto M_{\text{on}}(V) - \frac{M_{\text{on}}(0)}{M_{\text{off}}(0)}M_{\text{off}}(V) + C \tag{3.14}$$

The prefactor $\frac{M_{\text{on}}(0)}{M_{\text{off}}}$ of the "off"-spectrum will generally be close to 1 if "on"- and "off"-spectra are recorded under similar stabilization conditions. This method determines ρ_s up to a factor and an additive constant and as we will later see, it is surprisingly successful and in most cases sufficient.

Deconvolution

A more sophisticated way to perform background subtraction is to deconvolute the "on"-spectrum with the "off"-spectrum. This is achieved by partial integration of eq. 3.12 and numerically solving the resulting integral equation for ρ_s. We can replace the tip LDOS in eq. 3.12 by application of eq. 3.11 giving

$$M_{\text{on}}(V) - \frac{M_{\text{on}}(0)}{M_{\text{off}}(0)}M_{\text{off}}(V) = \frac{C_{\text{on}}}{C_{\text{off}}\overline{\rho}_{s0}}\int_0^{eV} M_{\text{off}}(eV-E)\frac{\mathrm{d}}{\mathrm{d}E}\rho_s(E)\mathrm{d}E. \tag{3.15}$$

Apart from the boundary values $\rho_s(0)$ and $\rho_s'(0)$, this equation only depends on the measured spectra M_{on} and M_{off}. It can be solved in a discrete form, giving an algorithm for numerical background removal

$$\frac{\mathrm{d}}{\mathrm{d}E}\tilde{\rho}_s(n\Delta V) = \frac{M_{on}(n\Delta V) - \tilde{M}_{off}(n\Delta V) - \sum_{k=0}^{n-1}\tilde{M}_{off}((n-k)\Delta V)\frac{\mathrm{d}}{\mathrm{d}E}\tilde{\rho}_s(k\Delta V)e\Delta V}{M_{on}(0)\Delta V},$$

where $\tilde{M}_{off}(E) = \frac{M_{on}(0)}{M_{off}(0)}M_{off}(E)$ and $\tilde{\rho}_s(V) = \frac{\rho_s(V)}{\rho_s(0)}$. The LDOS is determined up to an additive and a multiplicative constant and the initial value $\frac{\mathrm{d}}{\mathrm{d}E}\tilde{\rho}_s(0)$. The latter will generally be close to zero for metal surfaces as discussed above. The final step in the algorithm consists of a numerical integration to obtain $\tilde{\rho}_s$.

Comparison

First, I will consider simulated STS spectra and show how the two methods perform to recover the initial sample LDOS. In the second part, experimental data will be used to show how background removal improves the quality and reproducibility of STS spectra.

The STS spectra have been calculated using a tip LDOS consisting of two Lorentzians and a sample LDOS which is composed of four Lorentzian peaks. The Tersoff-Hamann model has been employed (eqs. 3.1 and 3.2) assuming $T = 0$K but taking into account lock-in broadening with a modulation of $10\mathrm{mV_{PP}}$. The widths and positions of the peaks differ between tip and sample LDOS, both are plotted in fig. 3.4(a). The "on"-spectrum (fig. 3.4(b)) shows a complicated structure with dominant features due to the tip LDOS. These artifacts consist of dips and peaks, dominantly at the positions of the features in the tip LDOS but also at other energies. The results of both the simple background subtraction and the full deconvolution are depicted in fig. 3.4(c). While the simple background subtraction performs well on the main features it fails to remove the satellites of the tip spectrum. The situation becomes considerably better for a full deconvolution, which also suppresses the satellite features.

However for a more realistic tip LDOS, the simple background subtraction performs almost equally well as the deconvolution algorithm. This can be

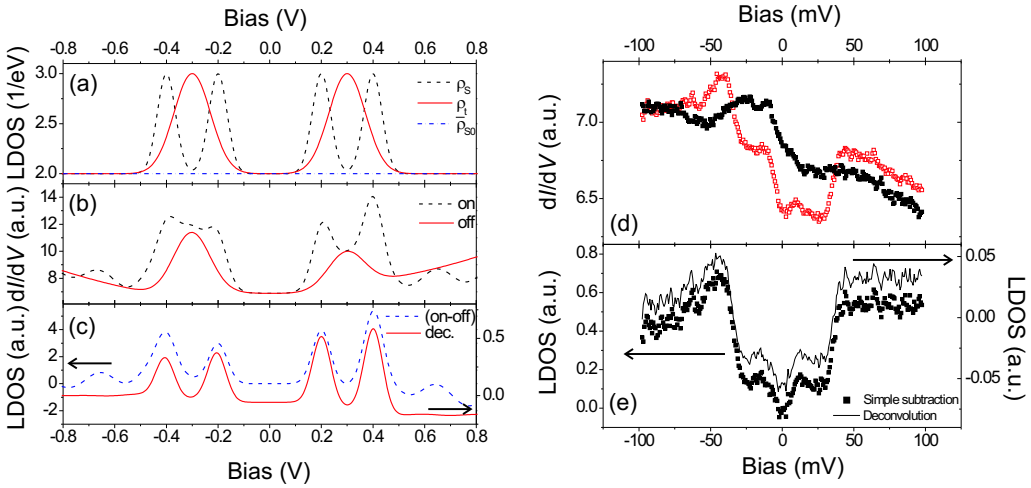

Figure 3.4: Background subtraction and tip deconvolution for STS spectra. (a) initial LDOS of the tip, of the sample at the position of the object of interest and of the clean surface. (b) calculated $\mathrm{d}I/\mathrm{d}V$-signal for a lock-in modulation of 10mV (with open feedback loop) for "on" and "off" spectrum, (c) spectrum after simple background subtraction and full deconvolution. (d) shows spectra from an experiment, the "on"-spectrum (open symbols) has been taken on a CO molecule on Cu(100), the "off"-spectrum (full symbols) on the clean surface, while (e) shows them again after background removal.

seen from the following experimental examples.
The first example deals with the IETS (inelastic electron tunneling spectrosopy) features of a CO molecule [23]. The second example shows for comparison spectra taken on the same cobalt adatom with two different tips, to demonstrate the reproducibility of the resulting background subtracted spectrum.
The "on"-spectrum shown in fig. 3.4(d) has been acquired on a CO molecule, while the "off"-spectrum has been recorded on the clean surface a few nanometers away from the CO molecule and other contaminations. It is expected to show steps in the conductance due to inelastic tunneling processes [23] as shown in fig. 3.2. The steps are expected to be symmetric with respect to the Fermi energy. The "on"- and the "off"-spectra are both rich of features. In the raw "on"-spectrum, the vibrational features can be recognized readily, but they are obscured by the tip-related structures. In the background subtracted spectra shown in fig. 3.4(e) only the vibrational features are found,

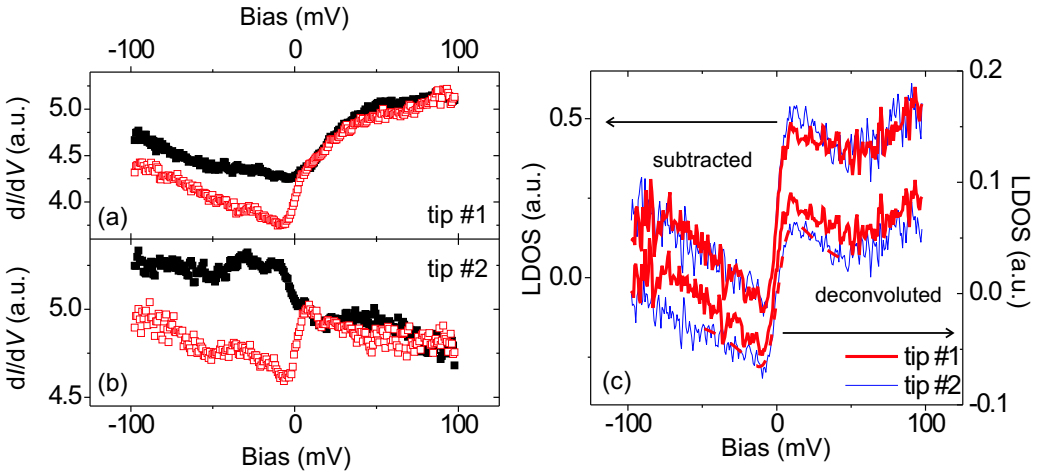

Figure 3.5: Background subtraction for the Kondo resonance of a single cobalt adatom on Cu(100): (a) and (b) are spectra recorded on (open symbols) and off (full symbols) with two different tips, (c) background subtracted spectra using both methods described here for both tips, for one of the deconvoluted spectra the fit of a Fano function is plotted (dashed line).

while the tip-related structures have been eliminated. The energies of the vibrational modes are consistent with previous work [25] and the spectrum shows the expected symmetry. The numerical deconvolution does not improve the spectrum compared to the simple subtraction method, which is to be expected since the condition for the simple subtraction to perform well, i.e. $E\frac{\rho_s'(0)}{\rho_s(0)} \ll 1$ is fulfilled.

Fig. 3.5 depicts a second example. The object under investigation is a single cobalt adatom on the Cu(100) surface. The cobalt adatoms are magnetic impurities and at low temperature the Kondo effect leads to the formation of a resonance in the LDOS at the Fermi level (see chapt. 6). Fig. 3.5(a) and (b) show a set of "on"- and "off"-spectra recorded with two different tips on the same cobalt adatom. Different means that the very end of the tip has been modified by dipping the tip into the surface. Although the "on"-spectra show comparable features at the Fermi energy, their overall behaviour is strongly influenced by features due to the LDOS of the tip. After background removal, the artifacts due to the tip have disppeared as can be seen from fig. 3.5(c). While again the full deconvolution does not improve the spectrum compared to the subtraction, this example shows the power

of background removal: after treatment of the data as decribed, the spectra are almost identical for the two different tips thus eliminating any tip-related features. For comparison, in fig. 3.5(c) the fit of a Fano function is plotted for one of the deconvoluted spectra. The observed line shape of the Kondo resonance is in excellent agreement with the fit – in constrast to the raw spectra.
It should be noted that both methods fail, if the LDOS of the substrate is strongly modified by the adsorbate within the energy range of the spectra recorded. For example, this could be the case for the surface state onset of the noble metal (111)-surfaces which can be shifted by adsorbates [26].
In conclusion, I have presented two background removal algorithms for STS spectra. The simple background subtraction offers in most cases a considerable improvement by removing the most prominent tip-related features from the spectrum. The full deconvolution algorithm is able to remove also satellite features due to the tip which cannot be handled by the simple background subtraction. The reason for the success of the simple method can be found in the condition for the validity of the approximation eq. 3.13. The variation of the LDOS of a metal is typically rather small compared to the total LDOS for energies close to the Fermi energy - which is basically the condition. So in most cases a simple subtraction of the background spectrum will be sufficient to recover the sample LDOS from the tunneling spectra. This has been demonstrated on real data for the inelastic tunneling spectrum recorded on a CO molecule on Cu(100) and for the Kondo spectra on a cobalt adatom.

Chapter 4

Single Molecule Chemistry

The development of low-temperature STMs has enabled in the past years the study of chemical reactions at a single molecule level. Especially the possibility to characterize chemical bonds and to trigger chemical reactions by the application of voltage pulses [14] has made STM a powerful tool for chemical analysis. This chapter concentrates on the topographic characterization and chemical analysis of organometallic cobalt complexes. Their spectroscopic properties will be discussed in the context of their magnetic properties in chapter 7.

4.1 Organometallic complexes at surfaces

Organometallic complexes exhibit a very rich chemistry in free space. Their common link is the existence of one or more metal-carbon bonds. If the metal center is a transition metal ion, up to six ligands can connect to it. These ligands can be either terminal or bridging. The latter enable the formation of huge organometallic clusters which can easily contain up to 20 transition metal ions [27]. Here I will only consider the simplest class of organometallic complexes, where the ligands are CO molecules and the transition metal ion is cobalt, iron or copper. Complexes with only one metal center are named mononuclear as opposed to binuclear complexes with two metal centers.
Previously, carbonyl complexes have been prepared and investigated by Lee and Ho [28], however they assembled their carbonyls by manipulation of single CO molecules with the STM tip. Our approach of growing the molecules is by using conventional UHV techniques as described in the next section.

The molecules are formed by self-assembly resulting in the surface being covered by the molecules. In addition, we find more than one species and also multinuclear species, which would be difficult to prepare with the STM tip. The study of Lee and Ho was restricted to mono- and dicarbonyl molecules.

4.1.1 Preparation

The Cu(100) single crystal surface has been cleaned as described above. After cleaning, cobalt has been evaporated from an electron-beam heated cobalt rod onto the sample at a substrate temperature of $\sim$ 150K, where diffusion and hence island formation is inhibited. The onset of diffusion of cobalt on Cu(100) is around 200K. After evaporation of minute amounts of cobalt ($\sim$ 0.001ML) leaving single cobalt adatom on the sample, the surface was exposed to 0.1 to 0.5L carbon monoxide and subsequently annealed to $200-300$K. This final annealing leads to a desorption of excess CO from the clean areas of the substrate [29]. Subsequently, the sample was transferred *in situ* into the STM. The preparation of copper and iron carbonyls follows the same recipe.

4.1.2 Topography

After preparation, the surface is covered predominantly with cobalt tetracarbonyl molecules. In addition we find more complicated binuclear species. The occurence of different species can be controlled by two parameters: 1. the cobalt coverage, which leads to the formation of more multinuclear species with increasing coverage, 2. the post-annealing temperature where a lower temperature leads to more different mononuclear species at the surface. It is interesting to note that the attachment of the CO ligands inhibits nucleation and island formation. If the sample had not been exposed to CO prior to the final annealing step, the cobalt atoms would have formed islands for annealing temperatures above 200K. The ligands either inhibit diffusion or are responsible for a repulsive interaction between the molecules.

In fig. 4.1(A-D), the mononuclear species which we find on the surface are shown together with ball models. The dominant species on the surface are $Co(CO)_4$-molecules, in addition some $Co(CO)_3$-molecules can be found on the surface. DFT calculations show that the cobalt atom sits in a hollow site with the four CO molecules pointing towards the nearest neighbour Cu atoms of the underlying substrate.

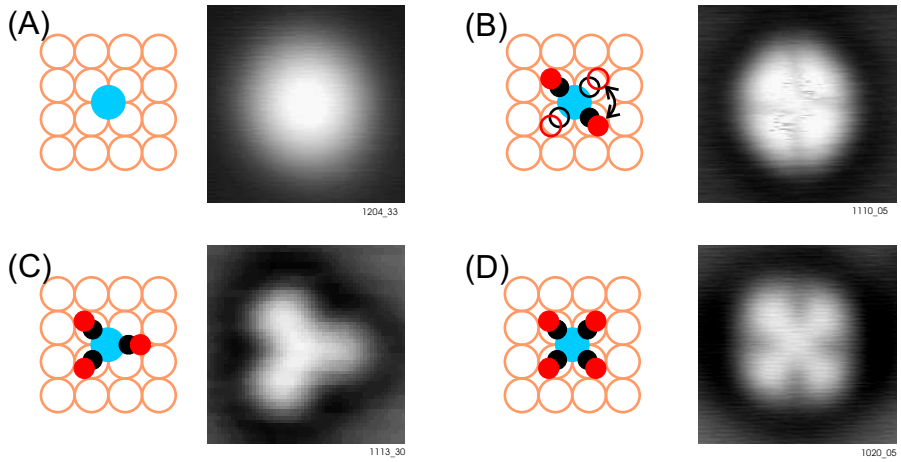

Figure 4.1: Mononuclear cobalt carbonyl complexes: (A) pure cobalt atom, (B) $Co(CO)_2$, (C) $Co(CO)_3$, (D) $Co(CO)_4$. All images and models drawn to the same scale, image size is $(1.5nm)^2$.

The cobalt dicarbonyl molecules are a product of a partial tip-induced dissociation of a cobalt tetracarbonyl complex. For comparison, also the image of a single cobalt adatom is shown. It should be noted, that the attachment of the CO ligands leads to a strong suppression of the LDOS at the Fermi energy: a cobalt tetracarbonyl molecule is imaged by the STM with an apparent height of around 20pm, while a cobalt adatom is found to be around 100pm high. Fig. 4.2 shows the main multinuclear species which are found on the surface. (B-G) show binuclear, (H) even a complex consisting of three cobalt atoms. The list could be extended to species with four atoms, but as the number of metal centers increases they become more and more rare.

4.2 Chemical analysis

The chemical identity of the molecules can be studied by tip-induced dissociation. At comparatively high positive or negative bias voltages, the injection of electrons into the molecule leads to its dissociation. Typical bias voltages, where the dissociation occurs are around $2 - 4V$.
Fig. 4.3(a) shows the surface after dissociation. At the position of the bright spherical object in fig. 4.3(a) used to be one of the clover-leaf shaped ob-

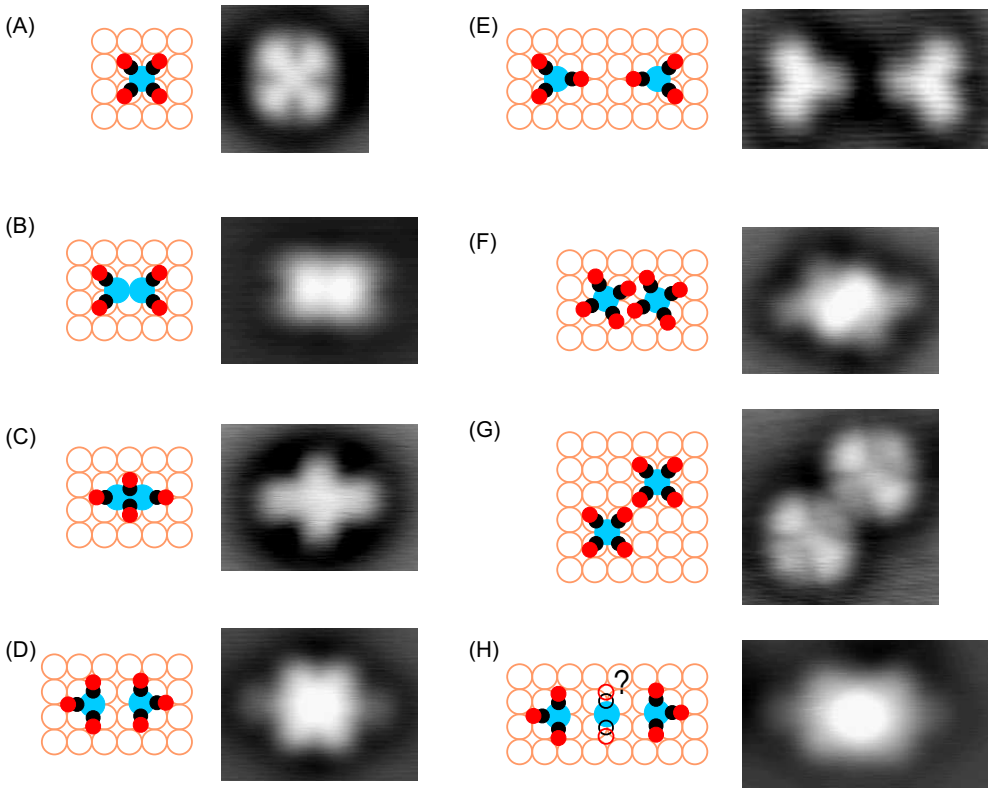

Figure 4.2: Binuclear cobalt carbonyl complexes: (A) shows for comparison the tetracarbonyl molecule ($Co(CO)_4$), (B) and (C) are molecules consisting of 2 cobalt atoms and four CO molecules, in (B) the complex consists of two dicarbonyl molecules ($(Co(CO)_2)_2$), in (C) a compact dimer with four CO molecules is formed ($Co_2(CO)_4$). (D) and (E) contain again two cobalt atoms with six CO molecules attached to it ($(Co(CO)_3)_2$), in (D) the CO molecules are rearranged while in (E) the molecules look like two tricarbonyl molecules. (F) and (G) are complexes with two tetracarbonyl molecules close together ($(Co(CO)_4)_2$), in (F) the CO molecules are again rearranged and can be in two equivalent configurations with mirror symmetry along a horizontal line (only one shown), while in (G) the shape of the tetracarbonyl molecules becomes apparent again. (H) shows a trinuclear carbonyl molecule, probably $Co(CO)_3Co(CO)_2Co(CO)_3$. All images and models drawn to the same scale.

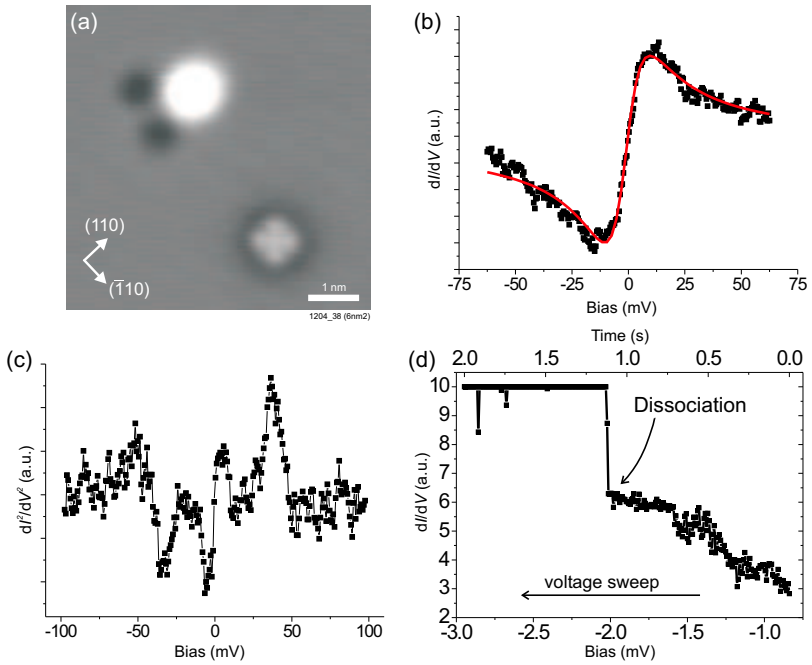

Figure 4.3: (a) Image of the destroyed carbonyl showing a cobalt adatom, two CO molecules (imaged as depressions) and another carbonyl. (b) Spectrum taken on the cobalt adatom and (c) IET spectrum taken on one of the CO molecules. (d) Spectrum with the dissociation of the carbonyl taking place at 2.02V or equivalently 1.12s.

jects, while in the lower half of the image another still intact molecule can be seen. Apparently, two types of objects remain at the position of the destroyed tetracarbonyl. Both can be identified by performing scanning tunneling spectroscopy. The $\mathrm{d}I/\mathrm{d}V$-spectrum as depicted in fig. 4.3(b) recorded on top of the bright protrusion shows the typical Kondo feature of a cobalt adatom at the Fermi level [30]. The two depressions next to the cobalt adatom in fig. 4.3(a) can be identified by inelastic electron tunneling spectroscopy (IETS). The $\mathrm{d}^2I/\mathrm{d}V^2$-signal is shown in fig. 4.3(c). It reveals the frustrated translation mode at $\pm$4mV and the frustrated rotation mode at $\pm$35mV and allows to identify the objects as CO molecules [23]. Apparently, a part of the CO molecules originally attached to the cobalt atom desorbs

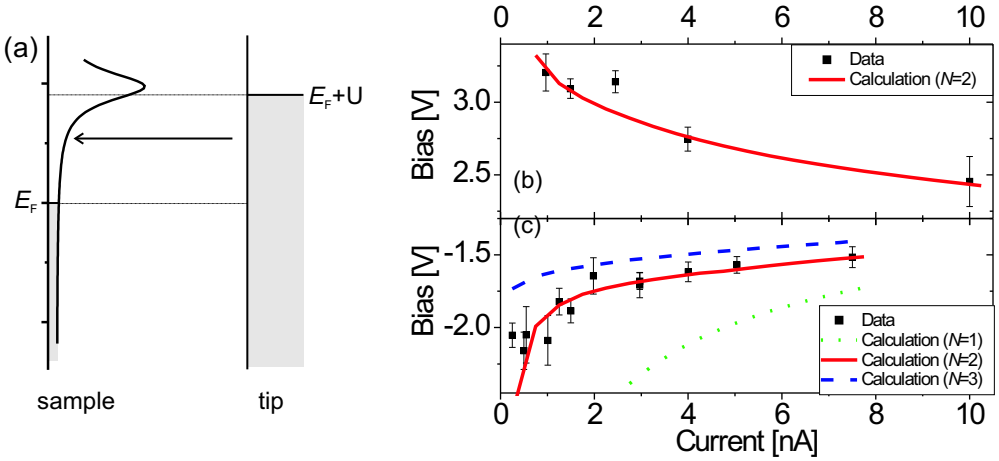

Figure 4.4: (a) Model for the dissociation induced by electron transfer. (b) and (c) Experimental curve and calculation of the dissociation voltage in dependence on the initial tunneling current for positive and negative bias voltage respectively.

upon dissociation or is attached to the tip.
Since the apparent height of the cobalt adatom is about five times larger than that of a tetracarbonyl molecule, the dissociation leads to a sudden increase in the tunneling current and in the $\mathrm{d}I/\mathrm{d}V$-signal. This increase can be exploited to detect the dissociation. A tunneling spectrum recorded on a cobalt tetracarbonyl molecule where a dissociation occured is shown in fig. 4.3(d). The spectrum is a usual $\mathrm{d}I/\mathrm{d}V$-spectrum, but as soon as the molecule underneath the tip dissociates, the increased electron density leads to a jump in the spectrum. Typically, the lock-in output is saturated after dissociation. In order to quantitatively analyze the dissociation of the molecule induced by tunneling electrons, we have recorded several spectra of the type shown in fig. 4.3(d) to measure the dependence of the voltage at which the dissociation occurs on the initial tunneling conditions. For equivalent initial tunneling conditions, we have averaged the bias voltage, at which the dissociation occurs. As a general trend, the molecules are found to dissociate at lower bias voltages for higher initial tunneling currents. Typically the bias voltage at which the dissociation occurs is smaller for negative then

for positive bias.
The dissociation process can be described by a similar model as has been proposed previously for the desorption induced by electronic transitions (DIET) as it occurs in photodesorption [31, 32]. The basic idea of the model is sketched in fig. 4.4(a). The negative ion resonance, where an electron is added to the $2\pi^\star$ orbital of the CO molecule [33] which is situated above the Fermi energy and is assumed to be of a lorentzian shape. By injecting tunneling electrons into this orbital, the molecule can be excited. The deexcitation can either proceed via interaction with the bulk or by a desorption or dissociation of the molecule. In order to describe our data, we have to take into account effects due to the tunnel junction. Furthermore, while recording a spectrum, the bias voltage is ramped. On one side this directly links the voltage scale to a time scale, on the other hand the model has to take into account the time dependence of the bias voltage.
The tunneling current is calculated within the Tersoff-Hamann picture for $T = 0$K as discussed in section 3.2

$$I \sim \int_0^{eV} \rho_\mathrm{s}(E)\rho_\mathrm{t}(E - eV)\mathcal{T}(E, V)\mathrm{d}E$$

with the tunneling probability $\mathcal{T}(E, V) = e^{-2s\sqrt{\frac{m_e}{\hbar^2}}\sqrt{\Phi_\mathrm{s}+\Phi_\mathrm{t}-2E+eV}}$ between tip and sample. The tunneling probability $\mathcal{T}$ depends on the tip-sample distance s and the work functions of tip and sample Φ_s and Φ_t. Since the tip is prepared by dipping it into the surface, we assume that $\Phi = \Phi_\mathrm{s} = \Phi_\mathrm{t}$. The tunneling barrier controls the energy distribution of the electrons which are transmitted. Thus it directly influences the number of electrons which can excite the resonance of the molecule.
The LDOS at the position of the molecule ρ_s is described by two terms: the LDOS $\rho_{\mathrm{s}0}(E) = \overline{\rho}_{\mathrm{s}0}$ of the Cu(100) substrate which is assumed be constant and the resonance of the molecule $\rho_\pi(E)$ which is spatially localized on the molecule:

$$\rho_\mathrm{s}(E) = \overline{\rho}_{\mathrm{s}0} + \rho_\pi(E)$$

The resonance is assumed to have a lorentzian shape of order n which accounts for multiple excitation [34]

$$\rho_\pi(E) = \frac{1}{\pi}\frac{\Gamma_\pi}{((E - E_\pi)^2 + \Gamma_\pi^2)^n}.$$

We introduce a "quantum efficiency" Q_0, which describes the part of the tunneling current which goes into the resonance. Furthermore, we assume

that the LDOS of the tip $\rho_t(E) = \overline{\rho}_t$ is constant within the energy range of interest. I obtain for the tunneling current $I_\pi(V)$ which goes into the resonance:

$$I_\pi(V) = Q_0 \int_0^{eV} \rho_\pi(E)\mathcal{T}(E,V)\mathrm{d}E.$$

$I_\pi(V)$ is implicitly a function of the time t since the voltage is ramped linearly during the measurement, $I_\pi(t) = I_\pi(V_0 + \Delta V \cdot t)$. The probability P, that the molecule dissociates at a time t is then

$$P(t) = \int_0^t I_\pi(\tau)P^*(t-\tau)\mathrm{d}\tau = I_\pi(t),$$

where $P^*(x)$ accounts for details of the decay process. We assume, that upon injection of an electron into the $2\pi^*$-orbital, it dissociates instantaneously, thus $P^*(x) = \delta(x)$.
If we had initially $N(0)$ molecules beneath the tip, after a certain time T,

$$N(T) = N(0)e^{-\int_0^T P(t)\mathrm{d}t}$$

molecules are left intact. From this we can calculate a mean lifetime of the molecules

$$\tau = \int_0^\infty \frac{N(t)}{N(0)}\mathrm{d}t. \tag{4.1}$$

Again it should be noted, that this lifetime τ corresponds to a voltage due to the constraint, that the bias voltage is ramped linearly. This integral can be calculated numerically. With all the simplifications introduced, the model is described by a total of eight parameters, 4 of which are fixed by the experimental conditions $(s, \Phi, V_0, \Delta V)$ and another 4 parameters have to be adjusted $(n, Q_0, E_\pi, \Gamma_\pi)$. We use $\Phi = 4.5$eV. Fig. 4.4(b) and (c) show the experimental curves for both bias polarities together with the calculation as described above. The experimental curves have been determined by destroying for each tunneling current several molecules and averaging the voltages at which the molecules dissociated. In fig. 4.4(c), we show also calculated curves for $n = 1, 2$ and 3. It is apparent, that the experimental data can only be well described with $n = 2$, indicating that two electrons need to be injected into the molecule before dissociation occurs. We can conclude, that the dissociation is a process of second order.
The values which we obtain from our model are summarized in table 4.1. For the negative ion resonance, where an electron is added to the $2\pi^*$ orbital, the

	E_π	Γ_π	n
neg. bias	-1.8eV	0.1eV	2
pos. bias	3.25eV	0.5eV	2

Table 4.1: Summary of the parameters extracted from the fit as described in the text.

energy we determine from our model is rather close to experimental values for CO on Cu(111) obtained from 2PPE measurements by Bartels *et al.* [35]. They observe the negative ion resonance at 3.5eV with a width of ~ 0.8eV. The positive ion resonance is apparently closer to the Fermi energy. In both cases, the dissociation occurs only if two electrons are injected into the $2\pi^*$ orbital.

Chapter 5

Quantum Coherence of Image-Potential States

5.1 Introduction

The image-potential states are model states for the study of electronic interactions of electrons at surfaces, a topic that has immediate consequences for many surface processes. The self interaction of electrons near metallic surfaces gives rise to eigenstates which are confined along the surface normal by the classical image potential on the vacuum side of the crystal surface and by the band structure of the crystal on the other side [36]. The lifetime of electrons injected or excited into an image-potential state is limited mainly by their interaction with bulk electrons. This has been studied in great detail in recent years by energy- and time-resolved two-photon photoemission spectroscopy (2PPE) [37, 38, 39, 40]. Theoretical understanding of the involved electron-electron scattering processes has established that the lifetime of image-potential-state electrons is determined by interband scattering with bulk electrons and by intraband contributions [38, 41].
The high LDOS of the image-potential states near the surface makes them accessible to STM. They appear at rather high sample bias voltages of $4-8$V. The electric field between tip and sample induces a Stark shift of the eigenenergies to higher values. Interest in image-potential states modified by the presence of an STM tip has focused so far on the fact that the energetic positions of the states are sensitive to the electronic structure of the surface [42, 43]. Spectroscopy of image-potential states by STM has been used to

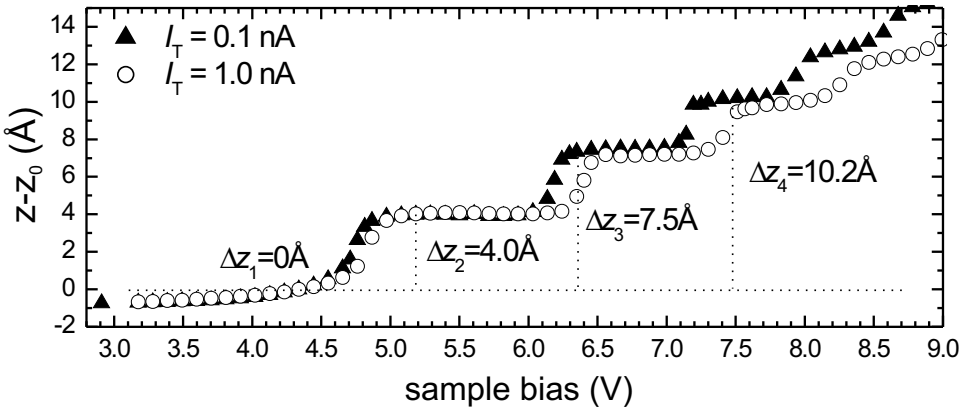

Figure 5.1: Measured $z(V)$ curve on a terrace of Cu(100) using two different tunneling currents of 0.1 and 1.0nA. We observe up to four image-potential states in the electric field of the STM tip. The measured increments in the tip-sample distance are labelled Δz_n.

achieve chemical contrast on the nanometer scale for metals on metal surfaces, e.g. Cu on Mo(110) [43] or Fe/Cr surface alloys [44].
Here, I present STM measurements of the dynamical properties of the image-potential states in front of the surface. Due to elastic scattering at point defects and step edges of the electrons injected into these states, modulations of the LDOS emerge. Using STS, we determine the energies for the first four image-potential states as well as the dispersion relation and the phase coherence length of the $n = 1$ Stark-shifted image-potential state on Cu(100). This opens up the possibility to study these quantities locally in nanostructures. In the case of surface state electrons at metal surfaces the local dynamics has been studied by STS in great detail [45, 46, 47, 48]. The results show a good agreement between photoemission and STS experiments on the one side and theory on the other side [47, 48]. A similar comparison is missing in the case of image-potential states.

5.2 Characterization of Image Potential States

The energies of the Stark-shifted image-potential states can be measured using $z(V)$ spectroscopy as shown in Fig. 5.1. For this experiment the feedback loop is kept active while sweeping the bias voltage. To maintain a constant current the tip is retracted with increasing bias voltage as more and more states become available to the tunneling electrons. We have taken $z(V)$-spectra at currents of 0.1 to 1nA. The spectra show a series of steps, where each step is due to the contribution of a new image-potential state to the tunneling current allowing us to identify the first four image-potential states. Their energies E_n relative to the vacuum level E_{vac} of the sample are obtained from the bias voltages V_n, at which the steps occur by

$$E_n = eV_n - \Phi \tag{5.1}$$

where $\Phi = 4.6$eV [40] is the work function of Cu(100) and e the elementary charge. Note that the states appear above the vacuum level of the substrate but nevertheless they are bound in z-direction by the tip and crystal potential respectively. From the absence of any features in $z(V)$ below 3V we identify the step at $V = 4.7$V as the state $n = 1$. The energies are considerably larger compared to the unperturbed states which form a Rydberg series below E_{vac} starting at -0.6eV[49, 38]. As can be seen from a comparison of the two spectra shown in Fig. 5.1, the states shift to higher energies for higher tunneling currents due to the decreased tip-sample distance. Measurements with different tips, i.e. tips that have been modified by field emission and gentle dipping into the surface, reveal a dependence of the energy levels on the tip properties which is stronger for the higher states. While the $n = 1$ state remains at a bias voltage of 4.7 ± 0.1V, we observe the higher states to shift by as much as 0.5V ($n = 2$) and 0.9V ($n = 3$). This yields a much stronger dependence of the energy levels on tip properties than on tunneling conditions, i.e the current at which the $z(V)$ spectroscopy is performed. To understand these findings we performed model calculations using a one-dimensional potential as introduced by Chulkov *et al.* [49]. This potential reproduces the Rydberg series of the image-potential states and the positions of the projected band edges at the $\overline{\Gamma}$ point ($k_{\parallel} = 0$) in the Cu(100) surface Brillouin zone. We integrated the Schrödinger equation in real space employing the model potential for a 25 layer crystal. The influence of the tip is modelled by adding as function of the bias voltage a linearly increasing potential to the image potential of the crystal reaching from the point z_{im} (see Ref. [49])

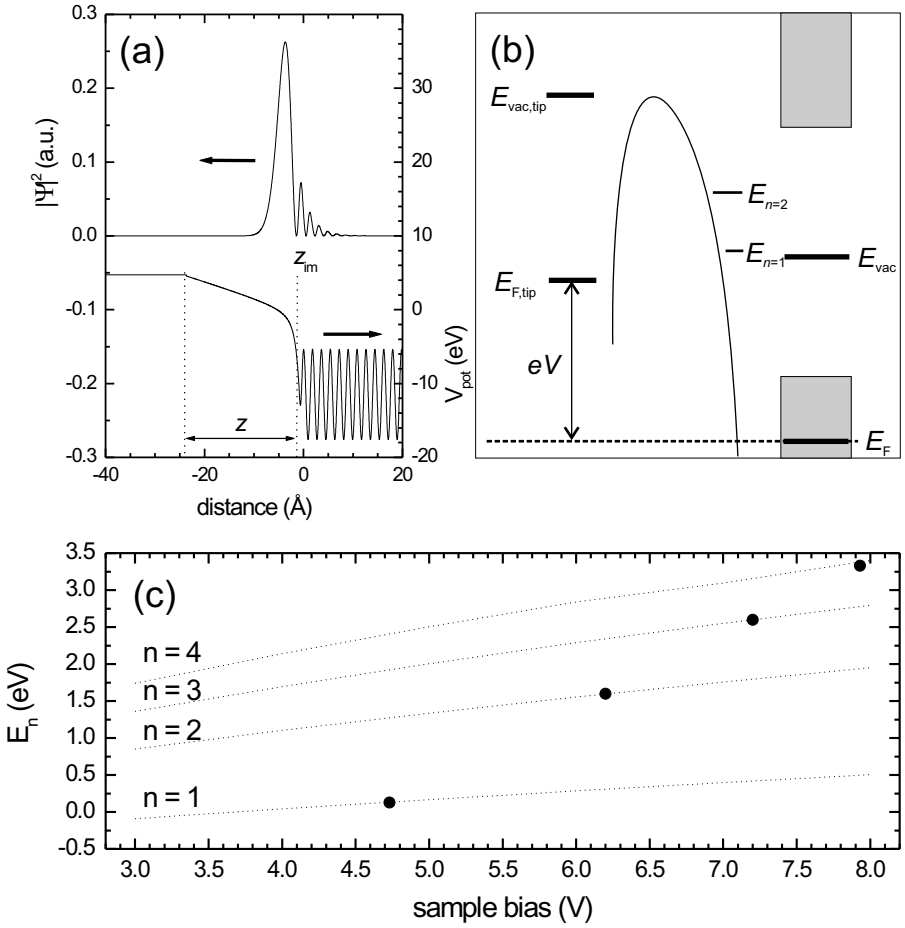

Figure 5.2: (a) one-dimensional model potential used and probability density of the wave function of the first image-potential state obtained. (b) schematic drawing of the energy levels of the resonances, the Fermi levels of tip and sample, the bulk band edges of the Cu(100) crystal ($E(X_{4'})$ and $E(X_1)$) and the potential in the tunneling gap. (c) calculation (dotted lines) of the energies of the image-potential states in the electric field of the STM tip as function of the applied voltage. Each of the dotted lines corresponds to one particular state ($n = 1$ to 4) calculated for a tip-sample distance $z = \Delta z_n + z_0$, where Δz_n is taken from the measurement shown in Fig. 5.3(b) and $z_0 = 22.5$Å. Full circles are plotted at the voltages where the steps in Fig. 5.3(b) occur and at the corresponding energies according to Eq. 5.1.

to the point $z_{\mathrm{im}} + z$ where z is the tip-sample distance. A similar ansatz has been used in Ref. [50]. Since the change in tip-sample distance is given by the plateaus Δz_n (Fig. 5.1) we use $z = \Delta z_n + z_0$ and treat z_0 as the only adjustable parameter in the model assuming equal work functions of tip and sample. This choice was made in favor of discussing the average electric field in the junction [42] since it allows to separate V as externally controllable parameter from details of the potential. The model potential and the probability distribution of the resulting wave function are shown in Fig. 5.2(a). Fig 5.2(b) shows schematically the resulting energy level diagram. In such a simple model, the energies E_n of the image-potential states in the electric field of the STM tip are reproduced for all n observed. This is shown in Fig. 5.2(c), where the calculated energies E_n are plotted as a function of the applied bias voltage for $z_0 = 22.5$Å corresponding to the measurement with a tunneling current of 0.1nA. The agreement is excellent. To reproduce the energy levels for the measurement at a current of 1nA a $z_0 = 19.5$Å is found. We emphasize that there is no need for an n-dependent "surface-corrugation parameter"as was employed earlier [42]. To arrive at the expected smaller z_0 values of 8 to 10Å [51] one has to improve the treatment of the tip electrode. The detailed inclusion of the image potential at the surface of the tip in a calculation using two Cu(100) model potentials facing each other yielded z_0 values which were $3 - 5$Å lower than the ones found above. On the other hand, the radius of curvature R of the tip can be neglected. Only for unrealistically sharp tips with $R \approx z$ the potential near the tip will fall off appreciably more quickly than the linear potential. We conclude that to explain the variation of the E_n with different tips the contact potential and not the tip radius is the decisive quantity. From the experimental point of view it is quite likely that the tungsten tip is coated with copper, since it is frequently prepared by slightly dipping it into the surface. Both, the composition and the morphology of the very end of the tip can lead to a lower work function compared to that of the Cu(100) surface, which can be compensated for by a reduced z_0.

Fig. 5.3(a) shows a typical STM image of an artificially created step edge. While the topographic image just shows the step edge, the simultaneously acquired $\mathrm{d}I/\mathrm{d}V$-map in fig. 5.3(b) taken at the same bias voltage reveals the quantum interference patterns. They are due to elastic scattering of electrons injected by the tip into the $n = 1$ image-potential state. Circular standing waves around point defects were also observed. (Not shown here.)

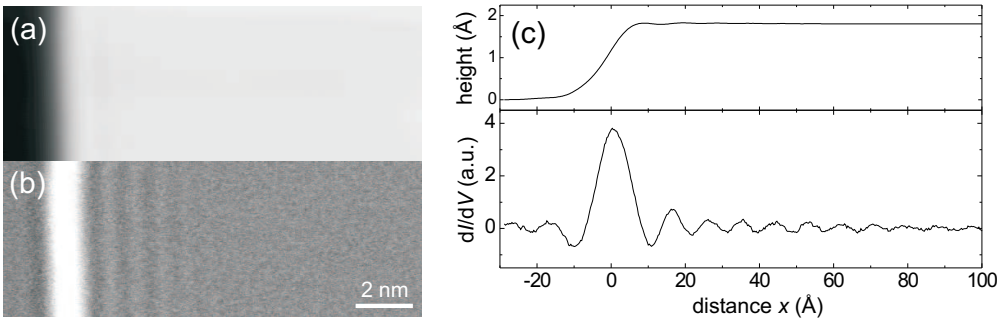

Figure 5.3: (a) STM topography of an artificially created step on Cu(100) taken at 5.2V bias voltage, (b) dI/dV-map of the same place at the same bias voltage. The image-potential-state electrons reflected at the step edge create a density modulation which appears as a standing wave pattern in the dI/dV-map. (c) Line cut through (a) and (b) showing clearly the oscillations in the dI/dV-map.

5.3 Coherence Length of Electrons in Image Potential States

In the following, the dynamics of electrons injected into the $n = 1$ image potential state will be discussed in detail. Due to elastic scattering of these electrons at point defects and step edges, modulations of the LDOS are created through quantum interference (Fig. 5.3(b) and (c)). This allows to study the dynamics of the states with non-vanishing momentum parallel to the surface locally. The analysis of the interference pattern of electrons scattered at a step edge enables the determination of their wave vector and phase coherence length as a function of energy. This way to measure the phase coherence length and thus the lifetime of the electronic state has been first introduced by L. Bürgi *et al.* [46]. The interference pattern is measured through the dI/dV signal which is proportional to the LDOS at the given energy. In Fig. 5.4(a) dI/d$V(V, x)$ is measured for bias voltages ranging from 4.6V to 5.6V at increasing distances x from the step edge. The resulting curves are represented as a grey scale map, where horizontal line sections are the energy resolved electron density oscillations as shown in Fig. 5.4(a). The density oscillations reveal the parabolic dispersion relation of the state with

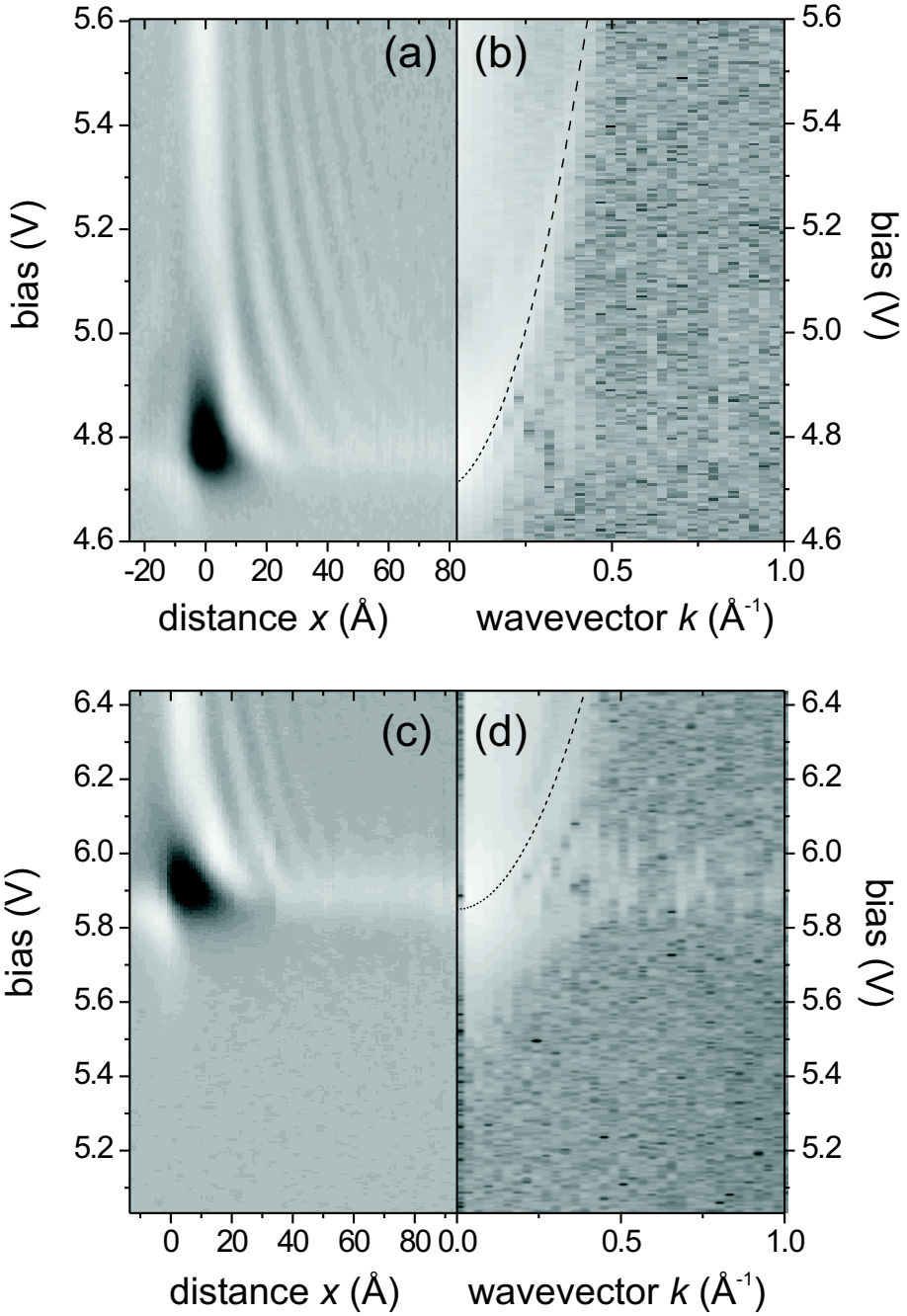

Figure 5.4: (a) $\mathrm{d}I/\mathrm{d}V(V,x)$-map for the $n=1$ image state, $\mathrm{d}I/\mathrm{d}V$ is plotted as a function of the lateral distance x from a step edge and of the bias voltage V. Horizontal line cuts reveal the standing waves due to the interference of electrons in the image-potential state scattered at the step edge. (b) shows a line-by-line Fourier transform of the $\mathrm{d}I/\mathrm{d}V(V,x)$-map, revealing the parabolic dispersion (marked by the dashed line as a guide for the eye). (c) $\mathrm{d}I/\mathrm{d}V(V,x)$-map and its Fourier transform (d) for the $n=2$ image state. To enhance the contrast, in the maps shown in (a) and (c), the average intensity of each line has been subtracted.

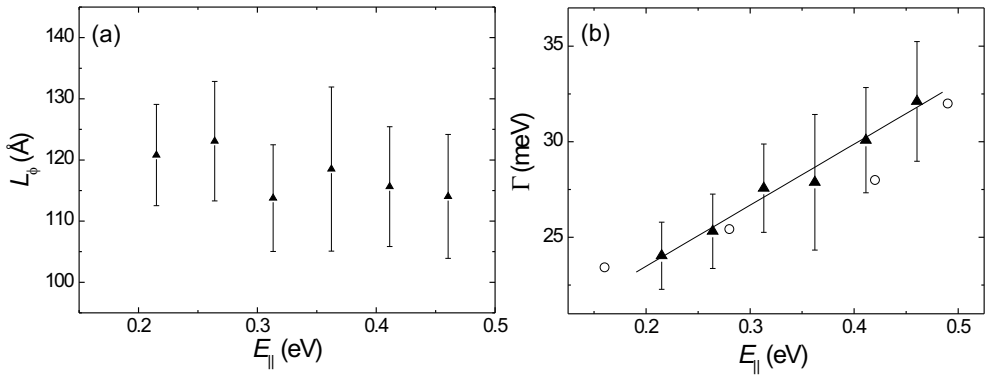

Figure 5.5: (a) Phase coherence lengths of the interference pattern at a step edge, (b) corresponding linewidths $\Gamma(E)$. Solid symbols are the data taken by STM, the solid line is a linear fit to them; open symbols represent linewidths determined by 2PPE measurements from Ref. [38].

$E'_{\overline{\Gamma}} = 4.7 \pm 0.1$eV and $m' = (0.8 \pm 0.1)m_0$. A greyscale map of the modulus of the line-by-line Fourier transform of the $\mathrm{d}I/\mathrm{d}V(V,x)$-map as shown in Fig. 5.4(b) reveals the parabolic dispersion. It can be seen as a bright rim, as a guide to the eye, the dispersion relation as obtained from the fit is also plotted in fig. 5.4(b). With the help of the calculations presented above, the influence of the tip on the dispersion of the image-potential state can be corrected for. Since the data are collected in open feedback mode, i.e. the distance between tip and sample is kept constant, one needs only to compensate for the shift of the energy at $\overline{\Gamma}$ with changing electric field during the bias voltage sweep. The dependence of the state's energy on the applied bias voltage close to $E'_{\overline{\Gamma}}$ is approximately linear. From the calculations shown in Fig. 5.2(c) we get $\mathrm{d}E_1/\mathrm{d}V = 0.12$. Using this correction, we obtain an effective mass of $m^* = m'/(1-0.12) = (0.9 \pm 0.1)m_0$. This agrees perfectly with the effective mass $m^* = 0.9m_0$ of the $n = 1$ image-potential state as determined by 2PPE [40]. A similar measurement for the $n = 2$ image state has been performed (fig. 5.4(c) and (d)). The obtained effective mass of the $n = 2$ state is $m^* = (1.0 \pm 0.1)m_0$. A similar increase in the effective mass for $n = 2$ was also observed by 2PPE [52].

The standing wave pattern decays with increasing distance from the step edge due to geometric factors and to a loss of coherence [53, 46]. The decay-

ing LDOS pattern formed by the image-potential states near a step edge can be described by

$$\rho \propto \left(1 - re^{-2x/L_\Phi} \mathrm{J}_0(2k_\parallel x)\right). \tag{5.2}$$

This formula contains the reflectivity of the step edge r, the phase coherence length of the electron L_Φ and the wavevector parallel to the surface $k_\parallel$. Additional sources of broadening leading to a loss of coherence are the finite measurement temperature, which enters through the Fermi broadening and the lockin detection technique. The Fermi broadening can be accounted for by applying the Adawi approximation [54, 53], leading to

$$I(V,T,x) \propto -\frac{1}{x}\left(\frac{\xi_{k_{eV}}}{\sinh\xi_{k_{eV}}} k_{eV}\mathrm{J}_1(2k_{eV}x)e^{-\frac{2x}{L_\Phi}} - \frac{\xi_{k_\mathrm{F}}}{\sinh\xi_{k_\mathrm{F}}} k_\mathrm{F}\mathrm{J}_1(2k_\mathrm{F}x)\right). \tag{5.3}$$

The broadening due to the lockin modulation is introduced by calculating numerically the lockin derivative according to eq. 3.8. Note that the second term in eq. 5.3 which describes the oscillations in the LDOS at the Fermi energy does not depend on the applied bias voltage and thus does not contribute directly to the lock-in derivative. Consequently, the error which is introduced by assuming that the decay length at the Fermi level $L_\phi(E_\mathrm{F}) \to \infty$ can be neglected. However it should be kept in mind that the second term does enter the $\mathrm{d}I/\mathrm{d}V$-signal through the height variations it induces.
To determine the lifetime of an electron in the $n = 1$ image-potential state we have analyzed quantitatively the quantum interference pattern and measured the phase coherence length L_ϕ as a function of energy on large defect free terraces. The scattering processes thus studied are those experienced in the absence of any defects [46, 48]. Inelastic scattering at the step edge leads to a reduced overall amplitude of the standing waves described by r in Eq. 5.2. Care was taken to account for instrumental broadening through the applied bias modulation when measuring the $\mathrm{d}I/\mathrm{d}V$ signal which also induces a decay of the wave pattern [46]. The obtained phase coherence lengths of $75 - 85$Å are converted into linewidths through $\Gamma(E) = \hbar^2 k/(m^* \cdot L_\phi(E))$ by using the measured k and m^* according to the dispersion relation (Fig. 5.4). In Fig. 5.5(a), the phase coherence lengths $L_\phi(E)$ are plotted, in (b) the corresponding linewidths. They agree excellently with the k-resolved linewidths found by 2PPE measurements [38]. In agreement with theory, we find $\Gamma(E)$ to increase linearly with energy, although the rate of $\mathrm{d}\Gamma/\mathrm{d}E = 32\mathrm{meV/eV}$ obtained from the fit in Fig. 5.5(b) is lower than the theoretical prediction [38]. The comparison of our results with the 2PPE measurements demonstrates

that the presence of the tip does not alter substantially the dynamical properties of electrons in the image-potential states. Although the $n = 1$ state shifts by as much as 0.7eV due to the presence of the electric field, it is still located near the center of the $\sim$ 6eV wide directional band gap of Cu(100). There is thus no significant change in the coupling to the bulk electrons, which is the main contribution to the linewidth.
It should be noted that the band gap is essential for the standing wave patterns to be detectable by STM. While for Ag(100), where the image states are also situated within a directional band gap the standing wave patterns can be observed similar to Cu(100), we have not been able to resolve them on Cu(111). There, the image state is a resonance with a much shorter lifetime of electrons injected into it.

Chapter 6

The Kondo Physics of Single Impurities

6.1 Introduction

The first observations of the Kondo effect have been performed already 70 years ago [5]. The resistivity of non-magnetic metals with minute amount of magnetic impurities as a function of temperature revealed a minimum at a finite temperature. An example is shown in fig. 6.1(a). This anomalous behaviour could be explained neither by electron-phonon scattering nor by simple impurity scattering. Both lead to a monotoneous decrease or a constant background with decreasing temperature. It was not until the sixties, that this riddle has been solved: Magnetic impurities undergo at sufficiently low temperature spin-flip scattering. The spin-flip scattering cross-section increases the lower the temperature becomes.
It is only recently, that interest in the Kondo effect has revived through two experimental developments allowing the study of the Kondo effect of a single spin impurity. On one hand, the investigation of Kondo phenomena in quantum dots became possible [7, 8]. Quantum dots are providing model systems where the Kondo effect can be studied in an artificial atom. The parameters of the Kondo problem can be tuned easily by adjusting electrode potentials. On the other hand, by low-temperature scanning tunneling microscopy (STM) and spectroscopy (STS) the Kondo effect of single magnetic adatoms could be studied. The spectroscopic signature of the Kondo effect, the Kondo resonance, of single adatoms has been first observed by STS for

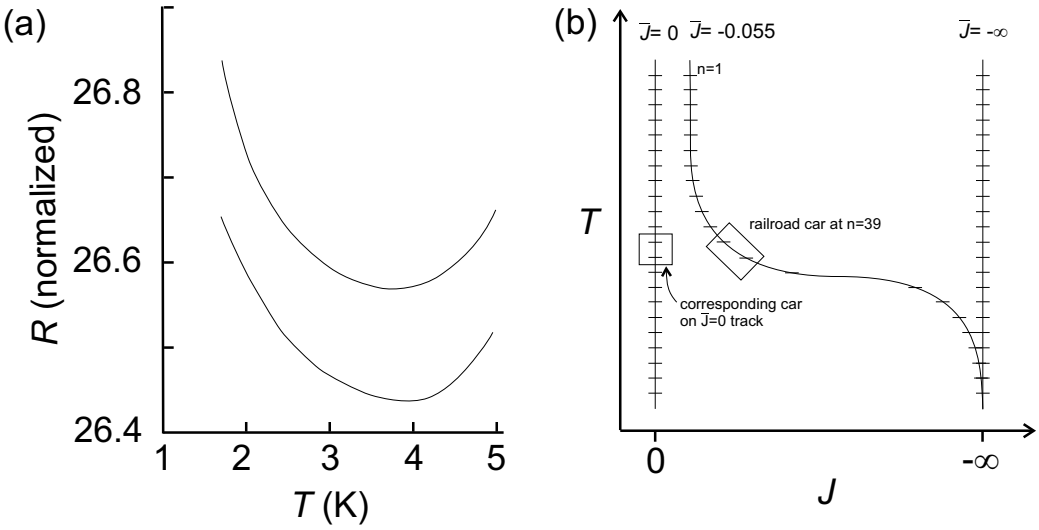

Figure 6.1: (a) Low temperature resistivity of a gold sample with magnetic impurities at different impurity concentrations [5]. (b) "Railroad track analogy" by Wilson [55] describing the crossover.

cobalt adatoms on Au(111) [3] and cerium on Ag(111) [9].
In the following I will first discuss the two principal models which have been applied to the Kondo problem. The first, the Kondo model [6], is only discussed because it offers a more intuitive view of the physics involved, whereas the second - the Anderson model [56] - allows a more complete description of the physics of a magnetic impurity in a metallic host. The experimental section is first concerned about STS measurements on single adatoms, in the last section these results are extended to systems consisting of coupled impurities.

6.2 Theory

6.2.1 Kondo model

The Kondo model describes the behaviour of a magnetic impurity by only considering the exchange interaction J between the spin of the impurity and

the spins of the conduction band electrons. The Kondo Hamiltonian

$$H = \sum_{k,\sigma} \epsilon_k n_{k\sigma} - J \sum_{k,k'} \left(\left(c^+_{k\uparrow} c_{k'\uparrow} - c^+_{k\downarrow} c_{k'\downarrow} \right) S_z + c^+_{k\uparrow} c_{k'\downarrow} S_- + c^+_{k\downarrow} c_{k'\uparrow} S_+ \right) \quad (6.1)$$

consists of four parts: the first term deals with the conduction band electrons, the second with potential scattering of the conduction band electrons at the impurity taking into account the spin of the impurity. The last two terms are those describing the spin-flip scattering: Both the spin of the impurity and the spin of the electron scattered at the impurity flip their spin simultaneously.
The solutions of this Hamiltonian can be calculated perturbatively in J. However, it turns out that for antiferromagnetic coupling ($J < 0$) between the impurity spin and the conduction electrons, the perturbation expansion breaks down for temperatures $T < T_\mathrm{K}$, with

$$k_\mathrm{B} T_\mathrm{K} \sim D e^{-\frac{1}{2J\rho_0}}. \quad (6.2)$$

D is the width of the conduction band and ρ_0 the density of states of the unperturbed host at the Fermi level.
Thus for sufficiently low temperatures the exchange interaction between the conduction band electrons and the spin of the impurity becomes dominant compared to thermal excitation energies and electron correlation has to be taken into account. At these low temperatures, the spin of the impurity is effectively screened by the conduction band electrons, and a non-magnetic singlet state forms thereby lowering the energy.
It is the crossover between a behaviour dominated by thermal excitations for temperatures T larger than the charateristic Kondo temperature T_K to a regime where the exchange interaction J governs the properties of the magnetic impurity which is commonly termed the Kondo problem. The physics of the crossover has first been theoretically calculated for the Kondo Hamiltonian by K.G. Wilson [55] within the framework of renormalization group theory – which brought him later the nobel prize. Wilson nicely sketched the crossover in his review paper [55] by drawing a "railroad track analogy" (see fig. 6.1(b)): with decreasing temperature, the system evolves from the local moment regime $J \to 0$ where the impurity carries a spin, is basically decoupled from the conduction band and has a magnetic moment to the strong coupling regime $J \sim -\infty$, where the spin is screened by the conduction electrons.

6.2.2 Spin-$\frac{1}{2}$ Anderson model

While the Kondo model offers a simple physical picture for a magnetic impurity in a metal host, it does not allow any prediction about whether an impurity does carry a spin after it has been emersed into the host. This is where the Anderson model comes into play. It describes the magnetic impurity to consist of a single singly occupied atomic orbital at energy ϵ_d, which is for a transition metal atom the d-orbital. The double occupation of the d-orbital is inhibited by the on-site Coulomb respulsion U between the two electrons. If the magnetic atom is brought in contact to or emersed into a metal, the d-orbital acquires a finite width Δ due to hybridization. The Hamiltonian of the Anderson model reads

$$H = \sum_{\mathbf{k},\sigma} \epsilon_k n_{\mathbf{k}\sigma} + \epsilon_{\mathrm{d}} \sum_{\sigma} n_\sigma + \sum_{\mathbf{k},\sigma} V_{\mathrm{d}k} \left(c^+_{\mathbf{k}\sigma} c_{\mathrm{d}\sigma} + c^+_{\mathrm{d}\sigma} c_{\mathbf{k}\sigma} \right) + U n_{\mathrm{d}\uparrow} n_{\mathrm{d}\downarrow}. \tag{6.3}$$

Again, the first term describes the conduction band of the metal, while the following three terms describe the d-level at the impurity site, its interaction with the conduction band electrons and the Coulomb repulsion.
The Anderson model has first been solved by Anderson self-consistently within a Hartree Fock treatment. Although this treatment neglects many-body effects and thus cannot explain the Kondo behaviour of a dilute magnetic alloy it already gives an idea about whether a magnetic atom stays magnetic when brought into contact with a metal. The solutions are shown graphically in fig. 6.2(a). It can be clearly seen, that magnetic and nonmagnetic solutions coexist. While in the symmetric case ($\epsilon_{\mathrm{d}} = -\frac{U}{2}$ corresponding to $x = -\frac{\epsilon_d}{U} = 0.5$) the impurity is almost always magnetic (except for $U < \Delta$), the spin can be quenched by the hybridization with the conduction band for $x < (>) 0.5$. Thus the Anderson Hamiltonian can not only describe the Kondo regime but also non-magnetic as well as mixed-valence behaviour. The latter describes the regime in which charge and spin fluctuations are equally important, which is the case when $|\epsilon_d| \sim \Delta$.
If solved in a many-body treatment, the Anderson Hamiltonian can show Kondo behaviour depending on the parameters. In the Kondo regime, the Kondo Hamiltonian is equivalent to the Anderson model. Both are connected by the Schrieffer-Wolff transformation [57], which relates the parameters Δ, U and ϵ_d of the Anderson model to the exchange coupling J of the Kondo model:

$$J = \frac{\Delta}{\pi \rho_0} \left(\frac{1}{\epsilon_d + U} - \frac{1}{\epsilon_d} \right). \tag{6.4}$$

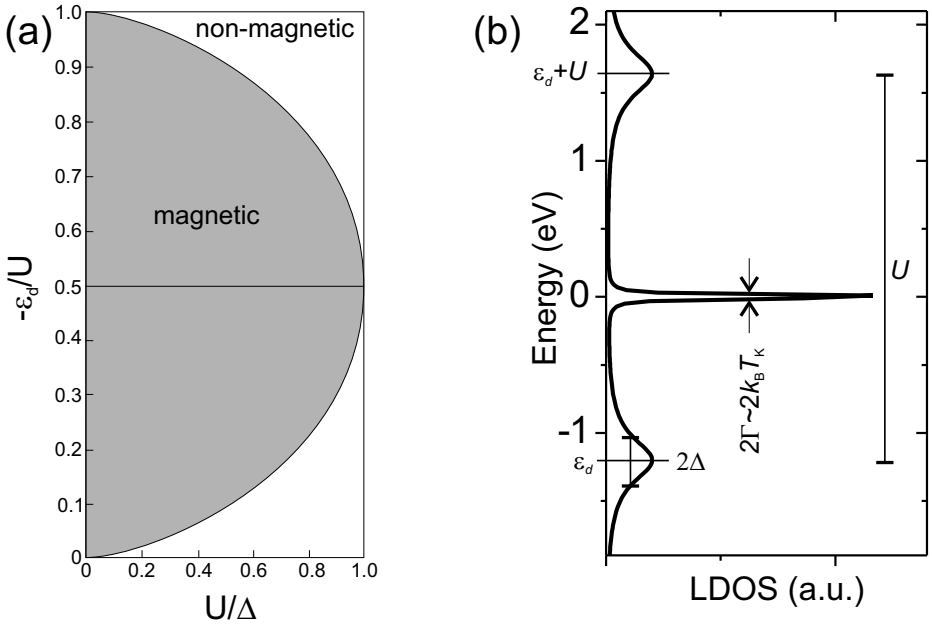

Figure 6.2: (a) Solutions of the Anderson model (graph taken from ref. [56]). x is a reduced parameter $x = -\frac{\epsilon_d}{U}$. The shaded area is the region of magnetic solutions in a (single particle) Hartree-Fock treatment. (b) Spectral density of the spin-$\frac{1}{2}$ Anderson model.

In the Anderson model, the Kondo Temperature T_K can be calculated from [58]

$$k_\mathrm{B}T_\mathrm{K} \sim \sqrt{\frac{\Delta \cdot U}{2}} e^{-\frac{\pi}{2\Delta \cdot U}|\epsilon_d+U|\cdot|\epsilon_d|}. \tag{6.5}$$

This formula expresses T_K in terms of the parameters ϵ_d, U and $\Delta \approx \pi V_{\mathrm{d}k}^2 \rho_0$ of the Anderson model. The singlet state which is formed at temperatures $T < T_\mathrm{K}$ has a peak in the LDOS which is close to the Fermi energy. As opposed to the Kondo model, the peak is shifted slightly away from the Fermi level due to level repulsion. The resulting spectral density within the Anderson model is shown in fig. 6.2(b). Besides the broad peaks of the hybridized d-level of the impurity at ϵ_d and $\epsilon_\mathrm{d} + U$, it shows a very narrow peak at the Fermi level – the so-called Kondo peak. To the width of the Kondo peak, a time scale $\tau_\mathrm{S} \sim \frac{\hbar}{k_\mathrm{B}T_\mathrm{K}}$ can be associated and thus a length scale $\xi = v_\mathrm{F}\tau_\mathrm{S}$ which should give an estimation for the spatial extent of the many body state. Typical estimates for the size of this "Kondo cloud" are about $10 - 100$nm.

6.2.3 Kondo and STS

In STS measurements, the Kondo effect can be sensed due to the prominent peak near the Fermi energy. But experiments have shown, that although the spectra recorded with the tip placed above a magnetic impurity show a distinct feature at the Fermi energy, it is generally not a peak but can acquire a large range of line shapes. Mathematically, the line shape has been successfully described by the Fano function [59]

$$\frac{\mathrm{d}I}{\mathrm{d}V} = a\frac{(q+\tilde{\epsilon})^2}{1+\tilde{\epsilon}^2} + b + c\cdot\omega, \tag{6.6}$$

where $\tilde{\epsilon} = \frac{\omega-\epsilon_\mathrm{K}}{\Gamma}$ and $\omega = e \cdot V$. Γ is the half width of the resonance, ϵ_K its position. a is a proportionality constant. The line shape is described by q and can vary between a dip for $q = 0$, an asymmetric feature for $q \sim 1$ and a peak for $q > 2$. In the limit $q \to \infty$, eq. 6.6 becomes a lorentzian. b and c account for a constant or linear background respectively. The Fano line shape has originally been introduced to describe the coupling of a discrete level to a continuum of states and the resulting spectroscopic line shape [59]. In the context of STM measurements, the analogy for the discrete level is the Kondo state, while the continuum of states is the conduction band of the

substrate [60].
The physical interpretation of the line shape and hence q in STS experiments is still under disscussion. Mainly two models have been suggested: the first proposes that the line shape can be understood by taking into account two tunneling channels between the tip and the surface – a direct channel, which couples the tip to the impurities d-level, and an indirect channel probing the Kondo peak via the substrate states [61, 62, 63]. The coherent superposition between the two leads to the features observed in STS. The existence of interfering tunneling channels implies, that the line shape depends on the lateral and vertical position of the tip since this will change the relative strengths of the two channels. Recently, a second model has been put forward [64, 65], where the direct channel is neglected and the line shape is interpreted to be only due to the indirect channel. The parameter q depends on the detailed electronic structure of the substrate and the hybridization with the impurity [64]. Since only one tunneling channel contributes, neither lateral nor vertical movement of the tip should have a considerable influence on the line shape.

6.3 Magnetic Impurities

6.3.1 Co/Cu(100) and Fe/Cu(100)

Fig. 6.3(a+b) show the tunneling spectra as recorded on single magnetic adatoms on the Cu(100)-surfaces. While Co/Cu(100) shows a rather broad feature near the Fermi level [30], an iron adatom shows a much narrower feature. Also the line shape varies, it is close to a dip for the latter while for Co/Cu(100) the resonance is quite asymmetric. From the fit of a Fano function (eq. 6.6), the Kondo temperature can be extracted. For Co/Cu(100) it is 88K, while for an iron adatom it is only around 50K.

Based on a comparison of the Kondo temperature of Co/Cu(100) with that of Co/Cu(111) which is only about 54K [66, 30] and that of Co in bulk copper of about 500K, the first attempt to understand the variations in the Kondo temperature was based on a linear scaling of the exchange coupling J in the Kondo model with the number of nearest neighbours [30]. A cobalt adatom sitting in a hollow site has three nearest neighbours on Cu(111), four on Cu(100) and twelve in bulk copper.
The reduction of the Kondo temperature when changing the adatom from

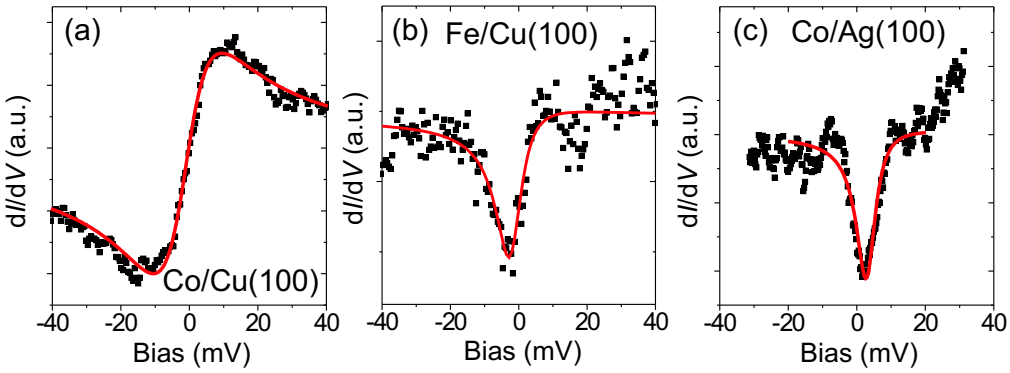

Figure 6.3: Background subtracted spectra taken on magnetic adatoms: (a) Co/Cu(100), (b) Fe/Cu(100) and (c) Co/Ag(100). The solid line depicts the fit of a Fano line shape (eq. 6.6) to the data.

cobalt to iron can be understood from the degeneracy of the d level which is responsible for the Kondo effect. Considering the degeneracy N in the Kondo model yields [67]

$$T_{\mathrm{K}} = De^{-\frac{1}{2(J/N)\rho_0}}, \tag{6.7}$$

which means that the higher N, the lower the Kondo temperature. For an iron adatom, the degeneracy of the d-level will be higher than for a cobalt adatom due to the lower occupation of the d-level.

6.3.2 Co/Ag(100)

A typical tunneling spectrum, which we measure with the tip placed above a single cobalt adatom on Ag(100), is shown in Fig. 6.3(c). The spectrum shows a distinct dip slightly above the Fermi energy. The line shape is the same as for Co/Ag(111) [68]. The solid line results from the fit of a Fano function (eq. 6.6) to the data. The Kondo temperature calculated from the width of the resonance and averaged over several different atoms and tips is 41 ± 5K. This value, which is lower than that for Co/Ag(111), indicates that the scaling of the Kondo temperature solely based on the number of nearest neighbours of the cobalt adatom as proposed for cobalt on copper surfaces [30] has to be amended.

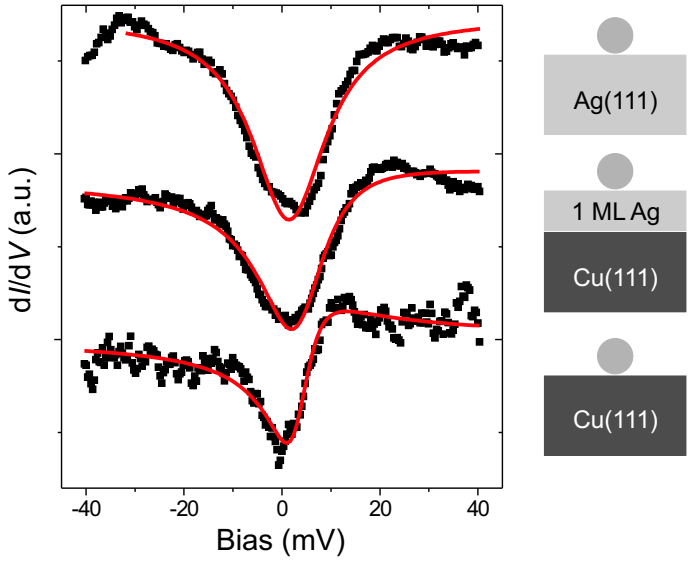

Figure 6.4: Spectra taken on a cobalt adatom on (from bottom) Cu(111), one monolayer of Ag on Cu(111) and on Ag(111) (data shifted vertically).

6.3.3 Overlayer systems

As we have seen, the Kondo temperature depends on the coordination of the impurity in a non-trivial way. In order to investigate the influence of a change in the chemical environment of the impurity on its Kondo behaviour, we have performed experiments on single monolayers of Ag on Cu(111). About half a monolayer of Ag has been deposited from an electron beam heated evaporator at a sample temperature of 300K. After transfer of the sample into the STM, we have deposited single cobalt adatoms onto the substrate. The surface exhibited silver islands with a size of several nanometers on the copper substrate, so we could measure STS spectra with the same tip on a cobalt adatom on a silver island and on the clean copper substrate. The spectra are shown in fig. 6.4 together with a spectrum for a cobalt adatom on Ag(111). We find that the Kondo temperature does not change gradually from that on Cu to that on Ag, but that there is an immediate change already after the first monolayer of Ag. This shows that the Kondo behaviour of the impurity is governed by its local environment, whereas other parameters of

Substrate	T_K [K]	q	ϵ_K [meV]	a [Å]	n_{NN}	β	n_d	Ref.
Cu(111)	54 ± 2	0.18 ± 0.03	1.8 ± 0.6	2.53	3	0.239	0.94	[30]
	53 ± 5							[66]
Cu(100)	88 ± 4	1.13 ± 0.06	-1.3 ± 0.4	2.53	4	0.319	1.16	[30]
Ag/Cu(111)	92 ± 10	0.15 ± 0.10	2.3 ± 1.0	2.7	3	0.202	0.84	*
Ag(111)	92 ± 6	0.0 ± 0.1	3.1 ± 0.5	2.7	3	0.202	0.84	[68]
Ag(100)	41 ± 5	0.0 ± 0.2	2.0 ± 1.1	2.7	4	0.269	1.02	*
Au(111)	76 ± 8					0.203	0.84	[70]
	75 ± 6	0.60 ± 0.05	6.5 ± 0.5	2.695	3	0.203	0.84	[62]

Table 6.1: Summary of Kondo temperatures for cobalt adatoms on the noble metal surfaces together with the parameters a and n_{NN} which enter our model. β is calculated according to Eq. 6.9 and n_d is obtained from the fit of Eqs. 6.8-6.10 as described in the text. Data marked by a star are new data published in this work.

the substrate such as the work function, the surface state or the bulk band structure play a minor role [69]. This is surprising in view of the fact that the electrons participating in the many body state are close to the Fermi energy and spatially delocalized.
A similar behaviour is found for cobalt adatoms on one and two monolayers of Ag on Au(111). Again, the Kondo behaviour of a cobalt adatom is already on one monolayer of Ag on Au(111) the same as on a bulk Ag(111) sample [69].

6.3.4 Scaling behaviour

The Kondo temperatures as well as the lineshapes for Cobalt adatoms on Ag(100) and on other noble metal substrates are listed in table 6.1. Based on the observation that the Kondo resonance is governed by local interactions we propose a model which explains the observed trend in the Kondo temperatures and the position of the resonance ϵ_K. Following Újsághy *et al.* [61], Eq. 6.5 can be expressed in terms of the occupation $n_d = -\frac{\epsilon_d}{U} + \frac{1}{2}$ of the d-level. Thus the properties of the adatom as derived from a single particle model can be mapped on an effective spin-$\frac{1}{2}$ Anderson model. This results in

$$k_B T_K \sim \sqrt{\frac{\Delta \cdot U}{2}} e^{-\frac{\pi U}{2\Delta}|-n_d+\frac{3}{2}|\cdot|-n_d+\frac{1}{2}|}. \tag{6.8}$$

In the following, we use $\Delta = 0.2$eV and $U = 2.84$eV which have been determined from DFT calculations [61]. The calculations yield an occupation of the d-orbital of 8.8 electrons for Co/Au(111) [61]. The large occupation compared to a free cobalt atom which has 7 electrons in its d-orbitals is rationalized by $sp-d$ hybridization. n_d can vary between 0 (empty orbital) and 2 (double occupancy), where the Kondo regime is roughly $0.8 < n_d < 1.2$ [71] with approximately one unpaired electron in the d-level.
We assume, that the occupation of the d-level for cobalt adatoms on the various noble metal surfaces discussed here can be estimated by a simple model which considers the hybridization between the d-orbitals of the impurity with the neighbouring substrate atoms. The occupation is assumed to increase with increasing overlap due to $sp-d$ hybridization [72, 73]. The hybridization of the d-orbital with the states of the substrate is described by a tight-binding-like hopping term [74]

$$\beta = n_{\mathrm{NN}} e^{-\frac{a}{\lambda_d}} \tag{6.9}$$

with a prefactor n_{NN} which takes the number of nearest neighbour substrate atoms into account. a denotes the distance between the center of the adatom and of the next substrate atom which we calculate within a hard sphere model. The values used in the calculation are tabulated in table 6.1. The spatial extent of the d-orbital of the adsorbate enters through λ_d which is estimated to be 1Å. The adatom resides in the hollow site on both types of surfaces discussed here, yielding $n_{\mathrm{NN}} = 4$ for the 100-surfaces and $n_{\mathrm{NN}} = 3$ for the 111-surfaces. To first order, the occupation n_d is described in terms of the hybridization by

$$n_d = n_{d0} + c \cdot \beta. \tag{6.10}$$

n_{d0} and c are obtained by fitting eq. 6.8 and 6.10 together with a proportionality constant to the experimentally obtained Kondo temperatures with the parameters as tabulated in table 6.1. The resulting curve $T_{\mathrm{K}}(n_d)$ is shown in fig. 6.5(a), where the hopping term 6.9 is already transformed into occupation n_d based on the fit and formula 6.10. It shows an excellent agreement with the experiments. As expected, the hybridization between the impurity and the conduction electrons and thus the occupation of the d-level varies in a narrow range around $n_d \approx 1$. The trend in the occupation of the d-level is confirmed by the position ϵ_{K} of the Kondo resonance. The relation between n_d and ϵ_{K} is plotted in Fig. 6.5(b) together with the theoretically expected

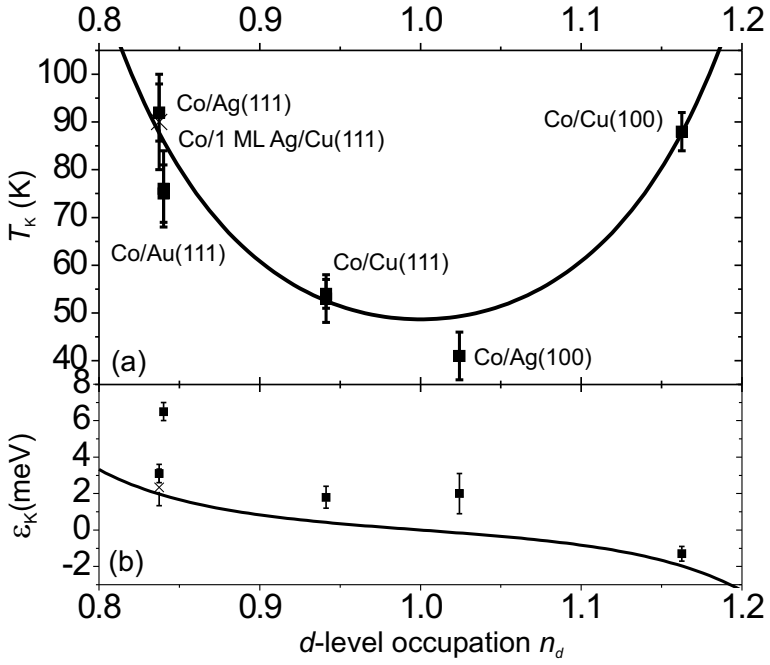

Figure 6.5: (a) Kondo temperature T_{K} in dependence of the occupation n_d of the d-level calculated with Eqs. 6.8-6.10. (b) Shift of the Kondo resonance ϵ_{K} with respect to the Fermi energy, the solid line shows the prediction by our model according to Eq. 6.11.

behaviour [58]

$$\epsilon_{\mathrm{K}} = \Gamma \tan\left(\frac{\pi}{2}(1 - n_d)\right). \tag{6.11}$$

The systems cobalt on Cu(111) and Ag(100) are almost perfectly described by the symmetric Anderson model, where $n_d = 1$ and the Kondo temperature as a function of the occupation has a minimum. Either by enhancing the hybridization, i.e. by changing the substrate to Cu(100), or by reducing it by going to Ag(111) or Au(111) the Kondo temperature is rising. The value, which we find for the occupation of the d-level for Co/Au(111), 0.84 is close to the calculated value 0.8 [61]. The physical picture that emerges is that for non-integer occupation the spin flip probability is higher and thus

the Kondo temperature increases.
The key result is that based on simple arguments one finds an increasing occupation of the impurity level expressed in the value of n_d when going from a Ag(111) substrate to Cu(100) which explains the observed values of T_K and ϵ_K using the mapping onto the Anderson model proposed in Ref. [61]. The limitations of the simple model are obvious. It neglects relaxation, which will lead to an enhanced hybridization between the d-level and the substrate. Furthermore, details of the electronic structure of the substrates are ignored. For Co/Au(111) the Kondo temperature is slightly lower than predicted by our model. This fact reflects that the model does not take into account hybridization with specific substrate orbitals. While the $4d$-orbitals of silver are very localized and well beyond the fermi energy, the $5d$-orbitals of Au are close to the fermi level and will contribute to the hybridization with the impurity. Thus the overlap is most likely underestimated for gold and overestimated for silver. Finally, the model neglects that an enhanced hybridization will lead to a reduction of the Coulomb repulsion U and an increase of the width of the d-level Δ. T_K increases monotonically as a function of both - smaller U and larger Δ, hence the curve shown in fig. 6.5(a) will become asymmetric and its minimum will be shifted to lower occupations but qualitatively show the same trend. This explains the systematic deviation of the shift ϵ_K in fig. 6.5(b) from the calculated curve.
We note that the surface state does not play a major role. Although its onset on Ag(111) is 165meV closer to E_F than on Ag/Cu(111) [75], the Kondo temperature of a cobalt adatom is the same. This is consistent with our model, where the properties of the surface state do not enter and with earlier experimental [30, 68] and theoretical results [76] which both show that the surface state has only a minor influence on the properties of Kondo systems.
Interaction with the tip is negligible as well within our model, the height of the tip above the surface is typically ~ 10Å and thus it will not hybridize with the d-level of the adatom. This is in accordance with the measurements by Madhavan *et al.* [62] who investigated the Kondo resonance in dependence of the tip-sample distance.
The behaviour of the Kondo temperature as shown in fig. 6.5(a) is similar to what has been measured on quantum dots. There, the properties of the Kondo system are tuned by varying a gate voltage, which shifts the electronic states up or down and thus decreases or increases the fractional occupation of the quantum dot [8]. In the case of adatom/surface systems, this tuning can be achieved by modifying the substrate.

In conclusion, we have presented a simple model in order to understand the large range of Kondo temperatures of cobalt adatoms on noble metals surfaces which have been reported previously and in this work. The model estimates the hybridization between the adatom's d-level and the substrate. Despite the simplicity of this model, which is in contrast to the complexity of the many-body physics, which is necessary to describe the Kondo effect, it captures the essence of the impurity/substrate Kondo systems presented here. Motivated by experiments on Ag/Cu(111), only the local environment of the impurity enters our model. The Kondo temperatures for adatoms on multilayer systems are shown to depend only on the topmost layer. This conclusion is not trivial, since the extent of the Kondo cloud - the size of the many-body state which leads to the formation of the Kondo resonance - is believed to be on the order of several ten to hundred nanometers [77]. Due to the local character of the magnetic interaction, it will be interesting to investigate the behaviour of a Kondo impurity on a surface alloy as substrate, which should allow for a fine tuning of the Kondo temperature as a function of the local stoichiometry in the vicinity of the adatom.

6.3.5 Substitutional cobalt impurities on Cu(100)

Cobalt impurities which are incorporated in the first layer of the subtrate have been prepared by depositing the cobalt from an electron-beam heated cobalt rod at a temperature of ~ 320K with coverages around 0.001ML. At this temperature, exchange processes between cobalt adatoms and copper atoms in the first monolayer are activated [78].

After transfer to the STM, single cobalt impurities at substitutional sites of the copper substrate can be found (see Fig. 6.6(a)). They are imaged with an apparent height of only ~ 4pm and a full width at half maximum of ~ 5Å (see Fig. 6.6(b)).

To check the chemical nature of the impurities, we have performed a CO titration experiment in a similar way as described in Ref. [78]. After deposition of cobalt as described above, we have dosed ≈ 0.5L CO at a sample temperature of 190K and subsequently annealed the sample to 260K. Above a temperature of ≈ 200K, CO desorbs from the Cu(100) surface [79] while CO molecules attached to cobalt impurities remain on the surface and can thus be used as markers. Fig. 6.6(c) shows three such complexes consisting of a substitutional cobalt impurity with CO molecules adsorbed. The com-

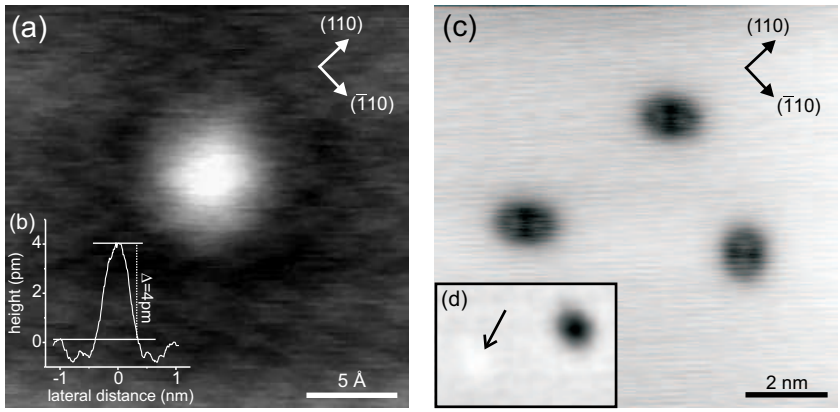

Figure 6.6: (a) Single cobalt impurity in the 1st monolayer of the Cu(100) substrate. Image taken at $U = 80\text{mV}$, $I = 1\text{nA}$. (b) Line cut through the impurity in (a). (c) Topography of three embedded cobalt atoms with two CO molecules attached to each of them to mark them ($U = -0.3\text{V}$, $I = 1.8\text{nA}$). (d) After removal of the CO molecules, only the cobalt atom remains at the position of the complex (left, marked by an arrow), typically one CO molecule is found on the surface in the vicinity of the cobalt impurity (imaged as a depression).

plexes have a two-fold symmetry which suggests a stoichiometry of 1:2. The $\text{Co}_{\text{sub}}(\text{CO})_2$-complexes (the index "sub" stands for substitutional) occur in two orientations on the surface which is due to the four-fold symmetry of the Cu(100)-substrate. The CO molecules point towards the nearest hollow sites. By injecting electrons with a bias voltage of around 5V into the complex, it can be dissociated leaving the cobalt impurity at the place of the complex. Typically, one of the CO molecules desorbs from the surface, while the other one can be found next to the impurity as shown in fig. 6.6(d). Spectroscopy on single cobalt impurities - prepared either with or without prior CO adsorption - shows a narrow resonance at the Fermi level (see Fig. 6.7(a)). The narrow resonance can be fitted by a Fano function (eq. 6.6) plus a linear background term. We obtain the line shape parameter to be $q = 4.4 \pm 0.8$ – describing an asymmetric peak. It has a width of $\Gamma = 7.1 \pm 0.6\text{meV}$ which corresponds to a Kondo temperature T_{K} of $82 \pm 6\text{K}$. Table 6.2 compares the measurement on a substitutional cobalt impurity with the results for adatoms on the Cu(100) and (111)-surfaces and for bulk impurities.

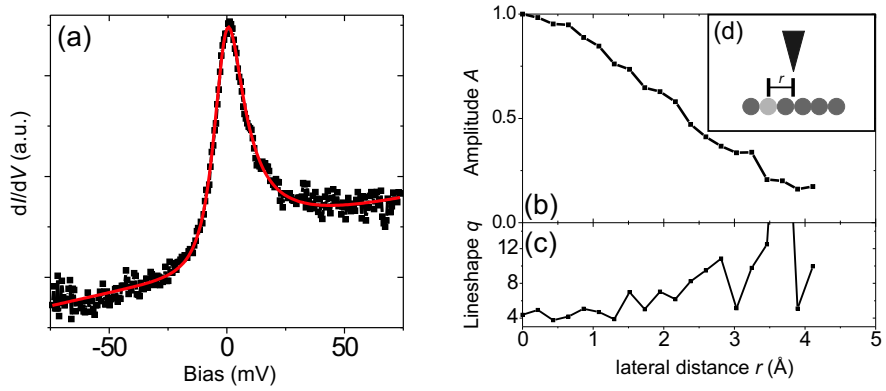

Figure 6.7: (a) Spectroscopy on a single cobalt impurity. The narrow Kondo resonance at the Fermi energy is fitted by of a Fano function with a linear background (formula 6.6). (b) Dependency of the amplitude A and (c) the line shape parameter q of the resonance on the lateral distance r from the impurity. (d) Sketch of the measurement geometry.

The observed line shape is close to a peak, which is in contrast to the spectra measured on adatoms, where values of q between 0 and 1 have been reported [3, 9, 66, 62, 68, 30]. The physical picture, which has been discussed in the past, assumes that the line shape is governed by the contribution of a direct tunneling channel into the d-orbital to the total tunneling current. In this model, a lineshape of $q \sim 0$ corresponds to a negligible contribution of the direct channel, while higher values of q imply that it contributes considerably [62]. Recently, a different model has been proposed by Merino et al. [64, 65], where the direct tunneling channel is neglected. In this model, the lineshape is merely governed by the detailed electronic structure of the substrate and the hybridization with the adsorbate level.
In order to gain understanding of the observed line shape, the dependence of the line shape parameter q and the amplitude $A = a(q^2+1)$ of the resonance on the lateral distance r of the tip from the impurity has been investigated. In contrast to measurements on adatoms which are typically imaged with a height of $\approx$ 100pm, the height of the tip above the substrate stays essentially constant when moving the tip laterally since the height of the impurity of $\approx$ 5pm is negligible compared to typical tip-sample distances of around 10Å.

System	T_K[K]	q	ϵ_K [meV]	a [Å]
Co/Cu(111)	54 ± 3	0.18 ± 0.03	1.8 ± 0.6	2.36
Co/Cu(100)	88 ± 4	1.13 ± 0.06	-1.3 ± 0.4	2.36
Co in Cu(100)	82 ± 6	4.4 ± 0.8	-1.1 ± 0.1	2.56
Co in bulk Cu	≈ 500			2.56

Table 6.2: Kondo temperatures T_K (in K) and the Fano line shape parameter q and the position of the resonance ϵ_K. Values for Co/Cu(111) and Cu(100) and bulk Cu taken from Ref. [30].

Thus the substitutional impurities are ideal systems to measure the importance of a direct tunneling channel. Spectra have been recorded with the tip positioned in a distance r from the impurity and fitted by formula 6.6. The result is shown in fig. 6.7(b) and (c) together with a sketch (d) of the measurement geometry. The amplitude $A(r)$ of the feature decays within $r \sim 3$Å which is comparable to the apparent size of the impurity as measured in the topography. At the same time, the line shape first stays constant and then starts to oscillate. The large variations in $q(r)$ at distances above 2AA is due to the fact that the peak gets weaker and so the lineshape is less well defined. But still all the values of q observed are larger than 3.5 and thus correspond to a peak. This indicates, that tunneling into the d-orbital of the impurity which forms the Kondo state does not contribute to the tunneling current. A direct tunneling channel into the d-orbital, which interferes with the tunneling channel into the conduction band of the substrate, would lead to a strong dependence of the tunneling probability into the d-orbital on the lateral distance of the tip from the impurity [63, 30]. Thereby, the line shape would change, as observed for cobalt adatoms on the Cu(100) surface [30].

The observed Kondo temperature of 82 ± 6K is surprisingly low. The higher number of nearest neighbour compared to a cobalt adatom on both Cu(111) and (100) and thus the higher hybridization with the substrate would suggest that the Kondo temperature of a substitutional impurity is higher than that of an adatom. As shown in table 6.2, this is not the case. The behaviour can not be understood by only considering the number of nearest neighbours. One possible reason can be found in the adsorption geometry. As shown by DFT calculations [80], adatoms are relaxed towards the surface by roughly 16%, whereas substitutional impurities relax only about 7%. The observed

Kondo temperatures T_K can be rationalized: An adatom moves closer to its nearest neighbours thereby enhancing the hybridization. A substitutional impurity will remain roughly in the same position as the atom it replaces - and thus the hybridization with each neighbouring atom is weaker and counterbalances the increased coordination.
Recently, a paper has appeared where the authors claim to have measured the Kondo effect of cobalt atoms embedded in Cu(111) [81]. The substitutional impurities are imaged as depressions. The half width of the dip-like feature which they find in spectra acquired on the substitutional impurities is about 35meV. However, from the topography (Fig. 2(a) in their paper), their impurities resemble that of a CO molecule on Cu(111) [82] which is also imaged as a depression (as on Cu(100)). Also the tunneling spectrum which they show (Fig. 4 in their paper) does not have sufficient resolution to resolve features on the order of 10meV, which is the typical energy scale for the Kondo effect for all other adatom systems. Thus it cannot be excluded by their data, that the feature they observe is not simply the IETS feature of a CO molecule on Cu(111), which has step-like features at ±35meV [82] and can be mistaken for a Fano dip with $q = 0$. In that case, additional vibrational features at ±4meV would become visible in spectra recorded with a higher resolution. Since CO is one of the most important contanimations in UHV systems, it is important to be aware of and to discuss effects of CO.

Chapter 7

Spin tuning by ligand adsorption

The development of new atomic sized magnetic information devices requires a detailed understanding of magnetism at the nanoscale. The coupling of a single spin to a bath of conduction electrons is one of the quantities involved. The ability to tune this coupling is thus of fundamental interest to push miniaturisation to its ultimate limit. In this chapter, I show how the Kondo effect of a magnetic impurity can be exploited to study its magnetic properties. The modification induced by ligand adsorption is characterized and it is discussed what we can learn from the properties of a Kondo system about the magnetic interactions involved and how it can be exploited to spatially localize a spin center within a single molecule. The spatial mapping of the Kondo resonance is introduced as a new imaging mode of STM to atomically resolve the spin center of a molecule.

7.1 Spectroscopy on carbonyl complexes

7.1.1 Cobalt carbonyls

Tunneling spectra acquired in the center of the molecules show a pronounced feature near the Fermi energy in all cases. The spectra are displayed in Fig. 7.1A-D. From the fit of a Fano function (eq. 6.6) we can extract Kondo temperatures as listed in table 7.1. The Kondo temperature is found to

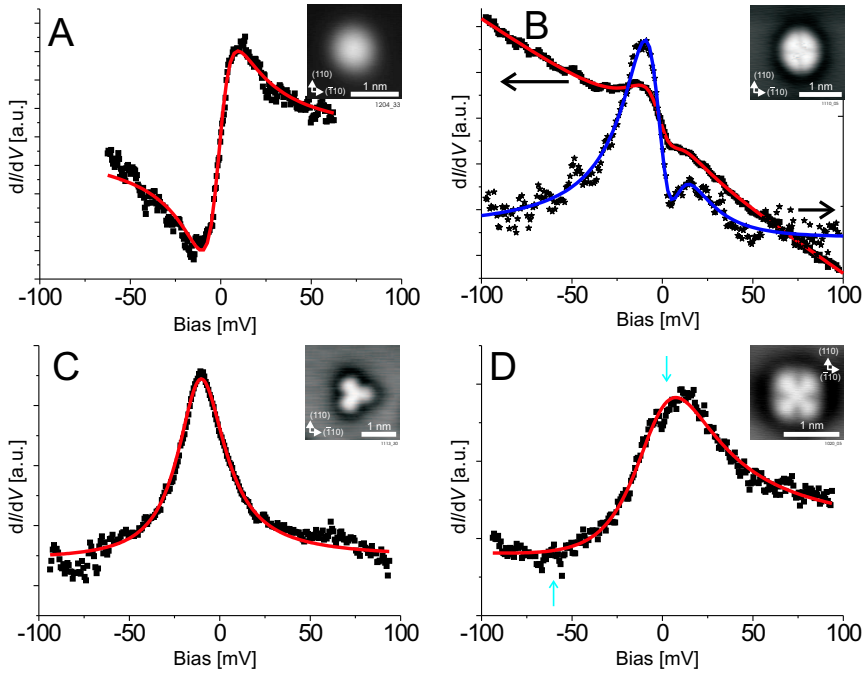

Figure 7.1: Spectra taken in the center of the adatom and carbonyls with $0, 2, 3$ and 4 ligands: (A) In the center of a cobalt adatom, (B) a $Co(CO)_2$ molecule (additionally, the spectrum is shown with a linear background removed), (C) $Co(CO)_3$ and (D) $Co(CO)_4$. A resonance is found at the Fermi level, solid lines show fits of a Fano function, for $Co(CO)_2$, two Fano functions have been fitted to account for the dip at the Fermi level.

increase with the number of ligands attached to the impurity from 88K for the cobalt adatom to 280K for the $Co(CO)_4$ complex.

7.1.2 Iron carbonyls

We have performed similar measurements for $Fe(CO)_4$-complexes. Again, a distinct feature is found near the Fermi energy. The Kondo temperature is 140 ± 23K. It is increased by more than a factor of two compared to that of an iron adatom. The STM image is shown in fig. 7.2(A+B) and the spectrum recorded on the carbonyl in fig. 7.2(C).

Molecule	T_K [K]	ϵ_K [meV]
Cobalt	88 ± 4	-1.3 ± 0.4
$Co(CO)_2$	165 ± 21	-1.8 ± 4.2
$Co(CO)_3$	170 ± 16	-13.2 ± 1.5
$Co(CO)_4$	283 ± 36	-5 ± 10

Table 7.1: Parameters determined from the fit of a Fano function for the various species.

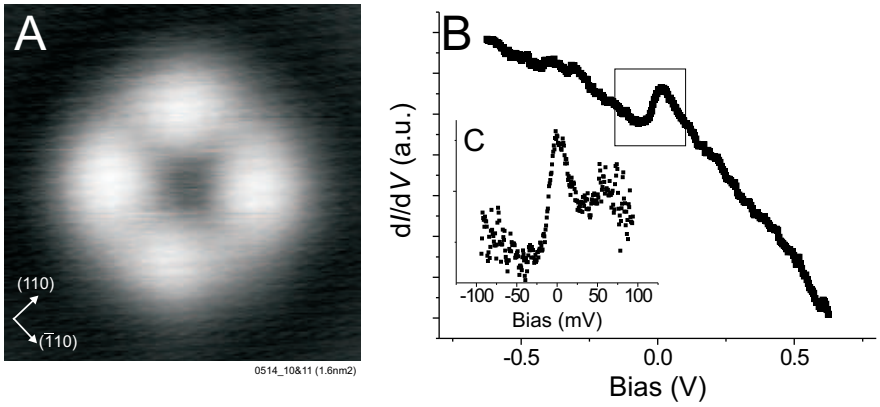

Figure 7.2: (A) Topography of $Fe(CO)_4$ molecules on Cu(100). $U = -1$V, $I = 1.6$nA, image size is 1.6×1.6nm^2. (B) Spectrum taken in the center of an $Fe(CO)_4$ molecule, (C) showing the region near the Fermi energy.

7.1.3 Discussion

In table 7.1, we summarize the results for the various molecules and a cobalt adatom. For a single cobalt adatom, the feature near the Fermi level has already been discussed in chapt. 6: it is the Kondo resonance due to the interaction of the spin of the adatom with the conduction electrons of the host [30]. By adding carbon monoxide molecules, the magnetic properties are modified. Carbon monoxide being a strong-field ligand is expected to increase the splitting between the molecular orbitals, so that pairing of the electrons is facilitated and the molecule is in a low-spin state. The free molecule has an uneven number of valence electrons with one unpaired electron. It is a radical, which shows in an inert gas matrix an ESR-signal [83]. Provided that the spin of the molecule survives on the surface, the narrow feature at the Fermi energy can be rationalized as the Kondo resonance due to the interaction of the spin with the conduction electrons of the substrate. The unpaired electron is expected to be in the d-orbital of the cobalt adatom in agreement with the spatial mapping of the resonance by STS, which indeed reveals the localization of the feature in the center of the molecule. The mapping will be discussed in detail in section 7.2. We observe similar features at the Fermi energy for $Fe(CO)_4$ on Cu(100) and previously Lee and Ho [84] reported peaks at the Fermi energy on iron mono- and dicarbonyls on Ag(110). For comparison, we have performed experiments on $Cu(CO)_2$ molecules on Cu(100) which do not show a similar feature at the Fermi energy, only the known vibrational features are observed [84]. The fact, that the feature stays pinned to the Fermi level within only a few millivolts by changing the central atom to iron or by changing the number of ligands indicates that it is not simply an electronic feature in the LDOS of the molecule.
It can be excluded that the feature is due to vibrational features that lead to spectra which are symmetric with respect to the Fermi level as discussed in section 3.4.2. Vibrational features could thus be mistaken for a Kondo feature especially for a Kondo dip if $q \sim 0$. But in our case the spectrum is not symmetric with respect to the Fermi energy. Apart from the symmetry of the spectrum, it can be shown from simple arguments, that the trends would be reversed for vibrational features: with increasing number of ligands, the metal-carbon bond will become weaker and thus the M-C vibrations will be reduced in energy leading to a narrower feature in contrast to our observation of a feature getting wider with increased number of ligands. Similar arguments apply for the metal-substrate bond. For the CO stretch mode,

the trend is reversed: as the M-C bond is weakend, the C-O bond becomes stronger and its modes are shifted to higher frequencies. But the lowest C-O stretch mode is at 250meV [84, 85], so it cannot account for the features within ±100meV of the Fermi energy.
The behavior of the Kondo temperature as a function of the number of ligands can be understood in the Kondo model. The CO ligands will lead to an increase in the exchange coupling J between the adatoms spin and the conduction electrons by a delocalization of the d-orbital. The physical idea for the increase of the exchange coupling J with the number of ligands emerges from the Schrieffer-Wolff transformation

$$J = \frac{\Delta}{\pi\rho_0}\left(\frac{1}{\epsilon_d + U} - \frac{1}{\epsilon_d}\right). \tag{7.1}$$

It is assumed, that Δ and ϵ_d stay basically constant while U will be reduced by the adsorption of the ligands. Δ will rather be reduced by an increasing number of ligands leading to a decrease in the coupling. The bond between the CO molecules and the cobalt adatom is commonly described by the Blyholder model [86]. It consists of a donation of electrons from the σ-orbital of the CO to the transition metal adatom and a backdonation from the d-orbitals of the cobalt adatom to the $2\pi^*$ orbital of the CO molecules. This backdonation leads to a delocalization of the d-electrons and therefore reduces the Coulomb repulsion U. The decreased Coulomb repulsion leads to an increased exchange coupling J as can be seen from eq. 7.1. With in a simple model, we assume that J scales linearly (apart from an additive constant J_0) with the number of ligands n

$$J = J_0 + c_J \cdot n. \tag{7.2}$$

We introduce this approximation into the Kondo temperature as obtained from the Kondo model

$$k_\mathrm{B}T_\mathrm{K} \sim De^{-\frac{1}{J\rho_0(E_\mathrm{F})}}, \tag{7.3}$$

and treat D, J_0 and c_J as fitting parameters. Fig. 7.3 shows a fit of this model to the experimental data. Within the errors, a good agreement is found. The relative increase in the Kondo temperature is similar for iron. While an iron adatom has a Kondo temperature smaller than 60K, on a $Fe(CO)_4$ molecule we find a T_K of about 140 ± 23K.

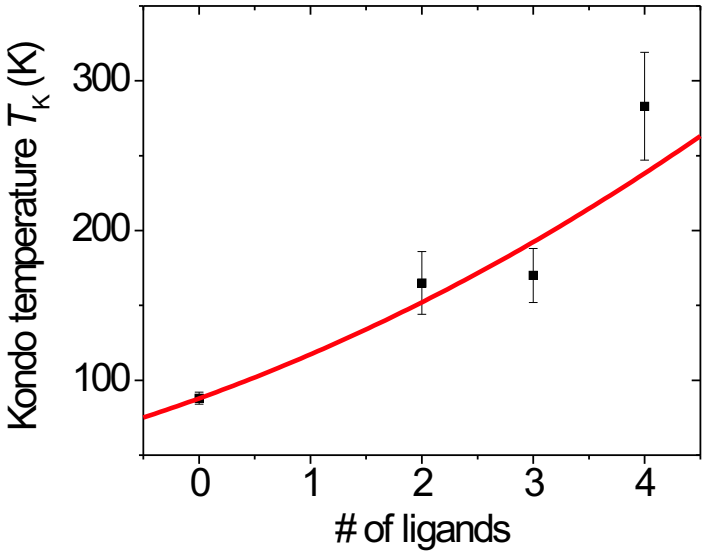

Figure 7.3: Scaling behaviour of a cobalt impurity with N CO molecules attached to it. The curve shows a fit of eq. 7.3 to the data.

7.2 Spin Mapping

The STM is able to go a step beyond the spectroscopic characterization of the Kondo resonance by exploiting its spatial resolution. In Fig. 7.4 we show the spatial mapping of the amplitude of the resonance for a cobalt tetracarbonyl molecule. The difference between the $\mathrm{d}I/\mathrm{d}V$-signal at the voltages marked by the arrows in fig. 7.1(D) is mapped spatially as intensity in fig. 7.4(B), while fig. 7.4(A) shows the simultaneously acquired topography. The spectroscopic image does not reflect the fourfold symmetry of the molecule showing only a spherically symmetric maximum in the center of the molecule - localized within a radius of $\approx$ 2.5Å. Thus we can not only detect the spin via the Kondo resonance but also localize it. The spin is found to originate from the cobalt atom which sits in the center of the molecule. The same experiment has also been performed on iron carbonyls, where the spin center is also found in the center of the molecule.

The spatial mapping of the Kondo resonance can be extended to more com-

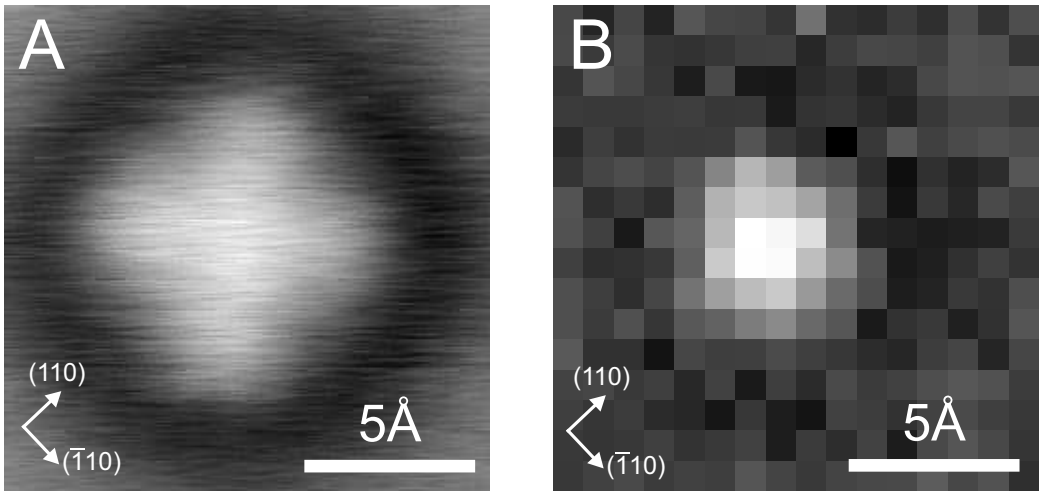

Figure 7.4: (A) Topography and (B) simultaneously acquired Kondo map of a cobalt tetracarbonyl molecule.

plicated species with more than one impurity. In fig. 7.5, the same measurement as for the $Co(CO)_4$-molecule is shown for $(Co(CO)_2)_2$ and $(Co(CO)_3)_2$ (both have been introduced in chapter 4). Fig. 7.5(A) and (D) show the topographies of the two species. On both, similar features at the Fermi energy can be found in the spectroscopy (see fig. 7.5(B) and (E)). A spatial mapping (fig. 7.5(C) and (F)) of these features allows for a localization of the cobalt atom and the spin on the complex.
Thus the Kondo effect can be exploited to make STM sensitive for the spin of a magnetic molecule. This allows to study by STM both the coupling between the spin of an adsorbate and the substrate and its spin center.

7.3 Conclusion

In conclusion, we have shown who the coupling a spin to the conduction band can be modified not only by changing the substrate, but also by chemistry by attaching ligands to the adatom. Thus, the magnetic properties of the cobalt adatom can be modified. CO begin a strong field ligands tends to quench the magnetism of the cobalt adatom which is expressed in the increasing Kondo temperature. By choosing a weak field ligand which enhances the magnetism of the adatom instead of quenching it, it might be possible to decouple a spin

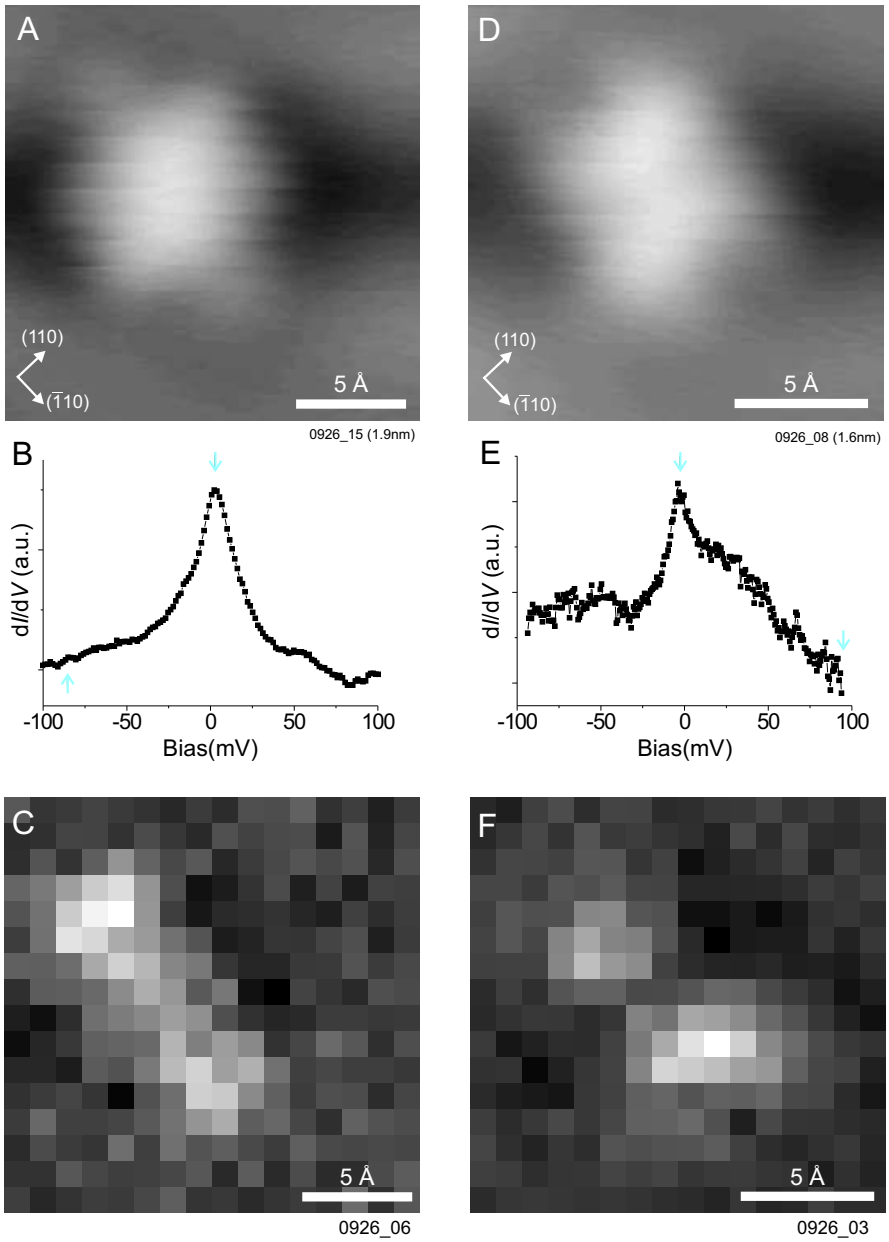

Figure 7.5: (A) and (D) topographies of binuclear carbonyl clusters ($(Co(CO)_3)_2$ and $(Co(CO)_2)_2$, the images are slightly distorted due to drift), (B) and (E) corresponding spectra taken on top of the binuclear carbonyl clusters, (C) and (F) spatial mapping of the peak in the spectra shown in (B) and (E).

from the conduction band in the very same way decreasing the Kondo temperature. Thus the parameters of the Anderson model can be tuned allowing to compare experiment and theory. The adsorption experiments demonstrate how the local chemistry in the vicinity of an adatom carrying a spin can be exploited to taylor magnetic interactions.
The spatial mapping of the spin center of the magnetic adsorbate opens up new possibilities to study single magnetic molecules with unprecedented resolution, if the spin center couples to the conduction band of the substrate. Furthermore if the coupling between adjacent molecules is on the same order as the coupling to the substrate, the interaction can be studies and eventually even tuned by manipulation – resulting in a new tool to prepare and investigate molecular magnetism. The study of magnetic interactions via the Kondo effect will be shown for the simplest case of single magnetic adatoms on a metallic substrate.

Chapter 8

The Kondo Effect of Coupled Spins

8.1 Introduction

Having shown how the Kondo physics of a single magnetic adatom can be studied and modified by STM, this chapter extends these results to coupled spins. The coupling is again studied and detected via the Kondo resonance. In the past, the group of Mike Crommie has dominated the research on the Kondo effect of coupled spin systems at a surface. In their work, nanostructures consisting of up to three magnetic adatoms have been created on Au(111) by atomic manipulation [87, 88, 89]. For cobalt adatoms, the Kondo resonance has been found to be quenched by the formation of a compact dimer [87]. Two nickel adatoms, which on their own do not show a Kondo resonance, reveal the formation of a Kondo feature as soon as the two atoms interact [89]. On a chromium trimer, a Kondo resonance has only been observed in a very special configuration (in the so-called isoceles), however again the single chromium adatom does not have a Kondo feature [88].
The coupling between two Kondo impurities has also been studied in coupled quantum dots [90]. The advantage is here, that the parameters can be tuned simply by varying gate voltages. The experimental setup of two coupled quantum dots thus allows to tune directly the coupling strength between the two dots. The measurements show a splitting of the Kondo resonance as soon as the coupling is of the same order of magnitude as the Kondo temperature. The intuitive picture is that the Kondo resonance splits into a bonding and

an antibonding state. It should be noted that it will be experimentally very challenging to extend these results to more coupled quantum dots, since the preparation of quantum dots with equivalent properties is not trivial.
While the lateral manipulation of single atoms with the STM tip is a standard task on the noble metal (111) surfaces [91], it is quite a challenge on a (100) surface. This is mainly because the (100) surfaces are more open and thus they bind adsorbates stronger than the (111) surfaces. One indication of this are the different diffusion barriers: on Cu(111), adatoms start to hop around already at $\sim$ 15K [92], while on Cu(100) cobalt adatoms do not move below 100K. We have chosen to study arrangements of cobalt atoms which are formed from the carbonyl complexes described in chapter 4. After a brief introduciton into the theory of the Kondo effect in coupled spin systems, the preparation of the atomic arrangements from the carbonyls will be discussed. The dependence of the Kondo effect on the distance between the cobalt adatoms in a dimer will be discussed and results for a chain of three adatoms presented.

8.2 Theory

Basically, the coupling between two impurities introduces another energy scale into the problem. Depending on the strength of the coupling, a variety of new effects are expected. For the following discussion, the coupling between the two magnetic impurities will be called I (as opposed to the coupling J between one of the spins and the spins of the conduction electrons of the substrate) irrespective of its origin. So I will generally contain contributions from conduction electron mediated interaction (RKKY-interaction), direct exchange and eventually also superexchange. Magnetic dipole coupling is orders of magnitudes too small to be of any importance. The relevant energy scale of the Kondo problem is the Kondo scale $k_{\mathrm{B}}T_{\mathrm{K}}$.
The relative magnitude of the two $k_{\mathrm{B}}T_{\mathrm{K}}$ and I determines the behaviour of the coupled system. For large ferromagnetic coupling $I \gg k_{\mathrm{B}}T_{\mathrm{K}}$, the two spins will become locked in the same direction when the temperature T becomes smaller than the Curie temperature of the mini-domain ($k_{\mathrm{B}}T \sim I$). The two spins add up to one large spin. As the temperature is further lowered below a new Kondo temperature $k_{\mathrm{B}}T_{\mathrm{FMK}}$, the combined spin will form a Kondo system.
For $|I| \ll k_{\mathrm{B}}T_{\mathrm{K}}$, the Kondo effect of the single impurities dominates, so they

behave as independent Kondo impurities. Finally, for antiferromagnetic coupling $|I| \gg k_B T_K$, the two spins will again be locked into a single mini-domain [93], this time with no net resulting spin. The interesting regime is intermediate antiferromagnetic coupling $|I| \sim k_B T_K$. It is predicted, that in this regime the splitting of the Kondo resonance can be observed [94, 95] as has been found in quantum dots [90]. Increasing the number of coupled impurities in a linear chain, it has been predicted, that for an uneven number of impurities, a gap forms at the Fermi energy in addition to the Kondo peak [95]. A similar gap emerges from a theoretical treatment of an inifinite 1D chain of magnetic impurities [96]. This prediction is yet to be confirmed experimentally.
However it should be noted that this discussion assumes, that the coupling J to the conduction band is not modified by the coupling between the impurities. This is not necessarily a valid approximation on the surface, where the formation of a dimer molecule may substantially reduce the coupling to the substrate [87].

8.3 Preparation and Characterization

The simplest way to prepare small clusters of cobalt atoms would be to simply deposit small amounts of cobalt on the surface and then let the clusters arrange by diffusion of the cobalt adatom. However, this leads to the formation of compact clusters with a geometry which is difficult to determine.

We have prepared our clusters and nanostructures by growing cobalt carbonyl molecules as described in chapter 4. The carbonyl groups inhibit nucleation in islands and promote the formation of small clusters with distances between the cobalt atoms corresponding to next-nearest neighbour distances, but also complexes with larger separation between the cobalt atoms are found. The molecules are dissociated by controlled, tip-induced dissociation. The cobalt carbonyl complexes consisting of one and more cobalt atom and CO can thus be converted into nanostructures consisting only of cobalt adatoms. The resulting structures are shown in fig. 8.1. After the dissociation, a single cobalt adatom, a structure consisting of two cobalt atoms sitting on next nearest neighbour sites a distance of 5.12Å apart and a linear trimer consisting of three cobalt atoms which are separated by the same distance are found on the surface. The interatomic distances have been determined by fitting gaussians to the section through the monomer, the dimer and the

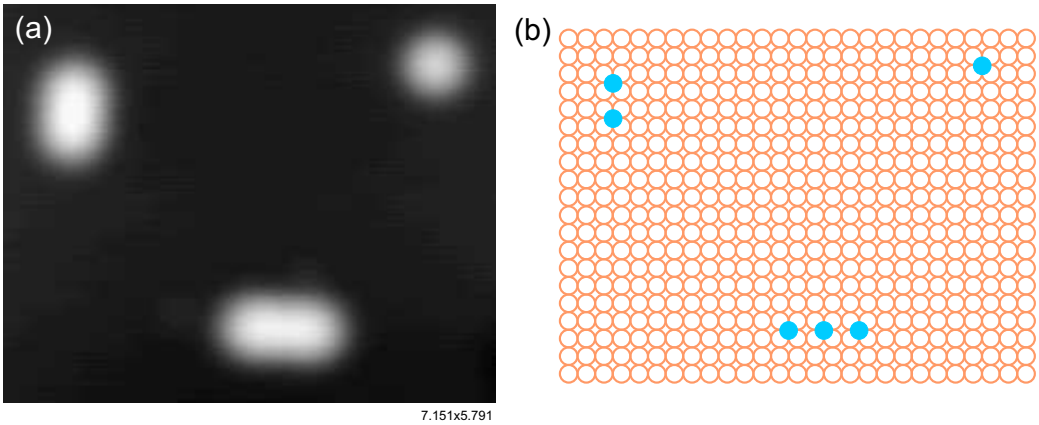

Figure 8.1: (a) Topography showing a cobalt monomer, dimer and trimer, (b) model of the arrangements of atoms in (a), shown to the same scale.

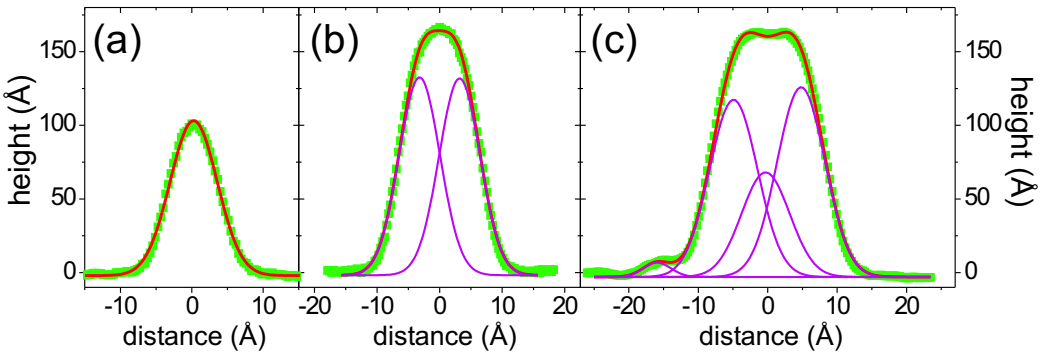

Figure 8.2: (a) Section of the monomer in fig. 8.1. The width obtained from the fit has been used to determine the spacing of the atoms in the dimer (b) and the trimer (c).

trimer as shown in fig. 8.2. The width of the gaussians has been fixed to the one determined for the monomer. As can be seen in fig 8.2, the fits describe the data well.

8.4 Results

The main interest is to study the magnetic interactions between the adatoms in the clusters. Fig. 8.3(a) shows different dimer configurations with different distances between the neighbouring cobalt atoms ranging between 2.56Å and 5.72Å. The STS spectrum shown in fig. 8.3(f) reveals that for a compact dimer the interaction between the spins is much stronger than the coupling to the substrate supressing the Kondo effect (at 6K). Already for the next-to-nearest neighbor distance a resonance is found again at the Fermi energy (fig. 8.3(g)). The resonance is considerably broader than that of the cobalt adatom. The width of the feature corresponds to a Kondo temperature $T_{\mathrm{K}} \sim 181 \pm 13\mathrm{K}$. Hence, the magnetic interaction between the two atoms in the dimer is no longer negligible. From the spectrum it can not be decided, whether the broadening is due to a splitting of the Kondo resonance as observed in coupled quantum dots [90] or whether the Kondo temperature is increased. For a distance of 5.72Å (fig. 8.3(h)) the Kondo resonance has almost acquired the same width and line shape as that of a single cobalt adatom. As a consistency check, spectra taken on both ends of the dimers are shown to be equivalent. For comparison, the spectrum acquired on a single cobalt adatom is shown (fig. 8.3(h)). It corresponds to infinite distance and no interaction.
For the trimer, the situation becomes even more interesting. As can be seen from fig. 8.4(a), the spectra show not only one peak, but a superposition of two features. In addition there is now a spatial dependence in the spectra since the sites of the cobalt atoms are no more equivalent. The intensity of the feature is stronger in the center of the trimer than on the two outer atoms. In fig. 8.4(c), the spatial dependence of the amplitude of the peak has been mapped. A fit of the two features by a superposition of two Fano functions results in a width corresponding to $\sim 78 \pm 13\mathrm{K}$ for the narrow dip and $368 \pm 37\mathrm{K}$ for the broad peak.

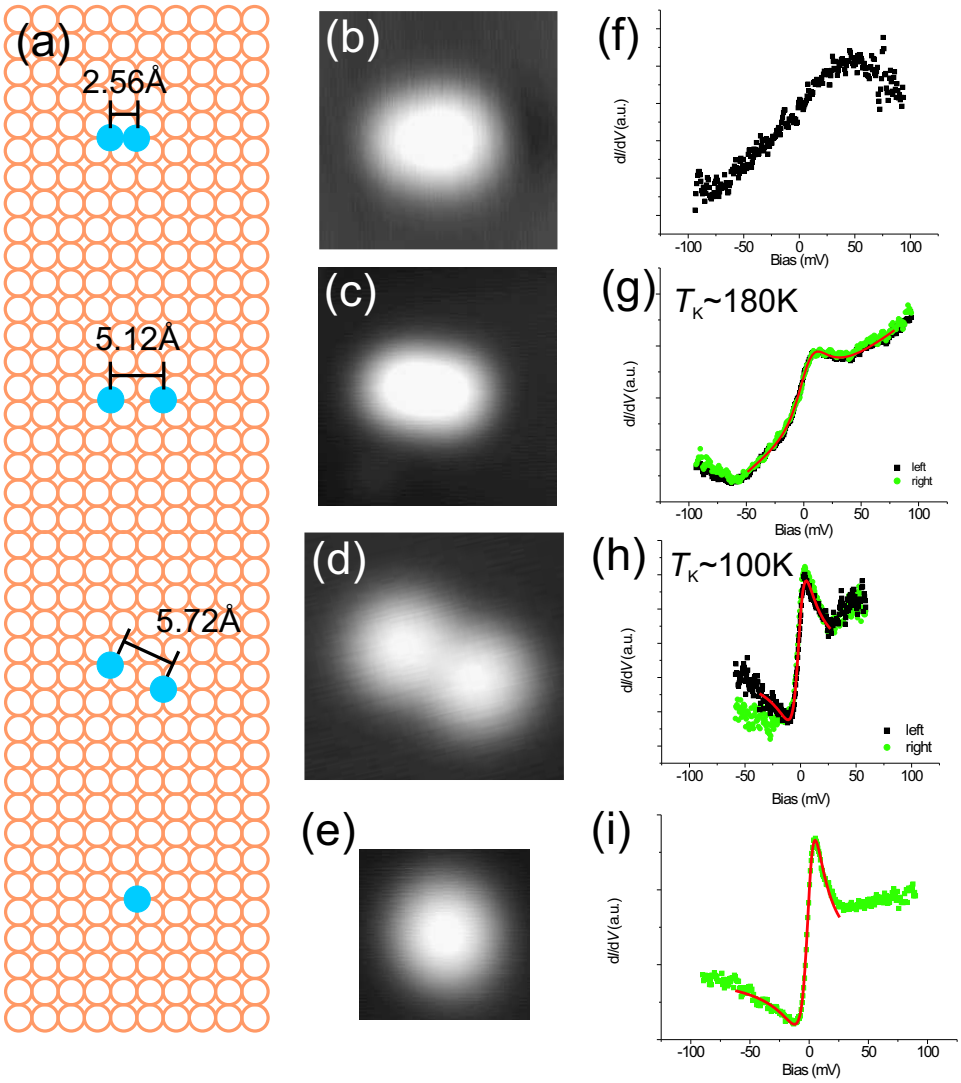

Figure 8.3: (a) Model of the dimers investigated, (b-e) topographies of the dimers, (f-i) spectra acquired on the dimers.

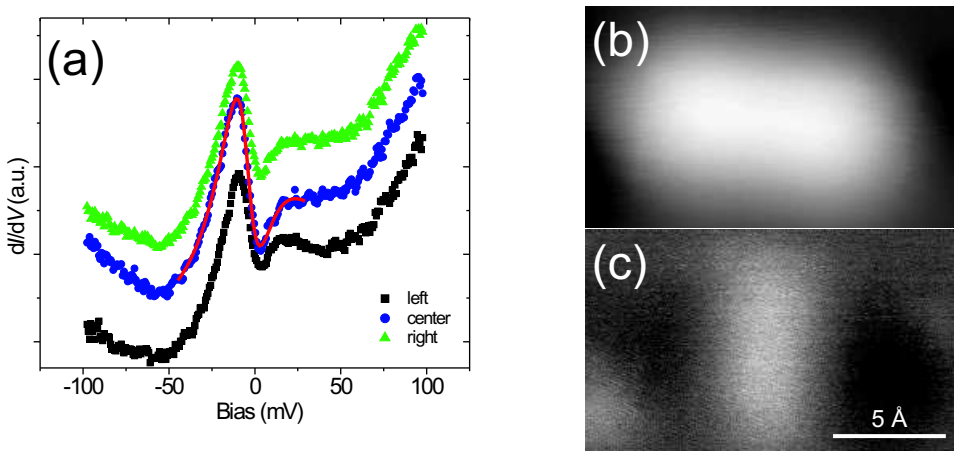

Figure 8.4: (a) Spectra acquired on a trimer, spectra taken on the left, right and center atom are shown and shifted vertically. (b) topography and (c) dI/dV-map acquired simultaneously on a trimer at -11mV. (c) shows the spatial map of the height of the peak near the Fermi energy.

8.5 Discussion

In table 8.1, the experimental results for the atomic arrangements which have been investigated are summarized. The observed behavior implies that there is some sort of interaction between the cobalt atoms. In the case of a compact cobalt dimer on Au(111) where the disappearance of the Kondo resonance has been observed upon dimer formation [87], the results have been explained by the formation of a Co_2 molecule. The strong interaction between the adatoms pulls them out of the surface towards each other. The reduction in hybridization with the substrate on its own would result in a strongly reduced Kondo temperature. In addition the cobalt atoms are expected to interact ferromagnetically leading to a further reduction of the Kondo temperature. In the case of the next-to-nearest neighbour sites, we do not expect the atoms to relax towards each other, so the interaction with the substrate should not be modified compared to a single cobalt adatom. Therefore, it is not surprising that we can find a resonance on the corresponding dimer with 5.12Å interatomic distance. For even larger distances, the width and lineshape of the resonance approaches that of the single impurity Kondo effect. The latter is in agreement with Chen *et al.* [87] who

	d [Å]	T_K [K]	ϵ_K [meV]	
Monomer	–	88 ± 4	-1.3 ± 0.4	
Dimer	2.56Å	–	–	
Dimer	5.12Å	181 ± 13	5.3 ± 1.6	
Dimer	5.72Å	99 ± 7	-1.4 ± 0.4	
Trimer	5.12Å	368 ± 37	-6.4 ± 5.2	
		78 ± 13	-2.8 ± 0.8	additional feature

Table 8.1: Summary of the Kondo temperatures determined on clusters. For the trimer, in addition to the main peak the data for the narrow feature at the Fermi energy is given.

find for cobalt adatoms on Au(111) that for separations larger than 6Å line shape and width of the resonance of a single cobalt adatom on Au(111) are recovered. Therefore the most interesting distance is 5.12Å, where magnetic interaction and Kondo effect are on the same energy scale.
The origin of the interaction can only be a magnetic one. There are three possibilities for magnetic interactions between impurities in metals: magnetic dipole coupling, direct exchange and RKKY interaction (and in principle superexchange, which does not apply in our case). Magnetic dipole coupling creates an energy scale on the order of 10^{-7}eV which is far beyond the Kondo scale of 10^{-3}eV. For direct exchange coupling, which is due to the overlap of the d-orbitals of the impurities, the situation is less obvious. The d-orbitals are quite localized, so their overlap should be negligible at a distance of 5Å. But still it might be on the same order of magnitude as the Kondo temperature. Finally, RKKY interactions, which are mediated by the conduction electrons, have to be considered. According to KKR calculations [97], the interaction between two cobalt atoms on Ag(100) on next-to-nearest neighbor sites is antiferromagnetic and the coupling strength is about 4meV. This coupling strength is expected to be similar or even stronger on Cu(100) where the interatomic distances are a bit smaller. The RKKY interaction is thus on the same scale as the Kondo temperature, so we believe that the modification of the Kondo effect is due to an antiferromagnetic coupling between the cobalt adatoms.
Two explanations for the behavior of the linear trimer emerge: The observation of an additional feature in the case of the cobalt trimer might be due to

the formation of a pseudospin. If the three atoms couple antiferromagnetic, there will remain a net spin. This pseudospin can be responsible for the occurence of a second energy scale besides the Kondo temperature of the single impurities. The other possible explanation is that the observed gap-like feature may be due to the formation of a gap in a linear chain with an uneven number of impurities as predicted recently for a chain of interacting quantum dots [95] or earlier in models describing an infinite chain of impurities [96]. In this picture, the Kondo peak on the dimer should split, which might be observable just as a broadening, while for the trimer a gap forms [95]. This assumption could be tested on longer chains consisting of 4 and 5 atoms.
In summary, it has been shown that the Kondo effect can not only be exploited to study single spins and their coupling to the conduction band of the substrate, but also to study the magnetic interaction between neighbouring magnetic adatoms. The distance dependence of the interactions has been adressed as well as new phenomena that occur in a small chain of three magnetic adatoms. In future experiments, the transition from the Kondo effect of a cluster with a small number of magnetic impurities to a 1D Kondo lattice will certainly yield a number of new and challenging experiments and results [96, 95].

Chapter 9

Kondo Lattices

It was the discovery of superconductivity in the heavy fermion compound $CeCu_2Si_2$ by F. Steglich *et al.* [98], which renewed the interest in Kondo lattices and coherent Kondo systems. Before, it was common lore that magnetism and superconductivity are mutually exclusive properties of a material. In heavy fermion superconductors, however, the spins of rare earth elements sitting on periodic lattice sites coexist with superconductivity. Nowadays, Kondo lattices and high-Tc superconductors are described by very similar theoretical models [58].
In this chapter, I will first discuss some of the basic theoretical considerations about the Kondo effect in rare earth compounds and Kondo lattices complementing the discussion of the theory of a single magnetic impurity in section 6.2.
I will then describe the preparation of the Kondo lattice we have studied, its characterization by SQUID magnetometry and the results of our STM study. This study has been performed in collaboration with the crystal growth group at the Max-Planck-Institut für Festkörperforschung in Stuttgart and with F. Treubel and G. Schatz at the University of Konstanz (SQUID magnetometry).

9.1 Theory

There are two substantial differences to the Kondo systems described in the previous sections: the magnetic atoms are rare earth elements, which due to the high degeneracy of their f-orbital exhibit a slightly different Kondo

behaviour. The second is the concentration of "impurities" which leads to coherence effects.

9.1.1 Anderson model for rare earth compounds

Due to the high degeneracy of the 4f-orbital of a rare earth atom, the corresponding Kondo peak is not any more pinned to the Fermi level, but it is shifted to higher or lower energies, depending on the filling of the 4f-orbitals. Typically, the shift is on the order of the Kondo temperature, comparable to the width of the Kondo peak. Thus, from a spectrum, two important quantities can be obtained, which are both related to the Kondo temperature T_{K}. The following results can be calculated from an expansion using the degeneracy N as a perturbation parameter (expansion in $1/N$) [58]. The Kondo peak of a 4f impurity can be approximated by a Lorentzian

$$\rho_{\mathrm{imp}}(\omega) = \frac{\tilde{\Delta}/\pi}{(\omega - \tilde{\epsilon}_{\mathrm{f}})^2 + \tilde{\Delta}^2}$$

centered at energy $\tilde{\epsilon}_{\mathrm{f}}$ with a width $\tilde{\Delta}$. The occupation n_{f} of the f-orbital can be obtained from its degeneracy N and the position and width of the quasiparticle peak by

$$\frac{n_{\mathrm{f}}}{1 - n_{\mathrm{f}}} = \frac{N\Delta}{\pi\tilde{\epsilon}_{\mathrm{f}}}, \tag{9.1}$$

where $\Delta = \tilde{\Delta}/(1 - n_{\mathrm{f}})$ describes the hybridization between the bare f-level and the conduction band. n_{f} can be determined experimentally from photoemission spectra (see e.g. [99]). In the case of Ytterbium, the occupation n_{f} describes the number of holes in the f-orbital. The position of the Kondo resonance yields the Kondo temperature, i.e. $\tilde{\epsilon}_f = k_{\mathrm{B}}T_{\mathrm{K}}$. An additional feature of the Kondo effect of 4f-compounds is the occurence of spin-orbit and crystal-field satellites which lead to additional peaks in the LDOS [100]. The spin-orbit splitting in rare earth compounds is on the order of 1eV due to the strong localization of the 4f-orbital, therefore the satellites are well separated from the main Kondo peak. The crystal-field splitting leads to side-peaks about $10 - 30$meV away from the Kondo peak.
Also macroscopic quantities can be related to the parameters of the Kondo peak. The magnetic susceptibility $\chi(0\mathrm{K})$ is connected to the position of the

Kondo peak by [101]

$$\chi(0) = \frac{1}{3}\frac{\mu_{\text{eff}}^2 n_f}{\tilde{\epsilon}_{\text{f}}}. \tag{9.2}$$

In $YbAl_3$, ytterbium is in an Yb^{13} configuration with a degeneracy $N = 8$ [58].

9.1.2 Kondo lattices

The new feature of a Kondo lattice is a second characteristic temperature scale T^*, which is connected to the onset of coherence. The otherwise localized Kondo clouds hop from site to site and create an electron band with a very high effective mass [102]. This is why these materials are often called heavy-fermion materials. Effective masses are about $10-100$ times the mass of a free electron. In the LDOS the onset of coherence can be observed as the formation of a substructure of the Kondo peak. This is shown schematically in fig. 9.1(a+b). Fig. 9.1(a) shows the band structure of a heavy fermion material. Two subbands are found with a gap in between. In fig. 9.1(b), the corresponding LDOS is depicted. It exhibits a gap surrounded by two strong peaks at the position of the Kondo peak one would have expected for the single impurity Kondo effect.

In case the gap is symmetric around the Fermi energy (so-called half filling), a Kondo insulator forms, which becomes insulating as soon as the gap is formed at low temperatures. An example for a Kondo insulator is FeSi, where the formation of the gap has been observed by tunneling spectroscopy [104].

9.2 Mixed-valence compound $YbAl_3$

The first measurements on $YbAl_3$ have already been reported in the seventies [105]. Besides a structural study of both $YbAl_2$ and $YbAl_3$, also the thermodynamic properties have been determined. Magnetization measurements on $YbAl_3$ revealed a clear deviation from a Curie law behavior. On reducing the temperature, the magnetization increases down to $\sim$ 130K, and then decreases again and rises again only below 20K. This behavior is clearly indicative of the Kondo effect. In addition, the authors found that the samples become superconducting below 0.96K which is surprising in view of the fact that the Kondo effect is related to the existence of magnetic moments while

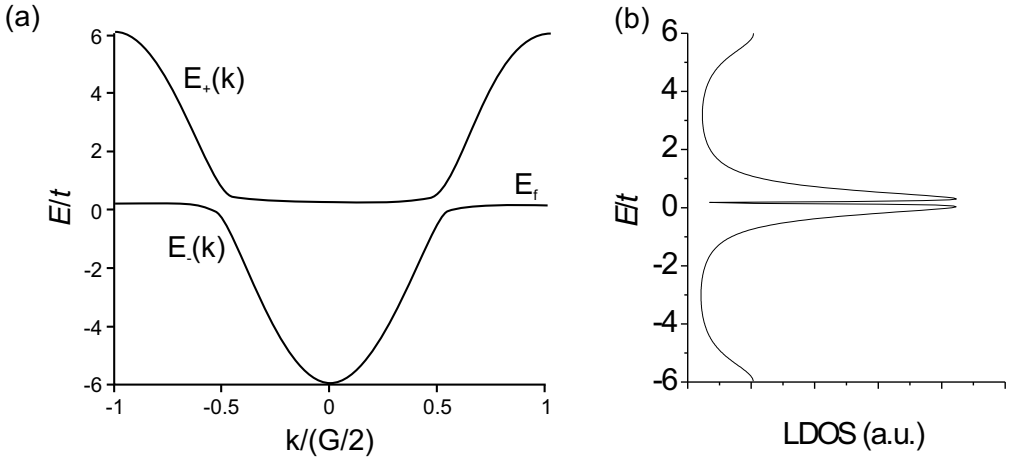

Figure 9.1: Heavy fermion bands: (a) band structure (taken from [103]) and (b) scheme of the corresponding LDOS.

superconductivity is generally thought to be quenched by magnetism.
In the late eighties, the first photoemission studies [106] were performed on $YbAl_3$ which were looking for the Kondo resonance. Rare earth compounds are Kondo systems which are particularly suited for photoemission studies of the Kondo resonance since the concentration of magnetic scatterers is orders of magnetitude higher than for single impurity systems as for transition metal impurities. The photoemission spectra exposed indeed a distinct feature slightly below the Fermi energy. Later on the interpretation of this feature has been questioned [107] and controversially discussed [108]. The main critique pointed out, that the temperature dependence of the Kondo peak as observed in the experiments would not show the behavior predicted by theory. The discussion was later also extended to other correlated materials [109, 110, 111].
Recently it has been shown that $YbAl_3$ exhibits two characteristic energy scales in its magnetic properties, which have been attributed to a crossover to a coherent Kondo state below 40K [112, 113, 114].

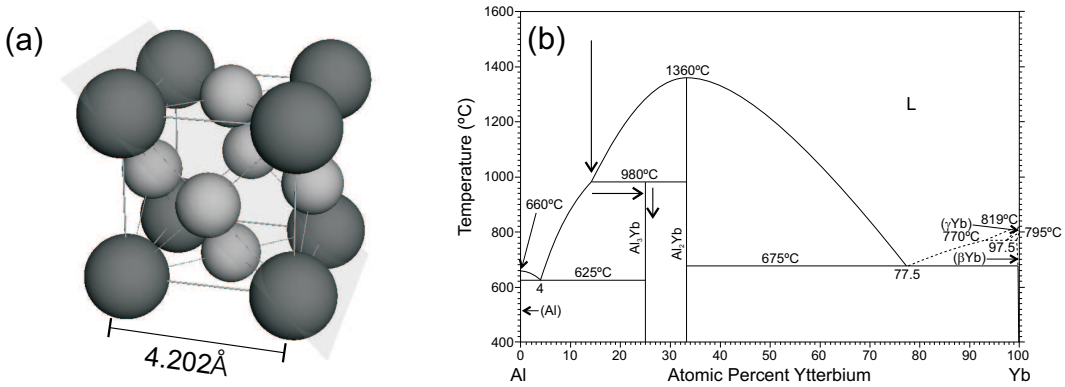

Figure 9.2: (a) Structure model of the unit cell of $YbAl_3$, the large balls indicate the positions of Yb, the small one those of Al atoms. The plane shows the (110) plane. (b) Phase diagram of YbAl [115], the arrows indicate the path which has been used to obtain the $YbAl_3$ crystal.

9.3 Structure

$YbAl_3$ forms an ordered alloy with a Cu_3Au structure [105]. The unit cell is that of an fcc crystal. The Yb-atoms are sitting in the corners of the cube, while the aluminum atoms reside on the faces. The structure is shown schematically in fig. 9.2(a). The nearest neighbour distance in the crystal is about 2.97Å.

9.4 Preparation

The $YbAl_3$ sample has been grown by the crystal growth group of the Max-Planck-Institut für Festkörperforschung using the Czochralski pulling method. The ingredients, ytterbium and aluminum have been treated with HF prior to the melting to remove surface oxides. The melt consisted of 12at. – % Ytterbium and 88at. – % Aluminum in an Al_2O_3 crucible. The annealing and growth process has been performed under Argon atmosphere. At a temperature of $\sim$ 980°C, a seed has been introduced from above into the melt and then slowly pulled out with a speed of $\sim$ 3cm/d while reducing the temperature, so that material nucleates at the seed and – in the best case – a single crystal of the desired compound is grown. In the case of $YbAl_3$ the growth is incongruent, that is only by reducing the temperature, the solid

phase can not be reached (see fig. 9.2(b)). Instead, the initial melt has the concentrations as indicated above with more Aluminum than needed to form $YbAl_3$. As can be seen from the phase diagram, at about 980°C, $YbAl_3$ is formed. The reaction path is indicated by the arrows in fig. 9.2(b). Due to the growth of the $YbAl_3$-crystal, the concentration of Aluminum increases. It is thus important to grow the crystal slow enough to avoid large variations in the concentration of the two compounds within the crucible.
From the crystal, we have cut slices of $\sim$ 2mm thickness and with a diameter of $\sim$ 5mm for the experiments. The grown samples were polycrystalline. Investigations by SEM showed that the size of the grains is about 500μm in diameter with regions of up to 20μm of undefined composition in between them. We have checked the composition of the grains by EDAX, the deviation from the stoichiometry 1:3 stayed below 3%.
For the STM measurements, the slice has been oriented by XRD predominantly in the (110) direction and polished with a suspension of diamond particles with a size of down to 0.25μm. After transfer to UHV, the surface has been treated by sputtering and annealing cycles. During the first cycles, the sample has been heated up to 700K, later on we annealed only to $600 - 650$K. Since the sample is polycrystalline, the grains have different orientations and the (110) direction will at best dominate. The STM measurements have been performed on two different slices of the crystal.

9.5 SQUID measurements

The theoretical expectation for the temperature dependence of the magnetic susceptibility χ is shown in fig. 9.3(a). Starting from high temperatures, where the spins fluctuate freely due to thermal excitation, the susceptibility rises with decreasing temperature. Around the Kondo temperature, the susceptibility has a maximum, the spins become more and more screened by the conduction electrons, so that their magnetic moment is suppressed with further reduction of the temperature. The exact position of the maximum of the magnetization depends on the degeneracy of the f-level, for $J = 7/2$ at about one fourth of the Kondo temperature.
The result of our SQUID measurements is shown in fig. 9.3(b). It is in good agreement with theory and identical with previously published magnetization measurements on $YbAl_3$ using SQUID magnetometry [116] and polarized neutron diffraction [117], indicating that our sample has the desired proper-

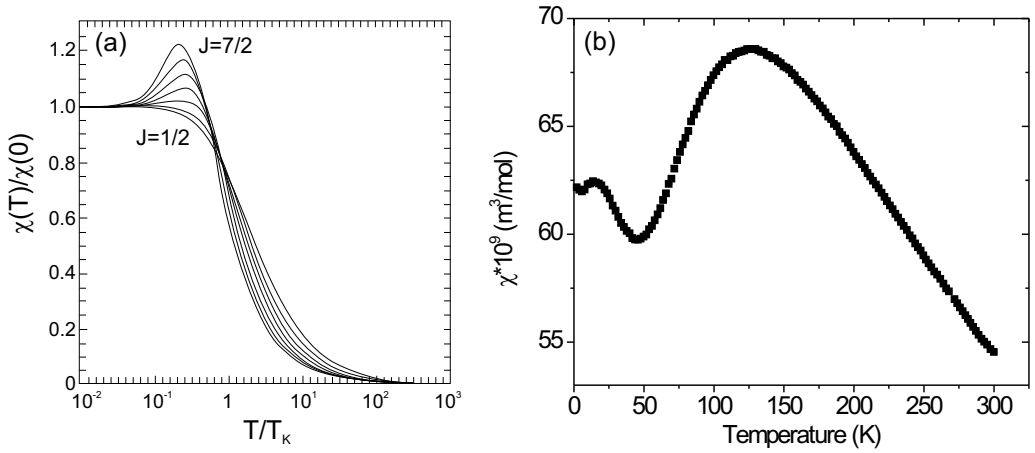

Figure 9.3: (a) Theoretical calculation for the temperature dependence of the magnetization (fig. 1 from Ref. [118], $J = \frac{7}{2}$ for Yb^{13}), (b) measured magnetization.

ties. In addition to the theoretical curve describe above, the experimental curve exhibits besides the maximum around 126K due to the growing spin compensation clouds around the magnetic ions a second maximum around 14K. This indicates that another crossover occurs. One possible explanation is the onset of coherence, so the Kondo "impurities" are not any more behaving as independent Kondo systems. From an extrapolation of the zero temperature susceptibility, the Kondo temperature can be extracted from eq. 9.2. We obtain with $\chi(0) = 6.2 \cdot 10^{-8} \frac{\mathrm{m}^3}{\mathrm{mol}}$

$$\frac{T_\mathrm{K}}{n_\mathrm{f}} \approx 522\mathrm{K}.$$

Using $n_\mathrm{f} = 0.7 \pm 0.1$ as determined from photoemission experiments [99, 108, 109], we obtain $T_\mathrm{K} \approx 365 \pm 52\mathrm{K}$.

9.6 STM measurements

9.6.1 Structure

The structure of the $YbAl_3$-surface is more complicated than that of the simple fcc crystals. Apart from the fact, that the alloy surface can have different terminations, different grains of the sample expose different crystallographic facets. Thereby it is possible to study the properties of different orientations on the same sample, selecting the facet with the STM. Fig. 9.4(a-d) show a (110)-facet, which can be either terminated by YbAl or purely by Al. The surface exhibits a reconstruction, the distances between the reconstruction lines suggest that the surface is terminated by YbAl, with every second ytterbium atom missing. In addition to the flat surface, probably monatomic chains of adatoms can be found on top of the reconstruction. The chemical nature of the atoms is not clear, but the reconstruction suggests that they are formed by the Yb-atoms which are ejected from the surface.
Fig. 9.4(e-g) depict model and topography of another place of the surface which exposes a (210)-facet, as can be concluded both from the structure of the surface and the step height. As one can see from the fig. 9.4(g), the terraces show an additional reconstruction.

9.6.2 Spectroscopy

As discussed in the previous section, the topography of the $YbAl_3$-surface is not trivial. It is to be expected that the spectroscopy will differ on the different patches of the surface. Fig. 9.5(a) shows spectra acquired on a (110)-facet of the surface at 77K. The spectra show a strong peak at about -75mV with a width of 52mV. In addition to this peak, the spin-orbit satellites can be found at around 1.2V above and below the Fermi energy in agreement with photoemission spectra [101] and theory [100]. Finally, a weak structure around -0.6V is found. The peak near the Fermi energy is shown in a high resolution spectrum in fig. 9.5(b) together with a spectrum acquired on a small (110)-facet at 6K. The low temperature spectrum reveals an additional feature at about -3mV with a width of 10mV.

The low temperature spectra acquired on the (210)-facet are shown in fig. 9.6(a) for the different sites on the surface. Besides a similar peak as on the (110) surface which is now at -102 ± 7mV and has a width of 44 ± 10mV, an additional peak shows up close to the Fermi energy at -28 ± 4mV

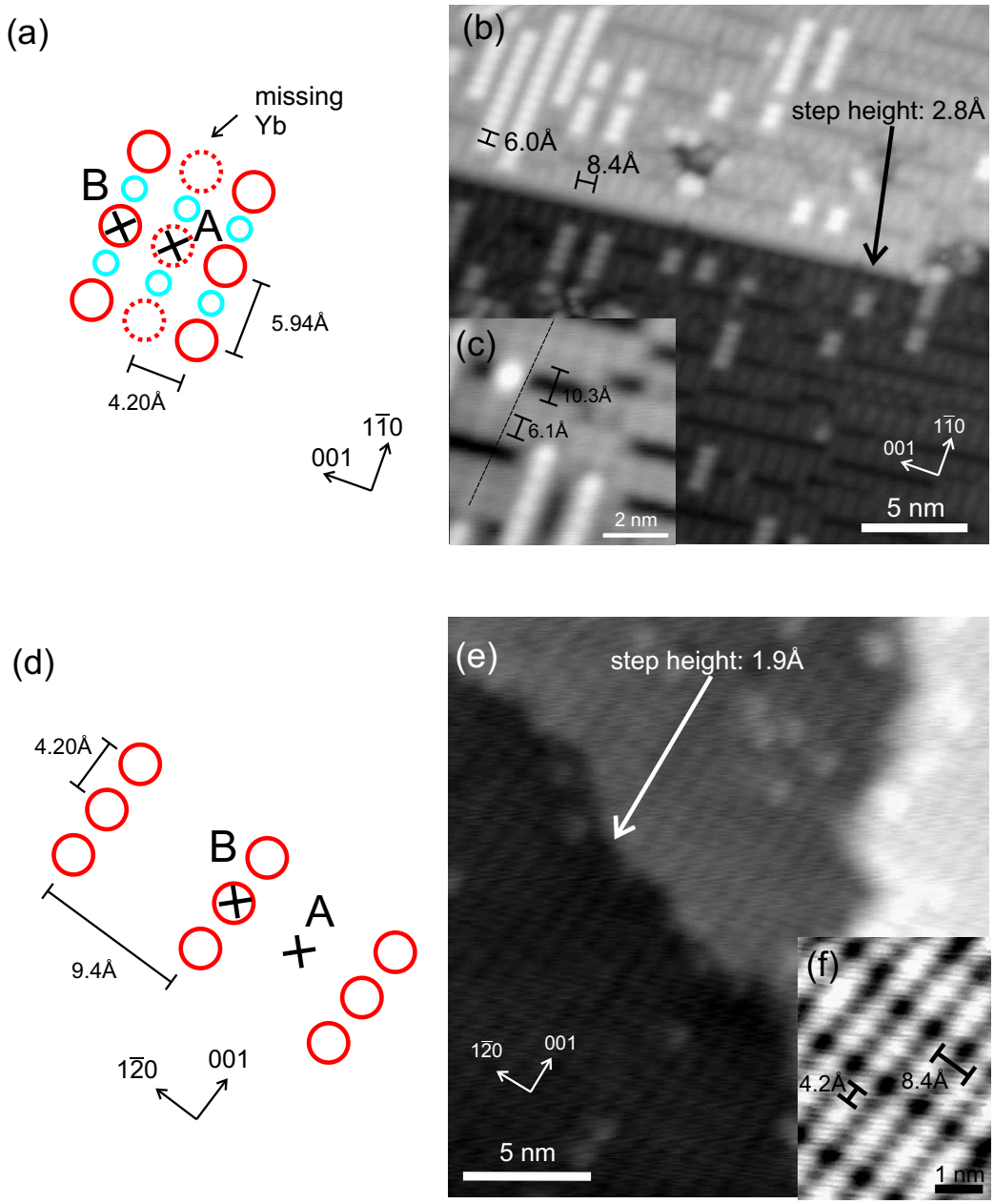

Figure 9.4: (a) Model of the YbAl-terminated (110)-surface of $YbAl_3$, (b+c) STM images of the $YbAl_3$(110)-surface measured at 77K. (d) (210)-surface (only one termination shown), (e+f) corresponding STM images ((e) recorded at 77K, (f) at 6K). In the models, the positions where spectra have been taken are marked by A and B corresponding to the positions in a dark rim and on a bright row in the images.

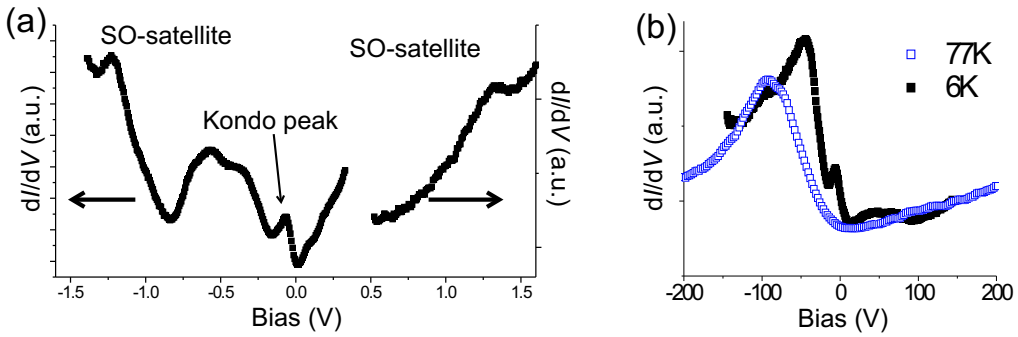

Figure 9.5: (a) Spectroscopy at 77K on the (110) facet. The spin-orbit satellites can be found at ±1.2V. (b) The strong peak at the Fermi energy in a high resolution spectrum acquired at 77K and at 6K. At 6K a second features emerges near the Fermi level.

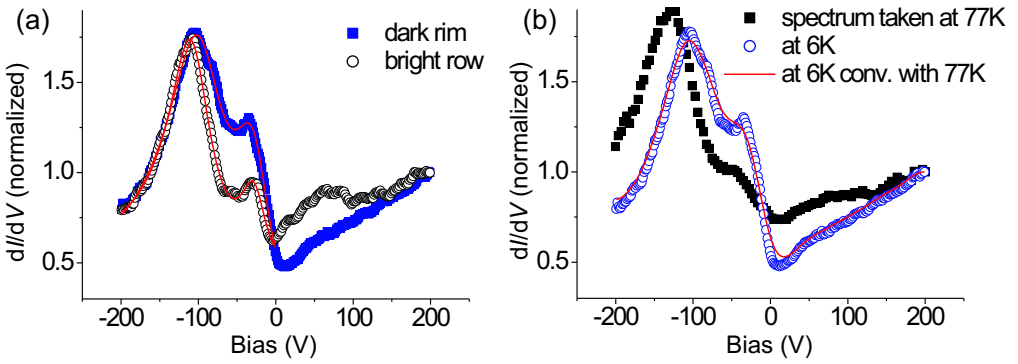

Figure 9.6: Spectra acquired on the (210) facet: (a) Spectroscopy at 6K on different spots of the surface together with the fits of two fano peaks shown as solid lines. (b) Comparison between the spectrum taken at 6K and at 77K in a dark rim. The solid line shows a the 6K-spectrum broadened numerically for comparison.

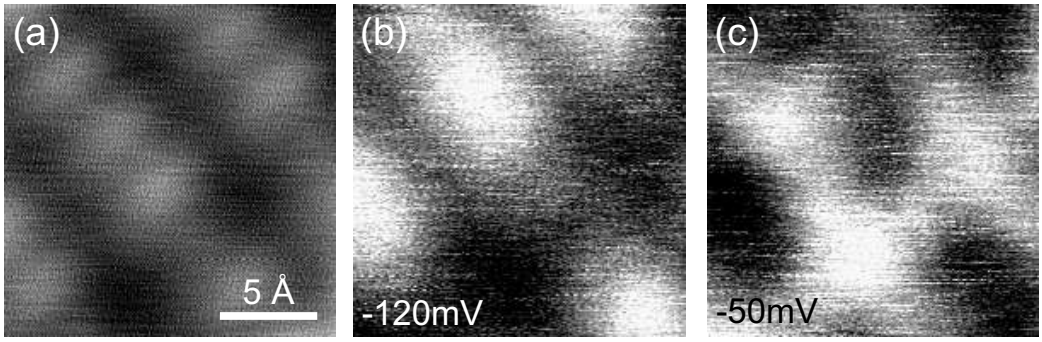

Figure 9.7: (a) Topography of a small part of a (210) facet of $YbAl_3$ showing a corrugation, (b) simultaneously acquired dI/dV-map at -120mV and (c) dI/dV-map acquired on the same spot of the surface at -50mV.

which is only 25 ± 8mV wide. Both features persist at 77K as can be seen from fig. 9.6(b). Fig. 9.6(b) shows in addition to the spectrum recorded on an equivalent spot on the surface at 77K a spectrum acquired at 6K but broadened to simulate a measurement at 77K. It demonstrates that the peak at -25mV can only be resolved as a shoulder at 77K due to the thermal broadening. A spatial mapping of the two peaks found close to the Fermi energy reveals that they originate predominantly from different sites of the surface. Fig. 9.7(a) shows the topography of the reconstruction together with maps at -120mV and at -50mV in fig. 9.7(b+c), roughly at the positions of the two features. The peak at -120mV leads to bright regions predominantly near the atomic rows as seen in fig. 9.7(b), while the peak closer to the Fermi energy becomes stronger in between the reconstruction lines.

facet	T	ϵ_1 [mV]	Δ_1 [mV]	ϵ_2 [mV]	Δ_2 [mV]
(110)	77K	–	–	-75 ± 17	52 ± 15
(210)	6K	-28.4 ± 3.8	24.9 ± 8.1	-102 ± 7	44.3 ± 9.7
	77K	-39.1 ± 6.6	29.1 ± 10.5	-114 ± 10	41.3 ± 6.2

Table 9.1: Peak positions ϵ_n and widths Δ_n determined from STS spectra. The index 1 refers to the peak closer to the Fermi energy.

9.7 Discussion

The discussion will focus mainly on the data acquired on the (210)-facet. The data for both facets are summarized in table 9.1. We attribute the peak which we find around −100mV to a Kondo state of the surface layer. This interpretation is consistent with the spatial mapping of the peak, which exhibits a higher intensity on the reconstruction lines. The surface Yb atoms are expected to have a lower valency than bulk Yb atoms [101], i.e. a smaller hole occupation n_f compared to the bulk value, in agreement with a peak which is shifted further below the Fermi energy. The peak has not been resolved in photoemission, however as for the photoemission experiments also polycrystalline samples have been used, the measurements have averaged over different crystallographic facets which may have a quite different behaviour as can be seen already from a comparison of the spectra which we find on the (110) and (210) facets.
The peak which is closer to the Fermi energy is identidied to be the Kondo peak of bulk $YbAl_3$. From the position of the peak, the Kondo temperature is estimated to be 330±44K, which is in excellent agreement with the SQUID data, which yields 363 ± 52K using n_f as determined from photoemission experiments. With rising temperature, the peak shifts to lower energies and broadens slightly. While the shift is in agreement with theory, the peak is expected to get narrower [119]. A possible reason of the observed broadening in the STS spectra acquired at 77K is the thermal smearing of the Fermi edge. Our spectroscopic results are in reasonable agreement with photoemission data [101, 108], where the Kondo peak is found to be around 45meV with a full width of 50meV [108]. However, instrumental broadening in the photoemission experiments was about 45meV [108], and typical errors for the peak position are as high as 15meV [120] rendering an exact determination of the position and width of the Kondo peak from the spectra very difficult. The width of the Kondo peak is not in agreement with theory, which predicts a much narrower peak with a width on the order of 10mV. It can be excluded that the width is increased by instrumental broadening which is at 6K about 1meV. A possible explanation is a crystal field splitting of the Kondo peak. The crystal field splitting lifts the degeneracy of the f-orbital due to the interaction with the neighbors of the Yb atom and leads to a splitting of the Kondo resonance. For cerium-compounds, the crystal-field splitting is as high as 35mV, while for ytterbium it is expected to be lower than 10mV [107]. In addition, the crystal-field splitting is expected to be

enhanced near the surface due to the reduced symmetry. If the splitting is on the same order of magnitude as the width of the Kondo peak, it might not be possible to resolve it but still lead to a broadening of the peak. On the (110)-facet, at 77K only one peak is found, which may be due to a superposition of the surface-related peak to the Kondo resonance.
From the SQUID measurements, an additional low temperature energy scale which corresponds to the maximum in the magnetization at 14K is expected. Due to the limited resolution and the limitation to occupied states, photoemission experiments have not resolved the features related to the onset of coherence up to now. We have identified a peak at about -3mV on the (110)-facet, which could account for this additional low energy scale and indicates the formation of a coherent heavy fermion state in $YbAl_3$. The position would correspond to a temperature for the onset of coherence of 35K, which agrees well with recent magnetotransport measurements [112, 113, 114].

9.8 Conclusion

We have studied the surface of a rare earth compound by STM. The compound, $YbAl_3$ has first been characterized by SQUID magnetometry, which shows a magnetization curve consistent with Kondo lattice behavior and with previous studies. The SQUID curve reveals two temperature scales, one which leads to a peak at 126K, and a second corresponding to a maximum in the magnetization at 14K. The former can be explained based on the Kondo model, consistent with a Kondo temperature of ~ 350K and the position of the Kondo peak as found from the STS measurements. Both are are in good agreement with previous results, however, new questions arise from the higher spectral resolution of STM. The width of the Kondo peak which we find by STS is larger than expected from theory. As a possible explanation we propose crystal field splitting of the Kondo peak. In addition, we find a strong dependence of the spectra on the crystallographic facet and the surface termination which might resolve the controversy in the photoemission community about position and width of the Kondo peak of $YbAl_3$ [101, 106, 108].

Chapter 10

Conclusions and Perspectives

In this work, I have shown how Scanning Tunneling Microscopy and Spectroscopy can be used to sense electron correlation in low-dimensional systems – near single magnetic adatoms, small molecules, small arrangements of magnetic adatoms – and in periodic systems. Exploiting both the high spatial and spectral resolution of the STM, the Kondo effect is studied at an atomic scale allowing to extract information about the energy scale of the couplings involved. It is demonstrated that the exchange coupling between the spin of an adatom and the conduction band electrons can be tuned by varying the substrate or by modifying the chemical environment of the adatom. The substrate plays the role of the gate electrode in a quantum dot experiment: it modifies the occupation of the adatoms d-orbital thereby tuning the Kondo temperature. The modification of magnetic properties of the adatom by the adsorption of ligands corresponds to the variation of the size of a quantum dot, changing the localization of the d-orbital. By combining the spatial and spectral capabilities of the STM, a systematic study of coupled spin systems, for neighbouring spins in a chain and even in a lattice is presented. The determination of these couplings by STS via the Kondo effect povides a powerful tool to study magnetic interactions near surfaces e.g. in magnetic molecules adsorbed on a metal surface. Provided the coupling of the spin center of a magnetic molecule be sufficiently strong, it is possible to localize it via its Kondo resonance and furthermore to study the interaction with neighbouring magnetic molecules by the modification of the Kondo resonance due to magnetic interactions as has been shown for cobalt adatoms. Thus molecular magnetism in two dimensions can be studied at the atomic scale. In this context the interplay between the magnetic anisotropy of the molecules and

the Kondo effect might offer new insights towards a more complete picture of magnetism at the nanoscale.
In the following two sections I discuss the prospects of the studies of the Kondo effect by STM on one hand and of spin detection on the other hand.

10.1 The Kondo problem in Surface Science

Although the theory of the Kondo physics itself is well developed, it is still a challenge to predict the Kondo properties of systems with reduced symmetries such as an adatom on a metal surface. The low symmetry renders an *ab initio* calculation of the Kondo temperature very difficult and computationally expensive. A first step would be a systematic study of adatom systems by DFT to compare the trends established by the model proposed in chapt. 6 with the results from calculations.
On the experimental side, still the "smoking gun" of the single impurity Kondo effect as measured by STS is missing: the splitting of the Kondo peak of a single adatom in a magnetic field. This proof of the resonance being due to magnetic effects comes into reach by the development of STM instrumentation operating at temperatures below 1K at high magnetic fields. Recently A. Heinrich *et al.* [15] have claimed to see such a splitting in the Kondo peak of Mn adatoms adsorbed at a step edge of an oxide film. However the environment of the adatom was not very well defined.
While I have shown how the magnetic coupling of a spin to the substrate can be increased by the attachment of CO molecules, the opposite effect of localizing the spin and thus stabilizing it is yet to be demonstrated. Ligands which tend to remove electrons from the adatom such as NO might be candidates for this kind of experiment, the Kondo temperature of such a complex is expected to decrease with the number of ligands.

10.2 Spin spotting

The Kondo Effect is only one possibility to make STM sensitive to single spins. It is only recently, that the expression "spin spotting" has been introduced by Manoharan commenting on experiments demonstrating single spin detection under ambient conditions with an STM by a method called

Electron-Spin-Resonance STM (ESR-STM) [121]. While I have exploited the coupling of a spin to the conduction band of the substrate to detect the spin via the Kondo effect, ESR-STM exploits the coupling between the tunneling electrons and the impurity spin. When the spin is placed in a magnetic field it precesses with the Larmor frequency leading to high-frequency components in the tunneling current. This technique has been named ESR-STM. It has been first demonstrated on impurities in silicon [122, 123, 124, 125, 126] and later on paramagnetic molecules on graphite [127, 128]. However, still an independent confirmation of these results is lacking. The ESR-STM approach is more general than detection via the Kondo effect since it neither requires a low temperature environment nor UHV. Furthermore, it has been suggested that an ESR-STM might be used to perform quantum computation [129]. The idea is that the hyperfine splitting of the ESR-signal could be used to make STM sensitive to the nuclear magnetic spin. Thus the spatial resolution of the STM would allow to address the single nuclei as qubits. Looking further into the future, with even more sensitive microscopes, it might eventually become possible to sense the coupling between the nuclear magnetic moment and the tunneling current directly. This would certainly be another revolution of scanning probe techniques - enabling chemical contrast at an unprecedented resolution.
At very low temperatures, the spin is no more precessing around the magnetic field but it can be locked into one of the two possible directions provided the magnetic field is strong enough. Spin-flip processes can be excited by the tunneling electrons if their energy is higher than the Zeeman-splitting of the corresponing spin-states. This excitation can be detected by IETS in the same way as for vibrational excitations. Recently, this technique has been demonstrated for single manganese atoms on an oxide layer on NiAl(110) [15]. The oxide layer decouples the atom from the conduction band electrons of the substrate, thus the formation of the non-magnetic Kondo many body state is inhibited. It is yet to be shown, whether the interaction between the tunneling electrons and the spin of the impurity is basically due to the same physics at different temperatures in the case of ESR-STM and the inelastic spin flip spectroscopy or whether they rely on two different mechanisms.

Abbreviations and Symbols

2PPE Two photon photoemission

AC alternating current

DFT Density Function Theory

EDAX Energy dispersive analysis of X-rays

ESR Electron Spin Resonance

IETS Inelastic Electron Tunneling Spectroscopy

LDA Local Density Approximation

LDOS Local Density of States

KKR Korringa-Kohn-Rostoker

RKKY Ruderman-Kittel-Kasuya-Yosida

SQUID Superconducting Quantum Interference Device

STS Scanning Tunneling Spectroscopy

STM Scanning Tunneling Microscopy

UHV Ultrahigh Vacuum

XRD X-ray diffraction

Δ width of hybridized state

$\tilde{\Delta}$ width of the Kondo resonance

e elementary charge

$\epsilon_\mathrm{d}, \epsilon_\mathrm{f}$ energy of d-, f-orbital

$\epsilon_\mathrm{K}, \tilde{\epsilon}_\mathrm{f}$ energy of the Kondo resonance

$\hbar$ natural unit of action ($\hbar = 0.658\mathrm{eV} \cdot \mathrm{fs}$)

k_B Boltzmann constant ($k_\mathrm{B} = 8.617 \cdot 10^{-5} \frac{\mathrm{eV}}{\mathrm{K}}$)

m_e mass of the electron ($\frac{m_\mathrm{e}}{\hbar^2} = 0.1312(\mathrm{eV} \cdot \mathrm{\AA}^2)^{-1}$)

m^* relative effective mass of an electron

μ_B Bohr magneton ($\mu_\mathrm{B} = 5.788 \cdot 10^{-5} \frac{\mathrm{eV}}{\mathrm{K}}$)

$n_\mathrm{d}, n_\mathrm{f}$ occupation of d-, f-orbital

I Current

J exchange coupling

ρ LDOS

T_K Kondo temperature

Φ work function

χ magnetic susceptibility

U on-site Coulomb repulsion

V Voltage

z tip-sample distance

Bibliography

[1] Intel press release. August 2002. http://www.intel.com/pressroom/archive/releases/20020813tech.htm.

[2] G.Binning, H. Rohrer, Ch. Gerber, and E. Weibel. Surface Studies by Scanning Tunneling Microscopy. *Physical Review Letters*, 49(1):57–61, 1982.

[3] V. Madhavan, W. Chen, T. Jamneala, M.F. Crommie, and N.S. Wingreen. Tunneling into a Single Magnetic Atom: Spectroscopic Evidence of the Kondo Resonance. *Science*, 280:567–569, 1998.

[4] K. McElroy, R.W. Simmonds, J.E. Hoffman, D.-H. Lee, J. Orenstein, H. Eisaki, S. Uchida, and J.C. Davis. Relating atomic-scale electronic phenomena to wave-like quasiparticle states in superconducting $Bi_2Sr_2CaCu_2O_{8+\delta}$. *Nature*, 422:592–596, 2003.

[5] W.J. de Haas, J. de Boer, and G.J. van den Berg. The electrical resistance of gold, copper and lead at low temperatures. *Physica*, 1:1115–1124, 1934.

[6] J. Kondo. Effect of Ordinary Scattering on Exchange Scattering from Magnetic Impurity in Metals. *Physical Review*, 169(2):437–440, 1968.

[7] D. Goldhaber-Gordon, Hadas Shtrikman, D. Mahalu, David Abusch-Magder, U. Meirav, and M.A. Kastner. Kondo effect in a single-electron transistor. *Nature*, 391:156–159, 1998.

[8] Sara M. Cronenwett, Tjerk H. Oosterkamp, and Leo P. Kouwenhoven. A Tunable Kondo Effect in Quantum Dots. *Science*, 281:540–544, 1998.

[9] Jiutao Li, Wolf-Dieter Schneider, Richard Berndt, and Bernard Delley. Kondo Scattering Observed at a Single Magnetic Impurity. *Physical Review Letters*, 80(13):2893–2896, 1998.

[10] A. Hirstein. *Low temperature scanning tunneling microscopy and spectroscopy in ultra-high-vacuum and high magnetic fields*. PhD thesis, EPFL, Lausanne, 1998.

[11] J. Frohn, J.F. Wolf, K. Besocke, and M. Teske. Coarse tip distance adjustment and positioner for a scanning tunneling microscope. *Review of Scientific Instruments*, 60(6):1200–1201, 1989.

[12] J. Tersoff and D.R. Hamann. Theory of the scanning tunneling microscope. *Physical Review B*, 31(2):805–813, 1985.

[13] P.K. Hansma, editor. *Tunneling spectroscopy*. Plenum Press, New York, 1982.

[14] W. Ho. Single-molecule chemistry. *Journal of Chemical Physics*, 117(24):11033–11061, 2002.

[15] A.J. Heinrich, J.A. Gupta, C.P. Lutz, and D.M. Eigler. Single-Atom Spin-Flip Spectroscopy. *Science*, 306:466–469, 2004.

[16] G. Hörmandinger. Imaging of the Cu(111) surface state in scanning tunneling microscopy. *Physical Review B*, 49(19):13897–13905, 1994.

[17] J. Klein, A. Léger, M. Belin, D. Défourneau, and M.J.L. Sangster. Inelastic-Electron-Tunneling Spectroscopy of Metal-Insulator-Metal Junctions. *Physical Review B*, 7(6):2336–2348, 1973.

[18] Allan J. Melmed. The art and science and other apsects of making sharp tips. *Journal of Vacuum Science and Technology B*, 9(2):601–608, 1991.

[19] D.A. Shirley. High-Resolution X-Ray Photoemission Spectrum of the Valence Bands of Gold. *Physical Review B*, 5(12):4709–4714, 1972.

[20] S. Tougaard. Background removal in x-ray photoelectron spectroscopy: Relative importance of intrinsic and extrinsic processes. *Physical Review B*, 34(10):6779–6783, 1986.

[21] R.M. Feenstra, J.A. Stroscio, and A.P. Fein. Tunneling spectroscopy of the Si(111)2×1 surface. *Surface Science*, 181:295–306, 1987.

[22] Vladimir A. Ukraintsev. Data evaluation technique for electron-tunneling spectroscopy. *Physical Review B*, 53(16):11176–11185, 1996.

[23] B.C. Stipe, M.A. Rezaei, and W. Ho. Single-Molecule Vibrational Spectroscopy and Microscopy. *Science*, 280:1732–1735, 1998.

[24] L.J. Lauhon and W. Ho. Effects of temperature and other experimental variables on single molecule vibrational spectroscopy with the scanning tunneling microscope. *Review of Scientific Instruments*, 72(1):216–223, 2001.

[25] L.J. Lauhon and W. Ho. Single-molecule vibrational spectroscopy and microscopy: CO on Cu(001) and Cu(110). *Physical Review B*, 60(12):R8525–R8528, 1999.

[26] H. Hövel, B. Grimm, and B. Reihl. Modification of the Shockley-type surface state on Ag(111) by an adsorberd xenon layer. *Surface Science*, 477:43–49, 2001.

[27] Paul J. Dyson, Brian F.G. Johnson, J. Scott McIndoe, and Patrick R.R. Langridge-Smith. Applications of Laser Desorption and Electrospray Ionization mass Spectrometry at the Transition between Clusters and Colloids. *Inorganic Chemistry*, 39:2430–2431, 2000.

[28] H.J. Lee and W. Ho. Single-Bond Formation and Characterization with a Scanning Tunneling Microscope. *Science*, 286:1719–1722, 1999.

[29] F. Falo, I. Cano, and M. Salmerón. CO Chemisorption on two-dimensional cobalt clusters: A surface science approach to cluster chemistry. *Surface Science*, 143:303–313, 1984.

[30] Nikolaus Knorr, M. Alexander Schneider, Lars Diekhöner, Peter Wahl, and Klaus Kern. Kondo Effect of Single Co Adatoms on Cu Surfaces. *Physical Review Letters*, 88(9):096804:1–4, 2002.

[31] T.-C. Shen, C. Wang, G.C. Abeln, J.R. Tucker, J.W. Lyding, Ph. Avouris, and R.E. Walkup. Atomic-Scale Desorption Through Electronic and Vibrational Excitation Mechanisms. *Science*, 268(5217):1590–1592, 1995.

[32] J.W. Gadzuk. Resonance-assisted, hot-electron-induced desorption. *Surface Science*, 342:345–358, 1995.

[33] J.P. Gauyacq, A.G. Borisov, and G. Raşeev. Lifetime of excited electronic states at surfaces: $CO^{-}(2\pi^{*})$ resonance on Cu(111) and Cu(100) surfaces. *Surface Science*, 490:99–115, 2001.

[34] G.P. Salam, M. Persson, and R.E. Palmer. Possibility of coherent multiple excitation in atom transfer with a scanning tunneling microscope. *Physical Review B*, 49(15):10655–10662, 1994.

[35] L. Bartels, G. Meyer, K.-H. Rieder, D. Velic, E. Knoesel, A. Hotzel, M. Wolf, and G. Ertl. Dynamics of Electron-Induced Manipulation of Individual CO Molecules on Cu(111). *Physical Review Letters*, 80(9):2004–2007, 1998.

[36] P.M. Echenique and J.B. Pendry. The existence and detection of Rydberg states at surfaces. *Journal of Physics C: Solid State Physics*, 11:2065–2075, 1978.

[37] U. Höfer, I.L. Shumay, Ch. Reuß U. Thomann, W. Wallauer, and Th. Fauster. Time-Resolved Coherent Photoelectron Spectroscopy of Quantized Electronic States on Metal Surfaces. *Science*, 277:1480–1482, 1997.

[38] W. Berthold, U. Höfer, P. Feulner, E.V. Chulkov, V.M. Silkin, and P.M. Echenique. Momentum-Resolved Lifetimes of Image-Potential States on Cu(100). *Physical Review Letters*, 88(5):056805:1–4, 2002.

[39] Ch. Reuß I.L. Shurnay, U. Thomann, M. Kutschera, M. Weinelt, Th. Fauster, and U. Höfer. Control of the Dephasing of Image-Potential States by CO Adsorption on Cu(100). *Physical Review Letters*, 82(1):153–156, 1999.

[40] Th. Fauster and W. Steinmann. *Photonic Probes of Surfaces*, pages 347–411. North-Holland, Amsterdam, 1995.

[41] E.V. Chulkov, I. Sarría, V.M. Silkin, J.M. Pitarke, and P.M. Echenique. Lifetime of Image-Potential States on Copper Surfaces. *Physical Review Letters*, 80(22):4947–4950, 1998.

[42] G. Binnig, K.H. Frank, H. Fuchs, N. Garcia, B. Reihl, H. Rohrer, F. Salvan, and A.R. Williams. Tunneling Spectroscopy and Inverse Photoemission: Image and Field States. *Physical Review Letters*, 55(9):991–994, 1985.

[43] T. Jung, Y.W. Mo, and F.J. Himpsel. Identification of Metals in Scanning Tunneling Microscopy via Image States. *Physical Review Letters*, 74(9):1641–1644, 1995.

[44] Y.J. Choi, I.C. Jeong, J.-Y. Park, S.-J. Kahng, J. Lee, and Y. Kuk. Surface alloy formation of Fe on Cr(100) studied by scanning tunneling microscopy. *Physical Review B*, 59(16):10918–10922, 1999.

[45] J.T. Li, W.-D. Schneider, and R. Berndt. Low-temperature manipulation of Ag atoms and clusters on a Ag(110) surface. *Applied Physics A*, 66:S675–S678, 1998.

[46] L. Bürgi, O. Jeandupeux, H. Brune, and K. Kern. Probing Hot-Electron Dynamics at Surfaces with a Cold Scanning Tunneling Microscope. *Physical Review Letters*, 82(22):4516–4519, 1999.

[47] J. Kliewer, R. Berndt, E.V. Chulkov, V.M. Silkin, P.M. Echenique, and S. Crampin. Dimensionality Effects in the Lifetime of Surface States. *Science*, 288:1399–1402, 2000.

[48] L. Vitali, P. Wahl, M. A. Schneider, K. Kern, V.M. Silkin, E.V. Chulkov, and P.M. Echenique. Inter- and intraband inelastic scattering of hot surface-state electrons in Ag(111). *Surface Science Letters*, 523:L47–L52, 2003.

[49] E.V. Chulkov, V.M. Silkin, and P.M. Echenique. Image potential states on metal surfaces: binding energies and wave functions. *Surface Science*, 437:330–352, 1999.

[50] L. Limot, T. Maroutian, P. Johansson, and R. Berndt. Surface-State Shift in a Scanning Tunneling Microscope. *Physical Review Letters*, 91(19):196801:1–4, 2003.

[51] J.K. Gimzewski and R. Möller. Transition from the tunneling regime to point contact studied using scanning tunneling microscopy. *Physical Review B*, 36(2):1284–1287, 1987.

[52] M. Weinelt. Time-resolved two-photon photoemission from metal surfaces. *Journal of Physics: Condensed Matter*, 14:R1099–R1141, 2002.

[53] L. Bürgi. *Scanning tunneling microscopy as a local probe of electron density, dynamics, and transport at metal surfaces*. PhD thesis, EPFL, Lausanne, 1999.

[54] I. Adawi. Electron-Density Oscillations in a General Potential. *Physical Review*, 146(2):379–386, 1966.

[55] Kenneth G. Wilson. The renormalization group: Critical phenomena and the Kondo problem. *Reviews of Modern Physics*, 47(4):773–840, 1975.

[56] P.W. Anderson. Localized Magnetic States in Metals. *Physical Review*, 124(1):41–53, 1961.

[57] J.R. Schrieffer and P.A. Wolff. Relation between the Anderson and Kondo Hamiltonians. *Physical Review*, 149(2):491–492, 1966.

[58] A.C. Hewson. *The Kondo Problem to Heavy Fermions*. Cambridge Studies in Magnetism. Cambridge University Press, 1 edition, 1993.

[59] U. Fano. Effects of Configuration Interaction on Intensities and Phase Shifts. *Physical Review*, 124(6):1866–1878, 1961.

[60] J.W. Gadzuk and M. Plihal. Excited states at surfaces: Fano profiles in STM spectroscopy of adsorbates. *Faraday Discussions*, 117:1–13, 2000.

[61] O. Újsághy, J. Kroha, L. Szunyogh, and A. Zawadowski. Theory of the Fano Resonance in the STM Tunneling Density of States due to a Single Kondo Impurity. *Physical Review Letters*, 85(12):2557–2560, 2000.

[62] V. Madhavan, W. Chen, T. Jamneala, M.F. Crommie, and Ned S. Wingreen. Local spectroscopy of a Kondo impurity: Co on Au(111). *Physical Review B*, 64(16):165412:1–11, 2001.

[63] M. Plihal and J.W. Gadzuk. Nonequilibrium theory of scanning tunneling spectroscopy via adsorbate resonances: Nonmagnetic and Kondo impurities. *Physical Review B*, 63:5404–5426, 2001.

[64] J. Merino and O. Gunnarsson. Simple model for scanning tunneling spectroscopy of noble metal surfaces with adsorbed Kondo impurities. *Physical Review B*, 69:115404:1–10, 2004.

[65] J. Merino and O. Gunnarsson. Role of Surface States in Scanning Tunneling Spectroscopy of (111) Metal Surfaces with Kondo Adsorbates. *Physical Review Letters*, 93(15):156601:1–4, 2004.

[66] H.C. Manoharan, C.P. Lutz, and D.M. Eigler. Quantum mirages formed by coherent projection of electronic structure. *Nature*, 403:512–515, 2000.

[67] G. Grüner and A. Zawadowski. Magnetic impurities in non-magnetic metals. *Reports on Progress in Physics*, 37:1497–1583, 1974.

[68] M.A. Schneider, L. Vitali, N. Knorr, and K. Kern. Observing the scattering phase shift of isolated Kondo impurities at surfaces. *Physical Review B*, 65(12):121406:1–4, 2002.

[69] M.A. Schneider, P. Wahl, L. Diekhöner, L. Vitali, G. Wittich, and K. Kern. Kondo effect of Co adatoms on Ag monolayers on noble metal surfaces. cond-mat/0409390, 2004.

[70] N. Knorr. *Electronic interactions at noble metal surfaces studied by scanning tunneling microscopy*. PhD thesis, EPFL, Lausanne, 2002.

[71] V. Zlatić, B. Horvatić, and D. Šokčević. Density of States for Intermediate Valence and Kondo Systems. *Zeitschrift für Physik B: Condensed Matter*, 59:151–157, 1985.

[72] José A. Rodriguez. Metal-metal bonding on surfaces: molecular orbital study of Pd/Ti(001) and Pd/Ru(001). *Surface Science*, 303:366–376, 1994.

[73] A.C. Pavão, T.C.F. Guimarães, S.K. Lie, C.A. Taft, and W.A. Lester Jr. Modeling the adsorption and dissociation of CO on transition metal surfaces. *Journal of Molecular Structure (Theochem)*, 458:99–121, 1999.

[74] M.C. Desjonquères and D. Spanjaard. A simple chemisorption theory and its application to transition adatoms on transition metals. *Journal of Physics C: Solid State Physics*, 15:4007–4021, 1982.

[75] M. Wessendorf, C. Wiemann, M. Bauer, M. Aeschlimann, M.A. Schneider, H. Brune, and K. Kern. Electronic surface structure of n-ML Ag/Cu(111) and Cs/n-ML Ag/Cu(111) as investigated by 2PPE and STS. *Applied Physics A*, 78:183–188, 2004.

[76] María Andrea Barral, Ana María Llois, and Armando A. Aligia. Hybridization of impurity states with Shockley surface band versus bulk states. *Physical Review B*, 70:035416:1–8, 2004.

[77] Erik S. Sørensen and Ian Affleck. Scaling theory of the Kondo screening cloud. *Physical Review B*, 53(14):9153–9167, 1996.

[78] F. Nouvertné, U. May, A. Rampe, M. Gruyters, U. Korte, R. Berndt, and G. Güntherodt. Ordered surface alloying of Co monolayers on Cu(001). *Surface Science*, 436:L653–L660, 1999.

[79] L.H. Dubois, B.R. Zegarski, and H.S. Luftman. Complex CO-potassium interactions on Cu(100): An electron-energy loss, thermal desorption, and work function study. *Journal of Chemical Physics*, 87(2):1367–1375, 1987.

[80] Rossitza Pentcheva and Matthias Scheffler. Initial adsorption of Co on Cu(001): A first-principles investigation. *Physical Review B*, 65(15):155418:1–11, 2002.

[81] N. Quaas, M. Wenderoth, A. Weismann, R.G. Ulbrich, and K. Schönhammer. Kondo resonance of single Co atoms embedded in Cu(111). *Physical Review B*, 69:201103:1–4, 2004.

[82] A.J. Heinrich, C.P. Lutz, J.A. Gupta, and D.M. Eigler. Molecule Cascades. *Science*, 298:1381–1387, 2002.

[83] L.A. Hanlan, H. Huber, E.P. Kündig, B.R. McGarvey, and G.A. Ozin. Chemical Synthesis Using Metal Atoms. Matrix Infrared, Raman, Ultraviolet-Visible, and Electron Spin Resonance Studies of the Binary Carbonyls of Cobalt, $Co(CO)_n$ (where $n = 1 - 4$), and the Distortion Problem in $Co(CO)_4$. *Journal of the American Chemical Society*, 97(24):7054–7068, 1975.

[84] H.J. Lee and W. Ho. Structural determination by single-molecule vibrational spectroscopy and microscopy: Contrast between copper and iron carbonyls. *Physical Review B*, 61(24):R16347–R16350, 2000.

[85] Lan-Feng Yuan, Jinlong Yang, Qunxiang Li, and Qing-Shi Zhu. First-principles investigation for $M(\mathrm{CO})_n/\mathrm{Ag}(110)$ ($M = \mathrm{Fe, Co, Ni, Cu, Zn, and Ag}$; $n = 1, 2$) systems: Geometries, STM images, and vibrational frequencies. *Physical Review B*, 65:035415:1–5, 2001.

[86] George Blyholder. Molecular Orbital View of Chemisorbed Carbon Monoxide. *Journal of Physical Chemistry*, 68(10):2772–2778, 1964.

[87] W. Chen, T. Jamneala, V. Madhavan, and M.F. Crommie. Disappearance of the Kondo resonance for atomically fabricated cobalt dimers. *Physical Review B*, 60(12):R8529–R8532, 1999.

[88] T. Jamneala, V. Madhavan, and M.F. Crommie. Kondo Response of a Single Antiferromagnetic Chromium Trimer. *Physical Review Letters*, 87(25):256804:1–4, 2001.

[89] V. Madhavan, T. Jamneala, K. Nagaoka, W. Chen, Je-Luen Li, Steven G. Louie, and M.F. Crommie. Observation of spectral evolution during the formation of a Ni_2 Kondo molecule. *Physical Review B*, 66:212411:1–4, 2002.

[90] H. Jeong, A.M. Chang, and M.R. Melloch. The Kondo Effect in an Artificial Quantum Dot Molecule. *Science*, 293:2221–2223, 2001.

[91] Joseph A. Stroscio and Robert J. Celotta. Controlling the Dynamics of a Single Atom in Lateral Atom Manipulation. *Science*, 306:242–247, 2004.

[92] N. Knorr, H. Brune, M. Epple, A. Hirstein, M.A. Schneider, and K. Kern. Long-range adsorbate interactions mediated by a two-dimensional electron gas. *Physical Review B*, 65:115420:1–5, 2002.

[93] M. Garst, S. Kehrein, T. Pruschke, A. Rosch, and M. Vojta. Quantum phas transition of Ising-coupled Kondo impurities. *Physical Review B*, 69:214413:1–23, 2004.

[94] C.A. Büsser, E.V. Anda, A.L. Lima, Maria A. Davidovich, and G. Chiappe. Transport in coupled quantum dots: Kondo effect versus antiferromagnetic correlation. *Physical Review B*, 62(15):9907–9910, 2000.

[95] C.A Büsser, Adriana Moreo, and Elbio Dagotto. Conductance dip in the Kondo regime of linear arrays of quantum dots. *Physical Review B*, 70:035402:1–8, 2004.

[96] H. Schweitzer and G. Czycholl. The second order U-perturbation approach to the Anderson lattice model in one, two and three dimensions. *Solid State Communications*, 74(8):735–742, 1990.

[97] B. Lazarovits, L. Szunyogh, and P. Weinberger. Fully relativistic calculation of magnetic properties of Fe, Co, and Ni adclusters on Ag(100). *Physical Review B*, 65:104441:1–7, 2002.

[98] F. Steglich, J. Aarts, C.D. Bredl, W. Lieke, D. Meschede, W. Franz, and H. Schäfer. Superconductivity in the Presence of Strong Pauli Paramagnetism. *Physical Review Letters*, 43(25):1892–1896, 1979.

[99] En-Jin Cho, J.-S. Chung, S.-J. Oh, S. Suga, M. Taniguchi, A. Kakizaki, A. Fujimori, H. Kato, T. Miyahara, T. Suzuki, and T. Kasuya. Surface core-level shifts and electronic structures of Yb compounds studied with use of photoemission spectroscopy. *Physical Review B*, 47(7):3933–3943, 1993.

[100] F. Reinert, D. Ehm, S. Schmidt, G. Nicolay, S. Hüfner, J. Kroha, O. Trovarelli, and C. Geibel. Temperature Dependence of the Kondo Resonance and Its Satellites in $CeCu_2Si_2$. *Physical Review Letters*, 87(10):106401:1–4, 2001.

[101] S.-J. Oh, S. Suga, A. Kakizaki, M. Taniguchi, T. Ishii, J.-S. Kang, J.W. Allen, O. Gunnarsson, N.E. Christensen, A. Fujimori, T. Suzuki, T. Kasuya, T. Miyahara, H. Kato, K. Schönhammer, M.S. Torikachvili, and M.B. Maple. Observation of Kondo resonance in $YbAl_3$. *Physical Review B*, 37(6):2861–2866, 1988.

[102] P. Nozières. Impuretés magnétiques et effet Kondo. *Annales de Physique*, 10:19–35, 1985.

[103] Peter S. Riseborough. Heavy fermion semiconductors. *Advances in Physics*, 49(3):257–320, 2000.

[104] M. Fäth, J. Aarts, A.A. Menovsky, G.J. Nieuwenhuys, and J.A. Mydosh. Tunneling spectroscopy on the correlation effects in FeSi. *Physical Review B*, 58(23):15483–15490, 1998.

[105] E.E. Havinga, K.H.J. Buschow, and H.J. van Daal. The ambivalence of Yb in $YbAl_2$ and $YbAl_3$. *Solid State Communications*, 13:621–627, 1973.

[106] F. Patthey, J.-M. Irmer, W.-D. Schneider, Y. Baer, B. Delley, and F. Hulliger. Characterization of the hybridized $4f$ states in $YbAl_3$ by high-energy spectroscopies. *Physical Review B*, 36(14):7697–7700, 1987.

[107] R.I.R. Blyth, J.J. Joyce, A.J. Arko, P.C. Canfield, A.B. Andrews, Z. Fisk, J.D. Thompson, R.J. Bartlett, P. Riseborough, J. Tang, and J.M. Lawrence. Temperature-invariant valence-band $4f$ photoemission features in the heavy-fermion compound $YbAl_3$. *Physical Review B*, 48(13):9497–9507, 1993.

[108] L.H. Tjeng, S.-J. Oh, E.-J. Cho, H.-J. Lin, C.T. Chen, G.-H. Gweon, J.-H. Park, J.W. Allen, T. Suzuki, M.S. Makivić, and D.L. Cox. Temperature Dependence of the Kondo Resonance in $YbAl_3$. *Physical Review Letters*, 71(9):1419–1422, 1993.

[109] J.J. Joyce, A.B. Andrews, A.J. Arko, R.J. Bartlett, R.I.R. Blythe, C.G. Olson, P.J. Benning, P.C. Canfield, and D.M. Poirier. Photoelectron spectroscopy of strongly correlated Yb compounds. *Physical Review B*, 54(24):17515–17535, 1996.

[110] F. Reinert, R. Claessen, G. Nicolay, D. Ehm, S. Hüfner, W.P. Ellis, G.-H. Gweon, J.W. Allen, B. Kindler, and W. Assmus. Photoemission experiments on $YbInCu_4$: Surface effects and temperature dependence. *Physical Review B*, 58(19):12808–12816, 1998.

[111] D.P. Moore, J.J. Joyce, A.J. Arko, J.L. Sarro, L. Morales, H. Hochst, and Y.D. Chuang. Bulk electronic structure of $YbInCu_4$ from photoemission: A unique test of the single impurity model. *Physical Review B*, 62(24):16492–16499, 2000.

[112] A.L. Cornelius, J.M. Lawrence, T. Ebihara, P.S. Riseborough, C.H. Booth, M.F. Hundley, P.G. Pagliuso, J.L. Sarrao, J.D. Thompson, M.H. Jung, A.H. Lacerda, and G.H. Kwei. Two Energy Scales and Slow Crossover in $YbAl_3$. *Physical Review Letters*, 88(11):117201:1–4, 2002.

[113] T. Ebihara, E.D. Bauer, A.L. Cornelius, J.M. Lawrence, N. Harrison, J.D. Thompson, J.L. Sarrao, M.F. Hundley, and S. Uji. Dependence of the Effective Masses in $YbAl_3$ on Magnetic Field and Disorder. *Physical Review Letters*, 90(16):166404:1–4, 2003.

[114] E.D. Bauer, C.H. Booth, J.M. Lawrence, M.F. Hundley, J.L. Sarrao, J.D. Thompson, P.S. Riseborough, and T. Ebihara. Anderson lattice behvaior in $Yb_{1-x}Lu_xAl_3$. *Physical Review B*, 69:125102:1–8, 2004.

[115] Thaddeus B. Massalski, editor. *Binary Alloy Phase Diagrams*, volume 1. American Society for Metals, Ohio, 1986.

[116] A. Hiess, J.X. Boucherle, F. Givord, and P.C. Canfield. Magnetic susceptibility and magnetization measurements of an $YbAl_3$ single crystal for groundstate investigations. *Journal of Alloys and Compounds*, 224:33–35, 1995.

[117] A. Hiess, J.X. Boucherle, F. Givord, J. Schweizer, E. Lelièvre-Berna, F. Tasset, B. Gillon, and P.C. Canfield. Magnetism in intermediate-valence $YbAl_3$: a polarized neutron diffraction study. *Journal of Physics: Condensed Matter*, 12:829–840, 2000.

[118] V.T. Rajan. Magnetic Susceptibility and Specific Heat of the Coqblin-Schrieffer Model. *Physical Review Letters*, 51(4):308–311, 1983.

[119] D.M. Newns and N. Read. Mean-field theory of intermediate valence/heavy fermion systems. *Advances in Physics*, 36(6):799–849, 1987.

[120] En-Jin Cho, S.-J. Oh, C.G. Olson, J.-S. Kang, R.O. Anderson, L.Z. Liu, J.H. Park, and J.W. Allen. High resolution photoemission study of $YbAl_3$ at low temperature. *Physica B*, 186-188:70–73, 1993.

[121] Hari C. Manoharan. Spin spotting. *Nature*, 416:24–25, 2002.

[122] Y. Manassen, R.J. Hamers, J.E. Demuth, and A.J. Castellano Jr. Direct Observation of the Precession of Individual Paramagnetic Spins on Oxidized Silicon Surfaces. *Physical Review Letters*, 62(21):2531–2534, 1989.

[123] Y. Manassen, E. Ter-Ovanesyan, D. Shachal, and S. Richter. Electron spin resonance-scanning tunneling microscopy experiments on thermally oxidized Si(111). *Physical Review B*, 48(7):4887–4890, 1993.

[124] Y. Manassen. Scanning Probe Microscopy and Magnetic Resonance. *Advanced Materials*, 6(5):401–404, 1994.

[125] Y. Manassen. Real-Time Response and Phase-Sensitive Detection to Demonstrate the Validity of ESR-STM Results. *Journal of Magnetic Resonance*, 126:133–137, 1997.

[126] Y. Manassen, I. Mukhopadhyay, and N. Ramesh Rao. Electron-spin-resonance STM on iron atoms in silicon. *Physical Review B*, 61(23):16223–16228, 2000.

[127] C. Durkan and M.E. Welland. Electronic spin detection in molecules using scanning-tunneling-microscopy-assisted electron-spin resonance. *Applied Physics Letters*, 80(3):458–460, 2002.

[128] C. Durkan. Detection of single electronic spins by scanning tunnelling microscopy. *Contemporary Physics*, 45(1):1–10, 2004.

[129] G.P. Berman, G.W. Brown, M.E. Hawley, and V.I. Tsifrinovich. Solid-State Quantum Computer Based on Scanning Tunneling Microscopy. *Physical Review Letters*, 87(9):097902:1–3, 2001.

Publications

- P. Wahl *et al*, *Spectroscopic Evidence of Heavy Fermion Behaviour in* $YbAl_3$, in preparation.
- P. Wahl *et al*, *Background Subtraction in Scanning Tunneling Spectroscopy of single Atoms and Molecules*, submitted.
- P. Wahl *et al*, *Single Molecule Spin Tuning and Mapping*, submitted.
- P.Wahl, L. Diekhöner, M.A. Schneider, L. Vitali, G. Wittich, and K. Kern, *Kondo temperature of Magnetic Impurities at Surfaces*, Phys. Rev. Lett. **93**, 176603 (2004).
- M.A. Schneider, L. Vitali, P. Wahl, N. Knorr, L. Diekhöner, G. Wittich, M. Vogelgesang and K. Kern, *Kondo state of Co impurities at noble metal surfaces*, Appl. Phys. A accepted (2004).
- M. Roth, M. Weinelt, Th. Fauster, P. Wahl, M.A. Schneider, L. Diekhöner, and K. Kern, *Scattering of image potential state electrons by steps on Cu(001)*, Appl. Phys. A **78**, 155 (2004).
- L. Diekhöner, M.A. Schneider, P. Wahl, A.N. Baranov, V.S. Stepanyuk, P. Bruno, and K. Kern, *Spin polarized surface states of cobalt nanoislands on Cu(111)*, AIP Conf. Proc. **696**, 53 (2003).
- P. Wahl, M.A. Schneider, L. Diekhöner, R. Vogelgesang and K. Kern, *Quantum Coherence of Image-Potential States*, Phys. Rev. Lett. **91**, 106802 (2003).
- L. Vitali, P. Wahl, M. A. Schneider, K. Kern, V.M. Silkin, E.V. Chulkov and P.M. Echenique, *Inter- and intraband inelastic scattering of hot surface-state electrons in Ag(111)*, Surf. Sci. Lett. **523**, L47 (2003).

- N. Knorr, M. A. Schneider, L. Diekhöner, P. Wahl and K. Kern, *Kondo Effect of Single Co Adatoms on Cu Surfaces*, Phys. Rev. Lett. **88**, 096804 (2002).

Danksagung

Zum Schluß möchte ich all jenen danken, die zum Gelingen dieser Arbeit beigetragen haben bzw. sie erst ermöglicht haben:

- Prof. Dr. Klaus Kern für die Unterstützung und Förderung in den letzten drei Jahren
- Prof. Dr. G. Schatz und Prof. Dr. P. Nielaba von der Universität Konstanz für ihre prompte Bereitschaft als Gutachter und Prüfer für meine Arbeit zu fungieren
- Alexander Schneider für die Betreuung der Doktorarbeit
- mit Lars Diekhöner habe ich viele Aspekte dieser Arbeit und Experimente ausführlich diskutiert, außerdem haben er, Gero Wittich und Dominik Hoffmann dazu beigetragen, daß die dreieinhalb Jahre wie im Flug vergangen sind. Lucia Vitali danke ich für viele anregende Diskussionen.
- O. Gunnarsson und J. Merino für viele Diskussionen über Kondophysik, A.P. Seitsonen für die DFT-Rechnungen, die er zu den Carbonylen durchgeführt hat.
- C. Busch, H. Bender und C.T. Lin aus der Kristallgruppe haben den $YbAl_3$-Kristall gewachsen, die Präparation der Oberfläche hat H. Wendelt von der Kristallpräparation übernommen, SEM und EDAX Messungen an der Oberfläche sowie an STM-Spitzen hat V. Duppel durchgeführt, F. Treubel und Prof. Dr. G. Schatz von der Universität Konstanz haben die SQUID-Messungen gemacht.
- Die Teile für das neue STM – vor allem die Spulenkörper – hat Hermann Beer von der Zentralen Werkstatt gefertigt.

Schließlich möchte ich meiner Frau Sandra für ihr Verständnis und ihren Rückhalt danken und meinen Eltern, die mich immer unterstützt haben.